**REMOVING PARALLAX-INDUCED FALSE
CHANGES IN CHANGE DETECTION**

DISSERTATION

Karmon M. Vongsy, Civilian, USAF

AFIT-ENG-DS-14-M-01

**DEPARTMENT OF THE AIR FORCE
AIR UNIVERSITY**

AIR FORCE INSTITUTE OF TECHNOLOGY

Wright-Patterson Air Force Base, Ohio

AFIT-ENG-DS-14-M-01

REMOVING PARALLAX-INDUCED FALSE CHANGES IN CHANGE
DETECTION

DISSERTATION

Presented to the Faculty

Graduate School of Engineering and Management

Air Force Institute of Technology

Air University

Air Education and Training Command

in Partial Fulfillment of the Requirements for the

Degree of Doctor of Philosophy

Karmon M. Vongsy, BS, MS

Civilian, USAF

March 2014

AFIT-ENG-DS-14-M-01

REMOVING PARALLAX-INDUCED FALSE CHANGES IN CHANGE

DETECTION

Karmon M. Vongsy, BS, MS
Civilian, USAF

Approved:

//signed//   21 February 2014
———————————————————   ———————————————
Lt Col Michael J. Mendenhall, PhD   Date
(Co-Chair)

//signed//   21 February 2014
———————————————————   ———————————————
Dr. Gilbert L. Peterson (Co-Chair)   Date

//signed//   21 February 2014
———————————————————   ———————————————
Dr. Julie A. Jackson (Member)   Date

//signed//   21 February 2014
———————————————————   ———————————————
Dr. Michael T. Eismann (Member)   Date

//signed//   21 February 2014
———————————————————   ———————————————
Dr. Vincent J. Velten (Member)   Date

Accepted:

//signed//   3 March 2014
———————————————————   ———————————————
Adedeji B. Badiru, PhD   Date
Dean, Graduate School of Engineering
and Management

Abstract

Accurate change detection (CD) results in urban environments is of interest to a diverse set of applications including military surveillance, environmental monitoring, and urban development. Although CD approaches with hyperspectral imagery exist, there is no comprehensive framework that describes existing approaches and provides a foundation to generate new ones. This work presents a hyperspectral CD (HSCD) framework. The framework uncovers the need for HSCD methods that resolve false change caused by image parallax. Image parallax is the apparent motion of stationary objects due to differing viewing geometries.

A Generalized Likelihood Ratio Test (GLRT) statistic for HSCD is developed that accommodates unknown mis-registration between imagery described by a prior probability density function for spatial mis-registration. Using a normal prior distribution for the mis-registration leads to a fourth order polynomial test statistic that can be numerically minimized over the unknown mis-registration parameters. A more computationally efficient closed-form solution is developed based on a quadratic approximation derived through a second order Taylor series expansion and provides comparable results to the numerical minimization for the investigated test cases while running 30 times faster. The results indicate an order of magnitude reduction in false alarms at the same detection rate for synthetically mis-registered test data, especially in image regions containing edges and fine spatial features. Investigation of the model parameters is also assessed, and the potential of the derived method to incorporate more complex signal proccessing functions is demonstrated by the incorporation of a parallax error mitigation component. The GLRT statistic is extended to account for parallax errors and the visual results demonstrate the reduction of false alarms; also evident in test statistic histograms and signal-to-clutter ratio (SCR) computations.

Acknowledgements

Table of Contents

List of Figures

List of Tables

List of Abbreviations

Abbreviation   Page

List of Symbols

Symbol

Page

REMOVING PARALLAX-INDUCED FALSE CHANGES IN CHANGE
DETECTION

I. Introduction

1.1   Overview

Change detection (CD) is the problem of discriminating significant changes from
insignificant changes between two images [6]. Traditional image-based CD methods
use red-green-blue color imagery. Due to the spectral limitations with these imaging
technologies, the remote sensing community often exploits hyperspectral (HS) im-
agery for the CD task. A literature review uncovers relatively few works that develop
novel CD approaches for use on HS imagery. Certainly there exist benefits of per-
forming HSCD over regular image-based CD, such as detecting imperceptible targets
in a complex background. However, challenges both in integrating the spectra into
the change detector and working with imagery derived by non-stationary platforms
makes HSCD particularly difficult.

Accurate CD in urban environments is of interest to a diverse range of communities
and a diverse range of applications to include: military surveillance, environmental
monitoring, and urban development. Manually processing of data for CD is daunting;
especially in the case of HS data, due to its hundreds of spectral channels. Therefore,
there is a strong need for methodologies that enable automated detection of *changed*
or *interesting* events in aerial imagery to alert an image analyst or operator. Such a
methodology could provide further support by identifying relevant regions of change.
The incentive for performing HSCD is to take advantage of all the possible change

information available in the data providing a unique method for identifying subtle changes in a complex environment.

1.2 Research question

A basic CD algorithm generates a change mask that identifies change between pixels from a set of images acquired at different times. The reliability of the change mask is influenced by factors such as camera motion, sensor noise, illumination variation, non-uniform attenuation, or atmospheric absorption. Radke *et al.* [6] illustrate that detecting changes and determining their significance is complex and challenging. Two common problems with the application of CD algorithms for airborne data are image registration and parallax error [7] between the reference and test scenes caused by different viewing geometries between the images. Registration errors between the image pair causes pixel mis-alignment (mis-registration) and impacts pixel-based CD. Parallax error, the apparent change in relative positions of stationary objects due to different viewing geometries, is prevalent with taller objects in-scene and often causes false change [8]. Image mis-alignment further impacts the ability to determine if image parallax is the cause of false detections while image parallax makes the alignment of previously present objects impossible, also resulting in false detections.

The significant impact of image mis-registration and image parallax on HSCD leads to the following research question: *Can one develop a HSCD method that simultaneously removes false changes caused by image mis-registration and parallax?*

1.3 Methodology preface

The theory and phenomenology of hyperspectral processes that support change detection is introduced. Specifically, derivations of common change detectors for hyperspectral data, chronochrome (CC) and covariance equalization (CE) are provided

as current state-of-the-art. A new method to account for image mis-registration and parallax-induced false detections in HSCD is presented. The general form of the bilinear interpolation equation is used to account for estimates of image mis-registration for the sub-pixel case, where a generalized likelihood ratio test (GLRT) is constructed to provide a change test statistic for change at each pixel in the temporal hyperspectral image pair. This approach is then modified to incorporate an estimate of the parallax direction in order to mitigate false alarms due to parallax affects between the same two hyperspectral image pairs.

1.4   Results preface

After outlining the practical implementation and data sets used, applications using hyperspectral data are used to detail the GLRT-based algorithms presented and are compared with current anomalous change detectors. The results of the implementations are discussed and performance of the GLRT-based algorithms is evaluated using receiver operating characteristic (ROC) curves when applicable. Comparisons among curves are evaluated in terms of area under the ROC curve (AUC) estimated on the basis of available ground truth. The AUC for the mis-registration GLRT-based algorithm ($\text{AUC}_{\text{GLRT}_{\text{CC}}} = 0.9981$ and $\text{AUC}_{\text{GLRT}_{\text{CE}}} = 0.9954$) is higher than the current state-of-the-art baseline algorithms ($\text{AUC}_{\text{CC}} = 0.9972$ and $\text{AUC}_{\text{CE}} = 0.9909$) which demonstrate the effectiveness of the methods established in this research. In relation to a similar mis-registration approach, Local Co-Registration Adjustment (LCRA), the GLRT-based algorithm provides comparable performance. Visually, test statistics reveal that parallax mitigation reduces false alarms.

1.5 Organization of dissertation

Chapter II presents the common processes used in CD and computer vision pertinent to this research. A process framework for HSCD is introduced in order to frame the theoretical developments of this work. The new theoretical foundation for addressing false detections due to image mis-registration is described. Furthermore, Chapter III builds on this foundation to mitigate false detections due to image parallax. Chapter IV provides detailed simulation results demonstrating the effectiveness of the mitigation approaches. Finally, Chapter V summarizes the research presented before highlighting the contributions and efforts for potential future research.

II. Background

2.1 Introduction

Detection and characterization of geospatially coincident and temporally variant imagery has been of interest to researchers for many years due in large part to the number of applications across diverse disciplines. Automated image change detection (CD) is the process of autonomously analyzing spatially coincident image pairs, and identifying regions that have undergone significant spatial or spectral variation. CD is an important process in monitoring and managing military applications because it provides quantitative analysis of the spatial distribution of the population of interest.

Macleod and Congation [9] list four aspects of CD which are important when performing a monitoring task: (1) detecting the changes that have occurred; (2) identifying the nature of the change; (3) measuring the spatial area extent of the change; and (4) assessing the spatial pattern of the change. CD results are further processed by some means of characterization to filter the number of detections to a more meaningful subset based upon some application specific requirement or *a priori* information.

The basis of using remote sensing data for CD is that scene changes result in radiance value differences that can be sensed remotely. Imaging spectroscopy, the process of simultaneously acquiring data at multiple distinct spectral wavelengths, is a passive remote sensing technology that is of specific interest to the study of advancing CD capabilities. Spectral sensor-related constraints that affect the quality of the imagery and bound the options for processing image data include: bandwidth, sampling interval (the spacing between two consecutive wavelengths), and data type (*i.e.*, the number of bits used to digitally represent the magnitude of the sensor response). These, and other constraints, are typically referred to as sensor *operating*

conditions (OCs) [5, 10]. Two commonly referenced classes of spectral imaging spectrometers are hyperspectral (HS) and multispectral (MS). The distinction between these two classes of imagers are typically discriminated by the number of spectral bands captured as well as the channel bandwidth; an acceptable benchmark for HS sensors is the collection of hundreds of contiguous spectral bands while MS sensors collect less than 20 generally non-contiguous spectral bands (Fig. 1). An additional discriminator for an HS versus MS imaging system is the full width at half maximum (FWHM). FWHM refers to the detector response derived from exposure to a source and is assumed to be Gaussian. The FWHM contributes to the spectral channel bandwidth, typically reported in microns or nanometers (Fig. 2) [11].

HS-based CD has many advantages over MS-based CD in detecting and discriminating surface materials because the former provides a continuous spectrum across a wide range of wavelengths where the later does not. Typical gray-scale imagery (an image in which the value of each pixel is a single intensity) has a limited capability for detecting spectral change, but generally provides greater spatial resolution. These gray-scale images often fail to provide sufficient information to discriminate low contrast targets that might be employing concealment techniques. Hyperspectral change detection (HSCD) provides the added sensitivity to reveal camouflage, and in general, camouflage, concealment, and deception (CC&D) targets. Here, HSCD is addressed by means of a process framework developed from a thorough study of the CD literature. This CD framework focuses on passive remote sensors, in particular imaging spectrometers that only measure radiation emitted or reflected into the sensor by the object under scrutiny and/or its surroundings.
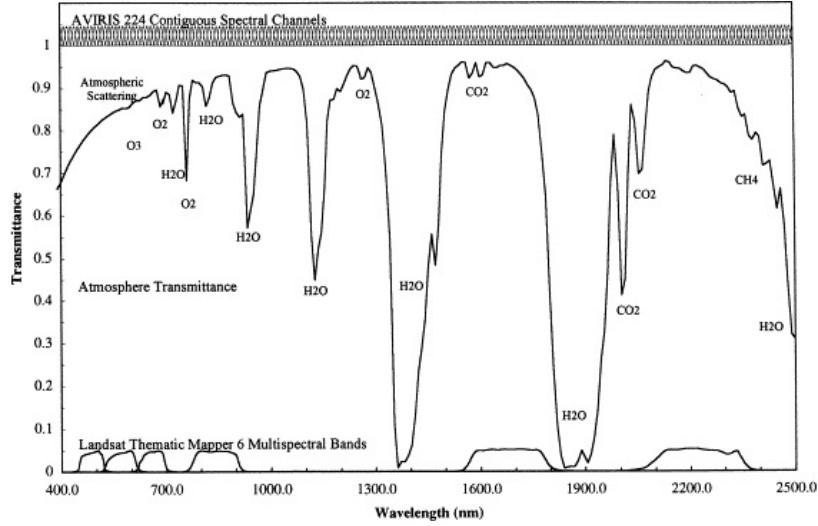
Figure 1. A comparison of the NASA's Airborne Visible/Infrared Imaging Spectrometer (AVIRIS) 224 spectral channel sensor for a measured spectra from 400 to 2500 nm at 10 nm intervals across the solar reflected spectrum and 6 of the multispectral bands measured by the LANDSAT Thematic Mapper [1].
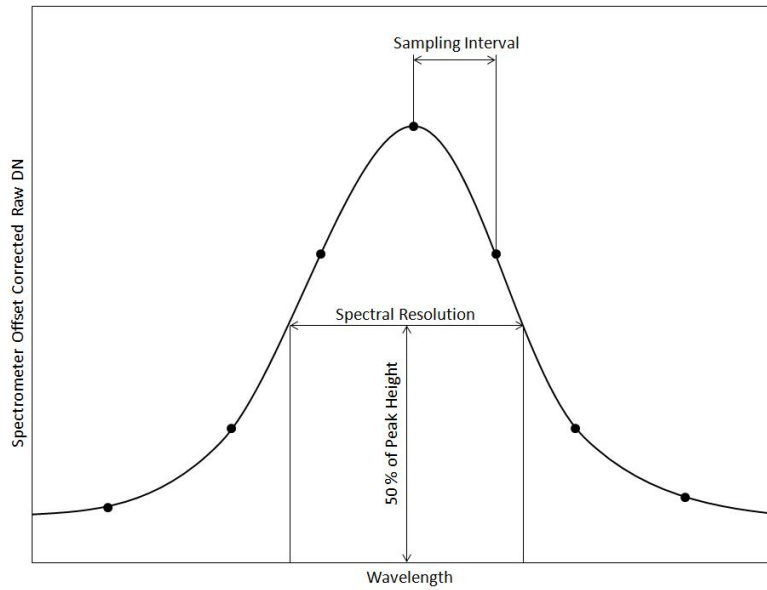
Figure 2. Illustration of full width at half maximum (FWHM) used to indicate spectral resolution.

2.2 Hyperspectral change detection literature review

There are several methods for addressing HSCD in an end-to-end system; these methods are organized into groups for examination: pre-processing, change detectors,

7

thresholding, post-processing, and analysis/assessment. The major topics are examined to provide relevant background for the proposed framework. Although there is a multitude of approaches in the literature as to the organization of CD, they converge on the following recommendations: CD should involve data acquired by the same sensor, with the same spatial resolution, same viewing geometry, same spectral bands, same radiometric resolution, and acquired at the same time of day [7]. It is also desirable to perform the change analysis at the same collection time to limit the differences associated with sun angle and seasonal variations.

The simplest CD framework separates significant and non-significant changes that generate a correspondence image from an image pair (Fig. 3). Images are typically referred to as the *reference image*, the *test image*, and the *change response*. In the CD routine, two corresponding pixels belonging to the same location in an image pair are determined on the basis of a quantitative measure. Two temporal image frames (or a pair of temporal images) are the minimum requirement to identify change.
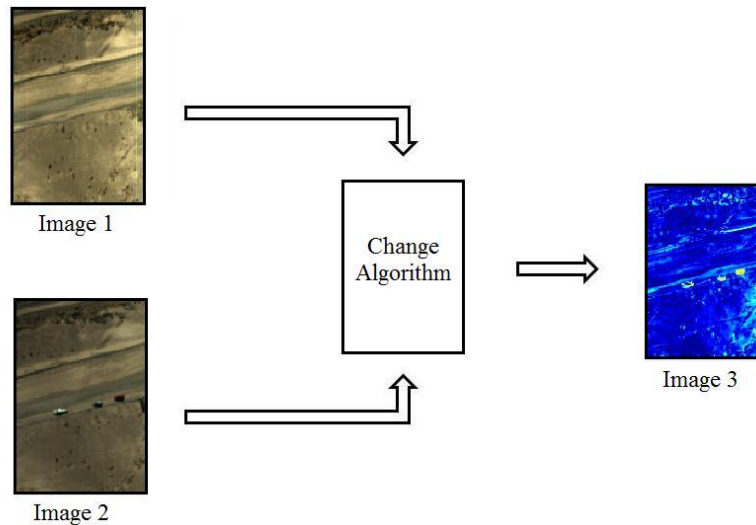
Figure 3. Simple CD framework using a minimal processing schema. Here Image 1 is referred to as the reference Image, Image 2 the test image, and image 3 the change response.

Although CD can be performed in the simplest manner as depicted in Fig. 3,

there is evidence that an extended form would improve HSCD performance. HSCD results depend on many factors, and this section details these factors into a comprehensive framework. Jensen [12] introduces a CD procedure to monitor land CD using remotely sensed data that consists of: (1) state the CD problem, (2) considerations of significance when performing CD, (3) image processing of remote sensor data to extract change information, (4) quality assurance and control program, and (5) distribute results. Lu *et al.* [13] describe three major steps involved when implementing a CD system: (1) image pre-processing, (2) selection of suitable techniques, and (3) accuracy assessment. Similarly, Jianya *et al.* [14] discuss the problem of CD and focus on the same three steps as in [13], but with the terms: (1) pre-processing, (2) CD algorithms, and (3) accuracy assessment. These simplistic descriptions of the CD processing chain lack robustness and do not capture many of the challenges in image-based CD. These frameworks further do not take advantage of HS images.

The literature is in common agreement that a CD algorithm requires additional processes beyond the simple frameworks described previously. However, there is no consensus as to a single universally applicable processing chain. The choice of routines within each method in the framework must be navigated based on the application and the needs of the end-user. Once the areas of the framework are determined, an understanding of specific data processing requirements is easily assessed.

Relatively few works support HSCD and most do not define the entire processing chain. Eismann *et al.* [15, 16] propose the use of an affine transformation to eliminate errors associated by multiple algorithms during the pre-processing stage. An affine transformation is a linear transformation and translation between two domains – for CD this is the reference domain to the test domain. Eismann *et al.* [15, 16] assume the same sensor is utilized, images are acquired under similar environmental conditions, and that image matching or cropping has already occurred. Ortiz-Rivera *et al.* [17]

9

also present general steps for HSCD to include pre-processing for the estimation of the change mask, which indicates the pixels that reflect a change. The steps are application specific to an extent and should be further developed to include all pre-processing possibilities such as feature extraction and dimensionality reduction. Ultimately the environmental setting plays an important role in the ability to identify change; as the setting becomes more complex (*i.e.*, heavy vegetation surrounding a city) the accuracies of CD techniques suffer. The literature often focuses on a single physical environment limiting the impact of their analysis in evaluating different CD methods across a variety of background conditions [9, 18, 19]. Incorporating post-processing into the CD processing chain may enable a more diverse study by level setting results due to various background conditions.

2.3 Organization of CD methods

Table 1 provides a basis for discussing a unified CD processing chain. It lists five foundational methods: pre-processing, change detector, post processing, thresholding, and analysis/assessment and summarizes typical routines within each overarching method with applicable supporting citations.

Table 1. A table of CD methods with supporting routines and literature references.

Change Detection Methods					
Pre-processing	Change detector	Post-processing	Threshold	Post-processing	Analysis assessment
●Geometric registration ●Radiometric correction (or normalization)	●Local-based methods ●Pixel-based methods	●HSV Transformation ●Contextual information	●Empirically ●Theoretical	●False alarm mitigation	●Visual ●Quantitative ●ROC curve ●Confusion matrix
Radke [6], Jensen [12], Eismann [15], Rosenfeld [20]	Lu [13], Marcenaro [21]	Knudsen [22], Zhang [23]	Rosin [24], Sahoo [25], Sezgin [26]	Radke [6], Lee [27]	Radke [6], Rosin [24], Sezgin [26]

The pre-processing stage adds distinct benefits to the CD process. Precise registration of multi-temporal imagery is a critical prerequisite of accurate pixel-level CD. The change detector is the heart of the change detection method and a variety of change detectors are available. A threshold scheme is typically employed to distinguish a separation between significant and insignificant changes. The selection of an appropriate threshold value for discriminating unchanged pixels from the changed pixels is also a key factor in most CD methods [28]. A binary change mask is created by classifying those pixels with a value above the threshold as being a valid change. Unfortunately, there are a number of factors that make obtaining high accuracy change masks a difficult task. Two common examples include changing illumination conditions and image pair mis-alignment. Post-processing those changes can improve the change mask result.

Post-processing, though rarely mentioned in the HSCD literature, is used to refine CD results and can be viewed as a false-alarm mitigation method. Rudimentary approaches post-process the change mask with standard binary image processing

operations [6]. Other approaches build binary classifiers based on training data from the change response to produce a more accurate change result [29]. Table 1 includes post-processing as a capability before or after the thresholding stage.

Lu *et al.* [13] provide factors that influence the accuracy of CD results, including: (1) precise geometric registration between multi-temporal images, (2) calibration or normalization between multi-temporal images, (3) availability of quality ground truth, (4) the complexity of the landscape and environment of the study area, (5) CD methods or algorithms used, (6) classification and CD schemes, (7) analyst's skills and experience, (8) knowledge and familiarity of the study area, and (9) time and cost restrictions. The performance of a CD algorithm, including the necessary pre- and post- processes, can be evaluated visually and quantitatively depending on the goal. Subcomponents of the CD framework can also be evaluated individually [6]. Assessing the accuracy of CD products is an important step in assessing the validity of the method. In assessing changes based on remotely sensed data, the major impediment is that the estimate values are difficult to compute due to the complexity of the processes involved and more often the truth data is not available for computing accuracy. When the inherent limitations are appropriately dealt with, pre-processing is adequately incorporated, and appropriate CD algorithms are selected, the assessment will reveal adequate results.

Analysis of the literature provides ample evidence to support the conclusion that HS data can be effectively used to detect and monitor changes. However there is an agreement with the observation of [30] that one of the challenges confronting the community is to develop an improved understanding of the *CD process* on which to build an understanding of how to match applications and methods. Our CD framework provides an improved understanding based on careful analysis of the literature and moves the community closer to matching applications and methods for improved

CD results.

2.4 Change detection framework

The framework presented in this dissertation document provides a foundation for comparing HSCD systems [2]. The framework provides categories of methods that must be acknowledged when analyzing HSCD and is presented in Fig. 4. It begins with two temporal HS image cubes, a reference image and a test image. The first step is to pre-process both image cubes to suppress undesired distortions and enhance image features important for the rest of the processing change. The pre-processed image cubes are supplied to the CD step which then outputs a CD response map with the raw detector results. The CD response map can either be post-processed or proceed to a threshold step in order to identify significant changes and represent them as a change mask. The change mask can then be enhanced in an additional post-processing step. The final change mask is then used to analyze CD performance.
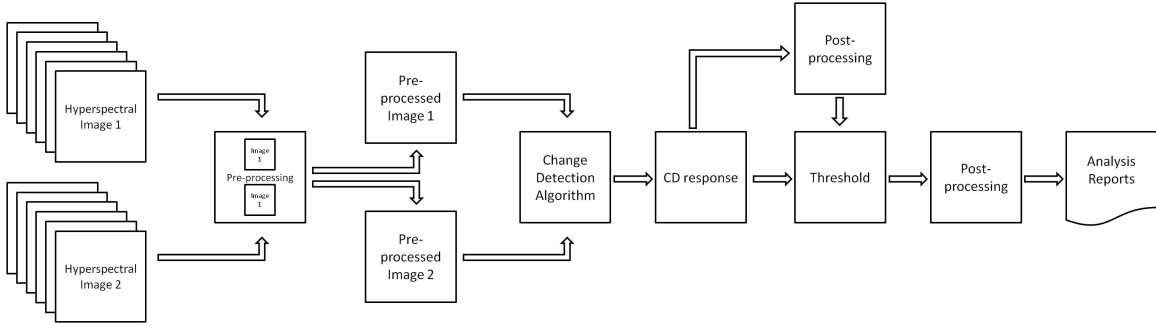
Figure 4. CD framework process [2].

2.4.1 Pre-processing

The form of pre-processing depends on the data under analysis. For example, if the HS image data is "raw" (obtained directly from the sensor), then atmospheric compensation and band reduction (related to specific atmospheric distortion windows) should be performed. Typical pre-processing steps include: georegistration [31], or-

thorectification [32], atmospheric compensation (*e.g.*, flat field correction, empirical line calibration, QUick Atmospheric Correction (QUAC) and Fast Line-of-sight Atmospheric Analysis of Spectral Hypercubes (FLAASH) [33]). Dimensionality reduction [34–37] and resolution enhancement [38].

Georegistration is the alignment of an unreferenced image with geodetic imagery. In general, this process aligns two images and correlates the images to a physical location by examining a set of distinguishable points. If not performed properly it can have a negative effect on the performance of the CD system. For example, if the accuracy of the georegistration degrades substantially, it may not be possible to correlate spatial pixels in the imagery to known points on the ground. It would then become nearly impossible to obtain an accurate location change result referenced to a ground position.

Orthorectification is the process of registering data pixels to a map grid. The end result is that the often visually-distorted data cubes captured from a HS sensor are spatially re-sampled so that they may be overlaid on a common set of ground coordinates. It then becomes possible to measure distances between objects in the imagery since the location of every pixel is known. The drawback to orthorectification is that the spatial interpolation routines alter the spectral content of the HS vectors within the image cube which may degrade detection performance. Fig. 5 demonstrates a notional orthorectification scenario. The left image displays an object as seen on the ground, known to be a square. The middle image is the raw image with the object as captured by the sensor to include geometric distortion (thus the square is distorted). The right image is representative after orthorectification; the image is transformed so that the sensor captured the object from a perpendicular view.

Figure 5. (left) Square object as it appears on the ground, (middle) square object sampled with a pushbroom sensor (horizontal distortion), (right) resulting orthorectified imagery.

Atmospheric scattering, absorption, and reflections as well as local environmental reflections contaminate the radiance received at the sensor (Fig. 6). The interpretation of surface features is enhanced by correcting for these effects. Atmospheric compensation is a technique used to remove the effects of the gases, aerosols, and water vapor present in the atmosphere on the spectra observed by the HS sensor. This is particularly important for interpreting temporal changes in imagery taken at a different time of day or a different time of year. For a visible to near infrared/short wave infrared (VNIR/SWIR) HS sensor, there are five intervening atmosphere/environment effects to the spectral radiance that are ultimately received by the sensor [39]:

1. Direct solar irradiance reflected off the object and transmitted through the atmosphere to the sensor;

2. Indirect solar irradiance scattered by the atmosphere, reflected off the object, and transmitted through the atmosphere to the sensor;

3. Scattered irradiance from the ground and local objects reflected off the object and transmitted through the atmosphere to the sensor;

4. Ground scattered radiance scattered further by the atmosphere, reflected off the object, and transmitted through the atmosphere to the sensor, also known as adjacency effect; and

5. Upwelling path radiance scattered by the atmosphere directly to the sensor.

The effect of the atmosphere on the solar irradiance spectrum is illustrated in Fig. 7. Note the relative loss in intensity at several wavelengths between 900 nm and 1100 nm due to gas and vapor absorption. Also note that two major absorption features centered around 1400 nm and 1900 nm are predominantly due to atmospheric water vapor.
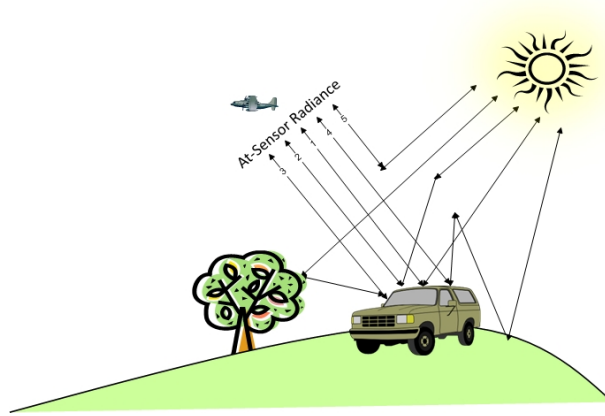
Figure 6. Solar reflective effects described by (1) Direct solar reflectance, (2) Indirect solar reflectance, (3) Local object scattering, (4) Adjacency effect, and (5) Scattered path radiance.
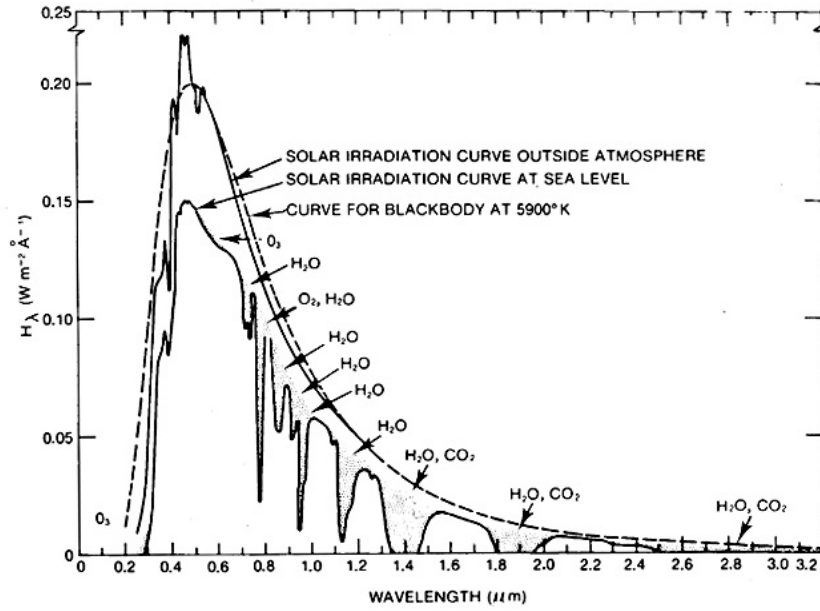
Figure 7. Solar irradiation curves: (dashed) blackbody radiator at 5900K (estimate of the suns solar radiation), (solid attenuated) solar irradiation curve at sea level, (solid non-attenuated) solar irradiation curve at the top of the atmosphere (energy from the sun entering the atmosphere) [3].

Dimensionality reduction plays a role in reducing processing time [34, 37], improving visualization [35, 36], and improving accuracy results in the assessment [37]. It is often desirable to remove some of the bands from the HS data cube that have low Signal-to-Noise Ratio (SNR); the bands corresponding to atmospheric water absorption are commonly among those with low SNRs as the gases and vapor in the atmosphere between the (airborne) sensor and the ground plane tend to absorb light at those wavelengths.

2.4.2 Change detectors

2.4.2.1 Overview

A comprehensive survey of image CD algorithms is presented in [6]. A variety of change detectors have been developed, and many have been summarized and case

17

studied [12, 13, 40–42]. Many of the documented algorithms can be modified for use with HS images, though few actually develop the detector specifically for HSCD. Deer [43] categorizes CD methods based on the notion of pixel-, feature-, and object-level CD. With the advent of HS images a fourth category of change detectors has emerged, namely spectral-based change detectors. A summary of these four categories of CD are listed in Table 2.

Table 2. Change detectors.

Pixel-based	Feature-based	Object-based	Spectral-based
−Image differencing −Image rationing −Image regression −Change vector analysis (CVA) −Endmember analysis	−Principal components analysis (PCA) −Local texture −Shape analysis −Vegetation index differencing (NDVI) −Wavelet	−Artificial intelligence −Artificial neural networks −Direct multidate classification −Fuzzy post-classification comparison −Post-classification comparison	−Spectral angle mapper −Spectral correlation mapper −Model-based chronochrome −Model-based covariance equalization

Pixel-level CD requires additional processes as the computations involve numeric values of each image band (*e.g.*, taking image differences or performing image ratios). These techniques evaluate only the difference between corresponding pixels between the reference and test images. Pixel-level CD requires less computation since only one pixel is considered at a time. However, it is very sensitive to noise and illumination differences since it does not exploit local structure information.

Feature-level CD involves a transformation of the spectral or spatial properties of the image (*e.g.*, principal component analysis, texture analysis, or vegetation analysis).

Object-level CD requires the most advanced processing (*e.g.*, post-classification

processing or neural networks analysis). The use of machine-learning algorithms, artificial neural networks, and decision tree classifiers have gained attention in recent years, has become an alternative to conventional CD approaches [44, 45]. Increased classification accuracy is often cited as the primary reason for developing and applying these techniques; however, these approaches are computationally complex and can require a considerable number of trusted training samples. Advantages of object-level CD routines include: no need for post-CD filtering and smoothing; less impact of slight geometric offsets between image datasets; and the ability to include context relationships to improve CD results [46]. The disadvantages are that the processes are laborious and usually require previous knowledge of the study area as well as accurate definition of the changes to be identified.

Spectral-based detectors make a direct comparison between spectra utilizing the entire spectrum of information to provide areas of change. There exists the potential to implement a spectral matching change detector using techniques typically formulated for spectral detection [47]. Here one exchanges the spectral library for a spectra signature at each corresponding spatial pixel in the test image. However, these methods inherently assume perfect registration since they perform pixel-level CD.

Junior *et al.* [48] explore the spectral angle mapper (SAM) and spectral correlation mapper (SCM) classification methods and use them as spectral change detectors (SCD). SCD, such as the Chronochrome (CC) and Covariance Equalization (CE) [49] algorithms, perform model-based CD through signature prediction.

2.4.2.2 Chronochrome change detector

The chronochrome change detector is a fundamental component of this dissertation and a derivation of that method is provided here. In general, the chronochrome provides the linear least mean squares solution to the prediction error, commonly

known as the optimal Wiener filter solution [50]. The chronochrome requires the cross-covariance between the image pair because it is a pixel-to-pixel computation forcing precise registration which is difficult to achieve. It does, however, use the generalized likelihood ratio test (GLRT), which is well understood in the detection community, and unknown parameters are replaced with their maximum likelihood estimates. Covariance equalization is an alternative to chronochrome by approximating the cross-covariance through whitening in order to eliminate the cross-statistics [51].

Under similar environment conditions and perfect registration where no parallax exists then the CD hypothesis test is

$$H_0 \quad : \quad \mathbf{t} = \mathbf{r},$$

$$H_1 \quad : \quad \mathbf{t} \neq \mathbf{r},$$

where H_0 is the null hypothesis of no change, H_1 is the alternative hypothesis of a change, and $\mathbf{r}$ and $\mathbf{t}$ are two measurements from a reference image and test image. In the formulation, lower-case boldface characters represent vectors, and upper-case boldface characters represent matrices. However, in reality, the respective signatures can be slightly different as a result of intrinsic variability. As a result, the measurement for a given pixel at time-one ($\mathbf{r}$) may be significantly different than that at time-two ($\mathbf{t}$), even when the underlying material associated with the pixel has not changed. Thereby, the measurements are assumed to have a linear transformation, and thus, the hypothesis test is

$$H_0 \quad : \quad \mathbf{t} = \mathbf{A}\mathbf{r} + \mathbf{b} + \mathbf{n},$$

$$H_1 \quad : \quad \mathbf{t} \neq \mathbf{A}\mathbf{r} + \mathbf{b} + \mathbf{n},$$

where $\mathbf{A}$ is the unknown gain matrix, $\mathbf{b}$ is an unknown offset vector, and $\mathbf{n}$ is additive

Gaussian noise. The unknown parameters are assumed space-invariant such that the global sample statistics of $\mathbf{r}$ and $\mathbf{t}$ are sufficient to estimate the transformation parameters.

The estimated gain matrix $\hat{\mathbf{A}}$ and offset vector $\hat{\mathbf{b}}$ are determined from a minimum mean-squared error perspective following the standard Wiener filter derivation requiring the error to be orthogonal to the reference spectra $\mathbf{r}$, or

$$E\left\{[\mathbf{t} - (\mathbf{Ar} + \mathbf{b})]\mathbf{r}^{\mathbf{T}}\right\} = \mathbf{0}. \tag{1}$$

Additionally, the residual error is required to be zero mean,

$$E\left\{[\mathbf{t} - (\mathbf{Ar} + \mathbf{b})]\right\} = \mathbf{0}. \tag{2}$$

The estimate for $\mathbf{b}$ is first found in terms of $\mathbf{A}$ as

$$E\left\{[\mathbf{t} - (\mathbf{Ar} + \mathbf{b})]\right\} = \mathbf{0}$$

$$E[\mathbf{t}] - \mathbf{A}E[\mathbf{t}] - \mathbf{b} = \mathbf{0}$$

$$\hat{\mathbf{b}} = E[\mathbf{t}] - \mathbf{A}E[\mathbf{r}]$$

$$\hat{\mathbf{b}} = \hat{\mathbf{m}}_{\mathbf{t}} - \mathbf{A}\hat{\mathbf{m}}_{\mathbf{r}} \tag{3}$$

where $\hat{\mathbf{m}}_{\mathbf{r}}$ and $\hat{\mathbf{m}}_{\mathbf{t}}$ are the sample mean vectors from time-one and time-two. The

estimate of $\mathbf{A}$ is

$$
\begin{aligned}
E\left\{\mathbf{tr^T} - \mathbf{Arr^T} - \mathbf{br^T}\right\} &= 0 \\
FE[\mathbf{tr^T}] - \mathbf{A}E[\mathbf{rr^T}] - \mathbf{b}E[\mathbf{r^T}] &= 0 \\
E[\mathbf{tr^T}] - \mathbf{A}E[\mathbf{rr^T}] - (\hat{\mathbf{m}}_t - \mathbf{A}\hat{\mathbf{m}}_r)E[\mathbf{r^T}] &= 0 \\
E[\mathbf{tr^T}] - \mathbf{A}E[\mathbf{rr^T}] - \hat{\mathbf{m}}_t E[\mathbf{r^T}] + \mathbf{A}\hat{\mathbf{m}}_r E[\mathbf{r^T}] &= 0 \\
E[\mathbf{tr^T}] - \hat{\mathbf{m}}_t E[\mathbf{r^T}] &= \mathbf{A}E[\mathbf{rr^T}] - \mathbf{A}\hat{\mathbf{m}}_r E[\mathbf{r^T}] \\
E[\mathbf{tr^T}] - \hat{\mathbf{m}}_t E[\mathbf{r^T}] &= \mathbf{A}(E[\mathbf{rr^T}] - \hat{\mathbf{m}}_r E[\mathbf{r^T}]) \\
\hat{\mathbf{A}} &= \frac{E[\mathbf{tr^T}] - \hat{\mathbf{m}}_t \hat{\mathbf{m}}_r^T}{E[\mathbf{rr^T}] - \hat{\mathbf{m}}_r \hat{\mathbf{m}}_r^T} = \frac{\mathbf{C_{tr}}}{\mathbf{C_r}}
\end{aligned}
\tag{4}
$$

where $\mathbf{C_r}$ is the sample covariance matrix of the time-one data and $\mathbf{C_{tr}}$ is the sample cross-covariance of the time-one and time-two data.

After applying the transformation to the test image using the estimates derived, an error matrix is formed via differencing the reference and prediction images [51].

In order to address registration concerns and create an algorithm that is more robust to registration errors, the covariance equalization algorithm was developed [52]. Covariance equalization, which is based on the whitening principle, was introduced as an approximation to the chronochrome algorithm, and it has a number of practical advantages in terms of implementation.

To derive the covariance equalization algorithm, follow chronochrome derivation and then begin with Eq. (4), restated here,

$$
\hat{\mathbf{A}} = \frac{\mathbf{C_{tr}}}{\mathbf{C_r}}.
$$

The cross-covariance can be approximated as the covariance of $\mathbf{C_t}$ [52]. Each image is brought into a new whitened space based on their own covariance matrix. By doing

22

this, registration is less of a concern in the prediction stage because it does not require the cross-covariance.

Eigenvalue decomposition refers to the factoring of a matrix into a diagonal matrix of eigenvalues, and corresponding eigenvectors. Since $\mathbf{C_t}$ and $\mathbf{C_r}$ are covariance matrices and by definition are square, symmetric, and positive semi-definite, they can be written as,

$$\mathbf{C_t} = \Phi_t \Lambda_t \Phi_t^T = \Phi_t \Lambda_t^{1/2} \Phi_t^T \Phi_t \Lambda_t^{1/2} \Phi_t^T,$$

$$\mathbf{C_r} = \Phi_r \Lambda_r \Phi_r^T = \Phi_r \Lambda_r^{1/2} \Phi_r^T \Phi_r \Lambda_r^{1/2} \Phi_r^T,$$

where Φ_t and Φ_r are orthogonal eigenvector matrices and Λ_t and Λ_r are diagonal matrices of eigenvalues resulting from the eigenvalue decomposition of the covariance matrices. Then, the symmetric square root of the covariance matrices can be whitened through the transformation $\Phi \Lambda^{-1/2} \Phi^T$

$$\mathbf{C_t} = \Phi_t \Lambda_t^{1/2} \Phi_t^T,$$

$$\mathbf{C_r} = \Phi_r \Lambda_r^{1/2} \Phi_r^T.$$

The estimate for covariance equalization of $\mathbf{A}$ is then

$$\hat{\mathbf{A}} = \frac{\mathbf{C_t}}{\mathbf{C_r}} \tag{5}$$

$$\hat{\mathbf{A}} = \frac{\Phi_t \Lambda_t^{1/2} \Phi_t^T}{\Phi_r \Lambda_r^{1/2} \Phi_r^T} \tag{6}$$

$$\hat{\mathbf{A}} = \frac{\mathbf{C_t}^{1/2}}{\mathbf{C_r}^{1/2}} \tag{7}$$

$$\hat{\mathbf{A}} = \mathbf{C_t}^{1/2} \mathbf{C_r}^{-1/2} \tag{8}$$

To equalize the mean vectors, the estimate for $\hat{\mathbf{b}}$ is given again by Eq. (3).

2.4.2.3   Local co-registration adjustment

To account for co-registration errors between the reference and test images, Theiler and Wohlberg [53] describe a method that extends any test statistic for anomalous change and minimizes that test statistic for pixels in the reference image that are in the neighborhood of the test image pixel under evaluation. It does so by comparing the measurement of vector $\mathbf{r}$ in the reference image with a 3x3 window of its corresponding vector $\mathbf{t}$ in the test image. Then, the nearest neighbor with the most anomalous relationship is the mis-registered compensated pixel. Local Co-Registration Adjustment (LCRA) includes both symmetric (independent of the direction of minimization) and sub-pixel variants of the algorithm. It assumes that a true anomalous change is independent of the direction of the minimization and therefore the minimization is performed in both directions (*i.e.*, $\mathbf{r}$ to $\mathbf{t}$, or vice versa) where the maximum of the resulting minima is selected as the final results. Finally, the sub-pixel LCRA redefines the optimization windows to include fractional pixel shifts. This is applied using interpolation to resample the images at higher resolution prior to processing.

2.4.2.4   Change detector summary

The notions of changes that are significantly different or unimportant vary by application, which makes it difficult to directly select one from the plurality of CD routines. There is no optimal CD routine and the procedure that is most appropriate depends upon the application (persistent ISR, target tracking, etc.) and the data (image quality, geography of study area, etc.). In addition, the choice of CD routine for the application should include *a priori* knowledge of the OCs in order to define the appropriate techniques that reveal significant change. This aspect is important for CD as it eventually determines if the data, the features, or the detector are cost effective.

2.4.3 Thresholding

Thresholding is a fundamental method applied in many image processing and detection methods. If the change output level exceeds a given threshold, the pixel is regarded as a change pixel. Setting the threshold is a crucial step. If set too high, it will suppress the detection of significant changes. If set too low it will swamp the change map with spurious changes. A typical thresholding routine is modeled in Fig. 8.
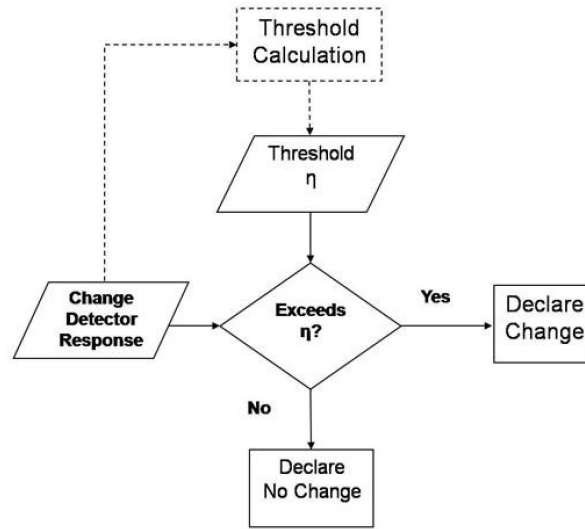
Figure 8. Typical thresholding routine.

Per the framework diagram in Fig. 4, responses from the detector optionally undergo a thresholding stage directly or after post processing. When accomplished directly after the detector, it serves to reduce the amount of information processed in the post-processing stage. If accomplished after the first stage of post-processing, it is used to refine a filtered response (due, *e.g.*, to classification) for potentially improved results. Regardless of when the threshold is applied, before or after post-processing, the method produces a binary change mask. As such, potential objects of interest (significant changes) are separated from the background. The binary image mask

(B) identifies the changed region [6] where

$$
B = \begin{cases} 1 & \text{if significant change,} \\ 0 & \text{otherwise.} \end{cases}
$$

For most CD methods in the literature, the threshold routine is not explicitly defined and there is no theoretical way for setting it ahead of time because of the complexity of the background clutter. Thresholds are typically computed globally or locally and often based on hypothesis testing. Global threshold routines operate on all pixels in the image whereas local threshold routines operate on a subset of the change information. Both approaches use spatial and/or spectral information for the assessment. However, the spectral information tends to be more robust in high noise environments. Ortiz-Rivera *et al.* [17] demonstrated that the local thresholding methodology improved CD results in their HSCD experiment.

Knowing what to look for in an image might simplify estimating the threshold, but trial-and-error is the most common approach. Several thresholding methodologies have been proposed in the literature; however, few of them are specific to CD. Rosin [24] describes four different methods for selecting CD thresholds; either the noise or the signal is modeled, and the model covers either the spatial or intensity distribution characteristics. Spatial features, such as texture and local variance, can help with establishing the CD threshold [54], but this implies that user objectives are determined prior to the design of the change analysis problem. Rosin does conclude that the most promising methods are spatial but adds more extensive testing and quantitative assessment is required.

Regardless of the specific technique used, *a priori* knowledge regarding the data and the application is helpful in selecting a relevant threshold. Approaches to determine the threshold values are still an active area of research and are most often

integrated into the post-processing stage.

2.4.4   Post-processing

Post-processing can occur on the change output prior to thresholding or after thresholding on the filtered change responses (Fig. 3). Post-processing accomplished at either point serves to improve the candidate change mask. The initial binary mask generated after thresholding can highlight insignificant changes and post-processing refines the results potentially improving accuracy.

The simplest techniques post-process the change mask with standard binary image processing operations. Morphological operations are commonly used as a tool for extracting information from an image to describe regional shapes; morphology is a way of giving *meaning* to a certain region in an image [6]. Post-processing applied to the binary image has the advantage of reducing false alarm probabilities at low computational cost. However, standard binary image processing operations may not always be valid in CD [55].

Zhang *et al.* [23] use the minimum noise fraction (MNF) to post-processing the raw CD response in order to separate signal from noise. The change output is then processed with a Markov Random Field (MRF) model [56] for the threshold step incorporating contextual information to improve accuracy and reliability. Lee *et al.* [27] investigate the feasibility of incorporating symbolic reasoning to remove insignificant changes due to shadows, clouds and partial occlusion of existing objects. Their overall CD system concept includes a change interpretation node which applies rules in a hypothesis-driven fashion to the change output to determine the relevance of that change. In general, the symbolic reasoning concept is not well defined, nor does it represent a variety of applications.

Decision fusion is also used in post-processing to mitigate false alarms. Decision

fusion is the combination of two or more algorithms and is most often applied to the change detector. The results of each CD routine are compared and their contribution to the final decision is weighted to be more or less significant than the others. A decision fusion step logically combines the final change/no change locations then correlates those from each change detector. All weighted outputs are then thresholded, at which point additional false alarms, and perhaps some true detections, are filtered out. Fig. 9 provides an illustration of a conventional decision fusion system. For each pixel in the change image there is consensus as to whether or not it contains significant change from the reference image. (This concept and figure was motivated by Hall and Llinas's [4] tutorial on data fusion.)
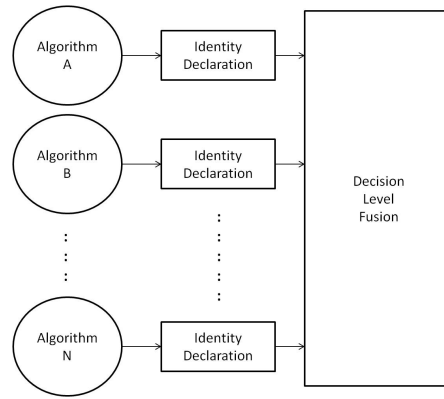
Figure 9. **Conventional decision fusion schema. Image motivated by Hall and Llinas's [4].**

Other post-processing false alarm mitigation routines use geographic information system (GIS) data [57, 58] to enable the delivery of quantified or stratified change maps that are consistent with change product delivery [40]. (A GIS is a system that captures, stores, analyzes, manages, and presents data that are linked to location.) The advantage of using GIS is the ability to incorporate different data sources into change analysis methods, thereby providing a better understanding and identification of the changes that have occurred in a geographic area of interest. The more prominent work by Zhang *et al.* [58] puts forward a holistic strategy of CD based on remote

sensed images and GIS data and claims it addresses the shortcomings of traditional methods, such as the error accumulation and error transfer caused by pre-processing techniques such as data co-registration and feature extraction. The result is improved accuracy and reliability of the change results.

Post-processing can also be in the form of visual-quality improvement to aid the image analyst in assessing CD results. Much of the filtering and post-processing is performed to enhance visual characteristics of images. HS visualization is a distinct but related problem to band reduction. Visualization techniques render either enhanced true color or false color images derived from the HS image, typically in an unsupervised manner [36]. Resolution enhancement aims to compensate for the typical low spatial resolution of HS sensors, primarily by fusing additionally available imagery or performing spatial superresolution [59]. The result is a HS cube with increased spatial resolution which greatly aids visualization for inquiry of the performance in CD results.

2.4.5 Analysis/Assessment

2.4.5.1 Overview

Analysis and assessment is important when developing a CD system and that assessment occurs by comparing results with a truth image mask (a verified ground truth pixel map). Accuracy assessment techniques in CD originate from those of remote sensing image classification. It is natural to extend the accuracy assessment techniques for processing a temporarily stationary image to that of multi-temporal images.

Rosin [60] comments that accurate ground truth is essential either through the use of synthetic imagery or annotation and an image analyst. However, it is often difficult, if not impossible, to collect reliable ground reference due to cost, time,

and accessibility of the study site. Three general approaches to obtain ground truth references are field survey, acquisition of airborne high-resolution imagery (HRI), and visual interpretation. The first two approaches incur a large cost and the third may not be accurate. Since the ground truth data provides a reference point, the thresholding aspect in CD can be tested for correctness of the change results. As described previously, incorporating GIS information can improve the end-to-end CD system results. GIS further provides convenient tools for multi-source data processing and is effective in handling the CD analysis using multi-source data [13].

2.4.5.2 Error matrix, receiver operating characteristic (ROC) curve, and area under the ROC curve (AUC)

The performance of a CD algorithm can be evaluated visually and quantitatively based on application needs. The truth reference and a visual interpretation combination can provide a sense of performance. However, an image analyst may find that the change map requires extensive examination of imagery to assess the relation of the true change. Among the quantitative assessment techniques for analysis of change masks, the most efficient and widely used are the error matrix [13], the receiver operating characteristic (ROC) [61] curve, and the area under the ROC curve (AUC) [62].

Oort [63] describes the common change/no change error matrix used in analyzing results. Here, CD is equivalent to a two-class classification problem. A typical error matrix for a two-class classification problem is illustrated in Fig. 10. As shown, the error matrix is compiled into a table with two rows and two columns that report the number of false positives, false negatives, as well as the complementary true positives and true negatives.

	Classes assigned by change detector/threshold		
True Classes	True Positives (TP)	False Positives (FP)	TP + FP
	False Negatives (FN)	True Negatives (TN)	FN + TN
	TP + FN	FP + TN	TP + TN

Figure 10. Typical change detection error matrix.

The error matrix provides a means to calculate accuracy from both the perspective of the system and the consumer. The accuracy rate refers to the percentage of correct predictions when compared with the actual classifications in the test data. Additionally accuracies, such as producer's and consumer's accuracy, are easily computed from the error matrix. Producer's accuracy is an expression of errors of omission, or false dismissals (for example, from the perspective of CD, labeling a pixel classified as no change when in fact it is change). Consumer's accuracy is an expression of errors of commission, false alarms (for example, again from the perspective of CD, labeling a pixel as change when in fact it is not).

ROC's (Fig. 11) are generally interpreted in one of two ways. If ROC one dominates ROC two, then system one performs better than system two across the entire operating range [64, 65]. If ROC one and ROC two cross, the interpretation is that system one performs better than system two over different portions of the operating range [66]. ROC curves are obtained from binary hypothesis testing by using several threshold values [7, 67].

Bradley in [62] (and others) suggest using the area under the ROC curve (AUC). The ROC is generated in the normal way and the area is estimated using techniques such as the trapezoidal integration method [62]. The AUC is not without its problems.

Namely, it summarizes the ROC curve with a single number and loses the ROC's granularity. It does, however, provide a way to distinguish between two systems when the ROC of one system crosses the ROC of another system (*i.e.*, one ROC does not dominate the other ROC).
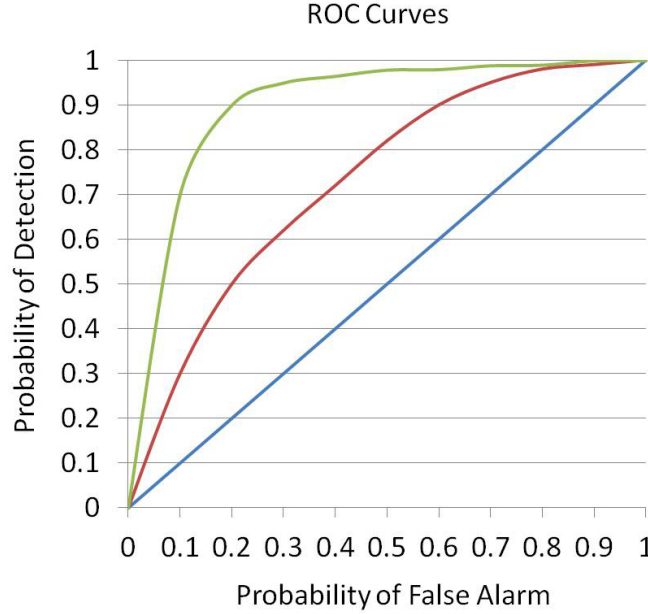
Figure 11. Three hypothetical ROC curves. The probability of detection (P_D) is plotted against the probability of false alarm (P_{FA}) based on changes to a detection threshold. A value of 0.5 (blue line) suggests random guesses while a value of 1 indicates correct classification; as the curves (red and green) approach the value of $P_D = 1$ and $P_{FA} = 0$, the detector performance is said to improve.

In order to evaluate the quality of a change mask independent of the choice of thresholding, the evolution of the detection probability as a function of the false alarm probability may be evaluated against the ground truth data. The ground truth is scored against the binary threshold image and can include different scoring methodologies such as proximity, touch, target centroid, blob centroid, vote and pixel-level (Fig. 12).
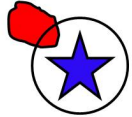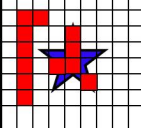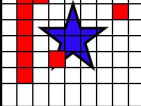
	Proximity • A blob within the immediate vicinity of the target counts as a detection. • This method only requires the center plus radius target mask. • It is good for drawing attention to a region containing targets. • This allows large, sprawling blobs to be counted as detections.
	Touch • The blob of pixels must touch the target. • This is the Proximity Method with tight boundaries. • The target masks must be regular or irregular polygons. • This method allows large, sprawling blobs to be counted as detections.
	Target Centroid • The blob must touch the center of target. • It ensures that some pixels are on the target. • This method only needs the center position of the target mask. • This allows large, sprawling blobs to be counted as detections.
	Blob Centroid • The center of the blob must touch the target. • This is one of the most conservative approaches. • It ensures that some pixels are on the targets. • This method works well with any type of target mask.
	Vote • There must be a certain percent of pixels on the target to count as a detection. • This method should have detailed target masks (irregular polygons). • This procedure must evaluate performance on a pixel-by-pixel basis.
	Pixel Level • Any pixel on the target mask counts as a detection. • This is the Vote Method without a percent-of-pixels threshold. • It is extremely lenient; only one pixel is required to touch the target.

Figure 12. Possible scoring methodologies used during assessment [5].

Accuracy assessment provides benefits in the CD framework including the decision of choosing the specific methodologies of each segment of the processing chain and reporting the overall reliability of the CD system. There is still a need for research in accuracy assessment for CD, especially where the ground reference data is insufficient or impossible to obtain.

2.4.6 Discussion

The contribution of the framework presented here is another step toward understanding the design space of CD systems by extracting the crucial processing steps in each processing stage. From both a research and implementation perspective, the analysis shows how each stage can be decomposed and implemented as part of an end-to-end CD system. For the researcher, the framework enables one to understand

and compare their individual CD research efforts (within a specific method specified in the framework) in different end-to-end CD systems. For the user, the framework helps the analyst choose specific methods for each process in the CD processing chain to achieve best results.

2.5   Stereo geometry

Stereo vision is often considered a form of image registration because the aim is to correlate a secondary image (change image) with a reference image and both require some form of correspondence algorithm. The distinction is that in the image registration case, the process lies in estimating a transformation that spatially aligns two images. However, in stereo vision the aim is to utilize the stereo geometry to locate the disparity between corresponding points, allowing the creation of 3-Dimensional (3D) data. Similar to image registration, stereo vision encounters its fair share of difficulties during correspondence matching. Some problems commonly endured by stereo algorithms include occlusions, perspective distortion, and illumination variation.

Stereo vision refers to the ability to infer information on the 3D structure and distance of a scene from two or more images taken from different viewpoints. Typical stereo vision systems solve two problems: correspondence and reconstruction [68]. Stereo correspondence is a well-understood problem in computer vision, with numerous applications including the previous mentioned image registration problem. The reconstruction problem, given a number of corresponding points in both images and geometry of the stereo pair, permits development of a 3D map of the scene.

Stereo matching methods try to solve the stereo correspondence problem. This dissertation aims to use stereo matching to identify all homologous pixels in the reference and change image pair to yield a parallax approximation [69, 70]. The stereo correspondence problem is solved by matching points between a stereo pair

of images. For every point in the reference image of the stereo pair, a matching
point is found in the test image of the stereo pair. This match is described by a
translation vector from the reference pixel in the reference image to the test pixel in
the test image (Fig. 13). Typical depth applications devise a disparity map from the
translation vectors.
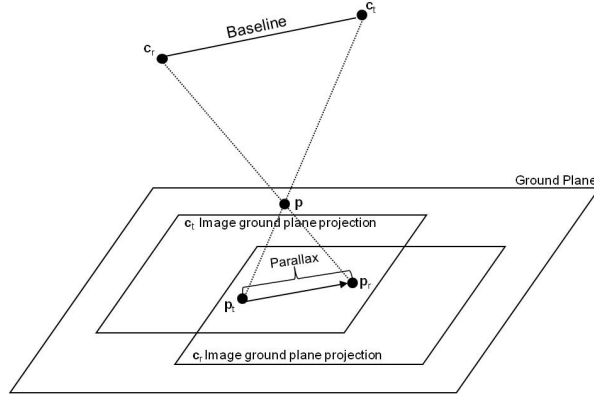
Figure 13. Depiction of residual displacement or parallax.

Matching corresponding points in each image can be a computational burden
within a 2-Dimensional (2D) array. In order to simplify the search, epipolar geometry
is often exploited. Epipolar geometry interprets the projective relationship for the
stereo pair. Hartley [71] describes the epipolar geometry of two views where a point
in one view defines an epipolar line in the other view on which the corresponding
point lies. Fig. 14 depicts the epipolar geometry for a stereo pair. The 3D point
$\mathbf{p}$ is imaged in two views, at $\mathbf{p}_r$ in the reference image and $\mathbf{p}_t$ in the test image.
The epipoles are designated by $\mathbf{e}_r$ and $\mathbf{e}_t$ which is defined by the intersection of the
line joining the image centers, $\mathbf{c}_r$ and $\mathbf{c}_t$. Thus the matching of points is somewhat
simplified as the epipolar geometry enables the search for corresponding points only
along corresponding image lines. The epipolar constraint restricts the search for the
match of a point in one image along the corresponding epipolar line in another image.
Thus the search for correspondences is reduced to a 1-dimensional (1D) problem.

35

Alternatively, false matches due to occlusions can be rejected by verifying whether or not a candidate match lies on the corresponding epipolar line.
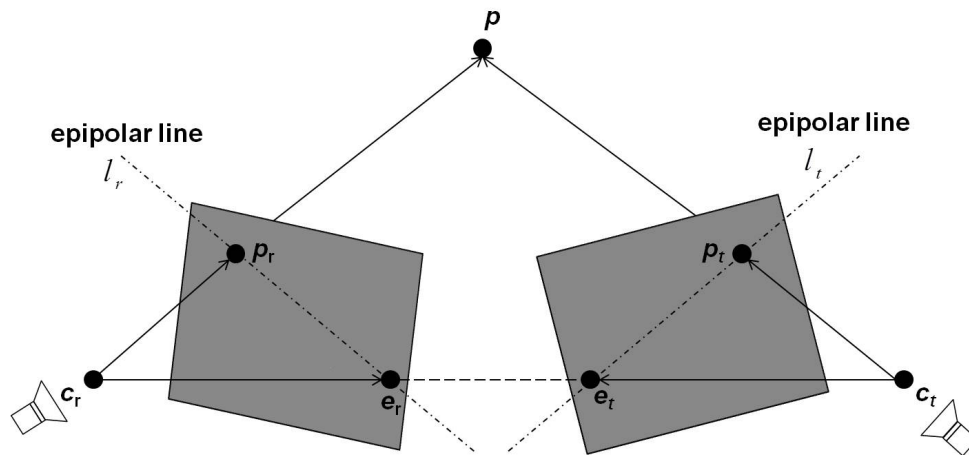
Figure 14. Depiction of the epipolar geometry for a stereo pair. The 3D point p is imaged in two views, at p_r in the reference image and p_t in the test image. The epipoles are designated by e_r and e_t which is defined by the intersection of the line joining the image centers, c_r and c_t.

Correspondence algorithms aim to describe a pixel, or area, from the image data that can be used to efficiently perform a similarity measure between the multi-view imagery. There are two steps in establishing a stereo correspondence: (1) select (manually or automatically) image pixel locations to match and (2) determine the similarity of that match. There are a large number of proposed descriptors for automatic pixel selection and associated similarity measures which utilize different local image features (*e.g.*, pixel intensities, color, texture, edges, etc).

In performance comparison of different descriptors, [72] shows that (SIFT) is one of the most stable and reliable feature detection algorithms. An overview of the SIFT keypoint descriptor's construction is provided where a complete description of the SIFT algorithm can be found in [73]. The SIFT descriptor is based on a monochromatic or gray-scale image representation. SIFT features are local histograms of gradient directions computed over different parts of the keypoint region. It computes the gradient vector for each pixel in the keypoint's pixel neighborhood and builds

36

a normalized orientation histogram of gradient directions to create a 128-dimension vector for feature correspondence. Orientation invariance is achieved by estimating the dominant orientation of the local image patch and is normalized for invariance to changes in illumination. The SIFT process of generating keypoints is performed in two steps: (1) feature detection and (2) feature extraction. Feature detection or keypoint detection is simply the process of locating salient points and/or regions from images, in order to construct useful local image descriptors. Other important attributes of a reliable and meaningful salient keypoint is that it must be invariant to image transformation, such as scale, rotation, and affine transform, in addition to perspective transformation, illumination, and brightness variations. Feature extraction is that local descriptors are computed on the region around each keypoint detected by the keypoint detection process. The local invariant feature descriptors are formed by the local image gradients measured at the selected scale in the region around each keypoint. In general, extracted features must be highly distinctive and tolerant to image noise, changes in illumination, uniform scaling, rotation, and changes in viewing direction.

The second step is determining the match through a similarity measure to provide spatial correspondence. Various similarity measures exist (*e.g.*, sum of absolute differences, cross-correlation coefficient, mutual information) for typical feature correspondence methodologies. The objective of the present work is to improve HSCD by eliminating the false parallax change. As such, stereo correspondence is utilized, not for image registration in the pre-processing stage of the CD processing chain, but to account for parallax thus eliminating false change. Specifically, a correspondence search is made between the reference and test image pair to measure the parallax or the apparent shift of a 3D point, $\mathbf{p}$, above the ground plane against the ground plane. The difference between the position of the pixel in the reference image and the

position of the pixel in the test image on the ground plane identified as the coordinates of the corresponding point of $\mathbf{p}$ provide an estimate of the parallax shift. The parallax direction associated with this estimate is a key component in the parallax-compensation algorithm developed in this research.

III. Change Detection Accounting for Mis-registration and Parallax Errors

This chapter presents a new method to account for image mis-registration and parallax-induced false detections in HSCD. A generalized likelihood ratio test (GLRT) is constructed to provide a change test statistic for change at each pixel in the temporal hyperspectral image pair, and the unit square restricted form of bilinear interpolation [74] is used to account for estimates of image mis-registration for the sub-pixel case. This baseline approach is then modified to incorporate an estimate of the parallax direction in order to mitigate false alarms due to parallax effects between the same two hyperspectral image pairs. The organization of this chapter follows this same basic construction.

3.1 Accounting for image mis-registration

3.1.1 Deriving the mis-registration generalized likelihood ratio test (GLRT)

In the following derivations, lower-case boldface characters represent vectors, and upper-case boldface characters represent matrices. Consider a hyperspectral sensor that makes two observations of a scene in the form of a hyperspectral image composed of K-element spectra made at spatial locations defined by an image coordinate (x, y). The image coordinate can be characterized in any domain, such as ground plane or angular coordinates, but (x, y) is used to represent spatial pixel indices in this dissertation. The reference image is denoted as $\mathbf{r}(x, y)$ and the test image as $\mathbf{t}(x, y)$ where $\mathbf{r}(x, y) \in \Re^K$, $\mathbf{t}(x, y) \in \Re^K$. Typically, hyperspectral images are indexed as matrices where the two-dimensional spatial nature is collapsed into one dimension; however, the two-dimensional spatial relationships are explicitly maintained here in

order to capture spatial mis-registration impacts.

Define the set of local sub-pixel mixtures using the unit square restricted form of the bilinear mixture model around a reference spectrum [74] $\mathbf{r}(x, y)$ as

$$\{\mathbf{m}[(x, y); \alpha_x, \alpha_y] : |\alpha_x| \leq 1, |\alpha_y| \leq 1\}, \tag{9}$$

where

$$\mathbf{m}[(x, y); \alpha_x, \alpha_y] = \begin{cases} \mathbf{r}(x, y) & \text{if } \alpha_x = \alpha_y = 0 \\ (1 - \alpha_x)(1 - \alpha_y)\mathbf{r}(x, y) + (1 - \alpha_x)\alpha_y\mathbf{r}(x, y + 1) & \\ \quad + \alpha_x(1 - \alpha_y)\mathbf{r}(x + 1, y) + \alpha_x\alpha_y\mathbf{r}(x + 1, y + 1) & \text{if } \alpha_x > 0, \alpha_y > 0 \\ (1 + \alpha_x)(1 - \alpha_y)\mathbf{r}(x, y) + (1 + \alpha_x)\alpha_y\mathbf{r}(x, y + 1) & \\ \quad - \alpha_x(1 - \alpha_y)\mathbf{r}(x - 1, y) - \alpha_x\alpha_y\mathbf{r}(x - 1, y + 1) & \text{if } \alpha_x < 0, \alpha_y > 0 \\ (1 + \alpha_x)(1 + \alpha_y)\mathbf{r}(x, y) - (1 + \alpha_x)\alpha_y\mathbf{r}(x, y - 1) & \\ \quad - \alpha_x(1 + \alpha_y)\mathbf{r}(x - 1, y) + \alpha_x\alpha_y\mathbf{r}(x - 1, y - 1) & \text{if } \alpha_x < 0, \alpha_y < 0 \\ (1 - \alpha_x)(1 + \alpha_y)\mathbf{r}(x, y) - (1 - \alpha_x)\alpha_y\mathbf{r}(x, y - 1) & \\ \quad + \alpha_x(1 + \alpha_y)\mathbf{r}(x + 1, y) - \alpha_x\alpha_y\mathbf{r}(x + 1, y - 1) & \text{if } \alpha_x > 0, \alpha_y < 0 \end{cases}$$

Assume (α_x, α_y) are unknown but can range from zero to one pixel. Also assume that a specific test spectrum $\mathbf{t}(x, y)$ maps to a specific reference spectrum $\mathbf{r}(x, y)$ within some unknown mis-registration $(\Delta x, \Delta y)$.

Consider the situation where there is some unknown mis-registration $(\Delta x, \Delta y)$ between the reference and test images such that the prediction image is required to be of the form

$$\mathbf{p}(x, y | \Delta x, \Delta y) = \mathbf{A}\mathbf{r}(x + \Delta x, y + \Delta y) + \mathbf{b}. \tag{10}$$

The assumption is that the amount of mis-registration can vary from pixel to pixel according to some known or assumed statistics defined by a probability density function (PDF) $f_{\Delta X, \Delta Y}(\Delta x, \Delta y)$. Letting $\mathbf{n}$ represent the sensor noise, the hypothesis

test corresponding to CD is written as

$$H_0 \quad : \quad \mathbf{e}(x,y) = \mathbf{t}(x,y) - \mathbf{p}(x,y|\Delta x, \Delta y) + \mathbf{n} = 0,$$

$$H_1 \quad : \quad \mathbf{e}(x,y) = \mathbf{t}(x,y) - \mathbf{p}(x,y|\Delta x, \Delta y) + \mathbf{n} \neq 0. \tag{11}$$

The GLRT test statistic for this detection problem is given by the maximum likelihood ratio [75] defined as

$$l(x,y) = \frac{\max\limits_{\mathbf{A},\mathbf{b},\Delta x, \Delta y} f_e[\mathbf{e}(x,y;\mathbf{A},\mathbf{b},\Delta x, \Delta y)|H_1]}{\max\limits_{\mathbf{A},\mathbf{b},\Delta x, \Delta y} f_e[\mathbf{e}(x,y;\mathbf{A},\mathbf{b},\Delta x, \Delta y)|H_0]} \tag{12}$$

where $f_{\mathbf{e}}(\cdot)$ is the probability density function for the residual error ($\mathbf{e}$) in Eq. (12). Under the alternative hypothesis, for anomalous CD, there is no *a priori* information; therefore, the maximum likelihood estimates are the measurements themsleves and the numerator in Eq. (12) is constant. Eq. (12) is written as

$$f_e[\mathbf{e}(x,y;\mathbf{A},\mathbf{b},\Delta x, \Delta y)|H_0] = f_e[\mathbf{e}(x,y;\mathbf{A},\mathbf{b})|H_0, \Delta x, \Delta y] f_{\Delta X, \Delta Y}(\Delta x, \Delta y). \tag{13}$$

The assumption is $\mathbf{n} \sim N(0, \mathbf{C}_n)$, as such

$$f_e[\mathbf{e}(x,y;\mathbf{A},\mathbf{b})|H_0, \Delta x, \Delta y] = \frac{1}{(2\pi)^{K/2}} \frac{1}{|\mathbf{C}|^{1/2}} e^{-\frac{1}{2}[\mathbf{t}(x,y) - \mathbf{p}(x,y|\Delta x, \Delta y)]\mathbf{C}_n^{-1}[\mathbf{t}(x,y) - \mathbf{p}(x,y|\Delta x, \Delta y)]}, \tag{14}$$

where $\mathbf{C}_n$ is the expected sensor noise covariance matrix in the resulting difference image. Further, let (σ_x, σ_y) be the root mean squared mis-registration errors and assume a normal prior PDF for the unknown residual spatial mis-registration

$$f_{\Delta X, \Delta Y}(\Delta x, \Delta y) = \frac{1}{2\pi \sigma_x \sigma_y} e^{-\frac{\Delta x^2}{2\sigma_x^2}} e^{-\frac{\Delta y^2}{2\sigma_y^2}}. \tag{15}$$

The transformation parameters $\mathbf{A}$ and $\mathbf{b}$ determined by chronochrome (CC) are assumed to represent the maximum likelihood estimates, or the covariance equalization (CE) estimates are used as a substitute. The change test statistic can be transformed into the log-likelihood by $d(x, y) = \ln l(x, y)$. Substituting the results from Eq. (12) to Eq. (15) into this log-likelihood test statistic and ignoring constant terms that are not data-dependent, the GLRT test statistic becomes

$$d(x,y) = \min_{\Delta_x, \Delta_y} \left\{ [\mathbf{t}(x,y) - \mathbf{p}(x,y|\Delta x, \Delta y)]^T \mathbf{C}_n^{-1} [\mathbf{t}(x,y) - \mathbf{p}(x,y|\Delta x, \Delta y)] + \frac{\Delta x^2}{\sigma_x^2} + \frac{\Delta y^2}{\sigma_y^2} \right\}. \tag{16}$$

Performing the minimization dictated by the GRLT CD statistic in Eq. (16) is straightforward for integer pixel mis-registration. This minimization provides the exact same result as the CC test statistic when the sample covariance matrix of the difference image $\mathbf{C}_e$ is used as an estimate of the noise covariance matrix $\mathbf{C}_n$, but with a minimization over different test-to-reference pixel associations. For non-integer pixel mis-registration increments, some interpolation procedure is needed. In the general case where the mis-registration could be more than one pixel, the minimization needs to be performed over integer pixel shifts and performed over the interpolation between integer pixel shifts. The assumption is that the image-to-image registration step preceding CD can provide a residual mis-registration better than one pixel (which is typically the case) and only explicitly deal with the case of sub-pixel shifts, which makes the mathematics more transparent. It should be noted, however, that the method developed under this assumption is easily generalized to scenarios with mis-registration errors of multiple pixels by applying it over multiple pixel regions. This generalization is useful for extending the methods described to address other phenomenon such as resampling errors introduced during image-to-image registration or parallax errors caused by different viewing geometries (addressed later in this Chapter).

The prediction $\mathbf{p}(x, y|\Delta x, \Delta y)$ is estimated in two dimensions from a bilinear mixture of the four nearest neighbors of $\mathbf{p}(x, y)$. The Δx and Δy provide the absolute measures of the mis-registration, which can be positive or negative, and include both full pixel and fractional pixel shifts. However, if the cost function is limited to fractional mis-registration and adjusted for each quadrant around the pixels then $\alpha = |\Delta x|$ and $\beta = |\Delta y|$, thus the estimate is given by

$$\hat{\mathbf{p}}(x, y; Q|\Delta x, \Delta y) = (1 - \alpha)(1 - \beta)\mathbf{p}_{00}^Q + \alpha(1 - \beta)\mathbf{p}_{10}^Q + (1 - \alpha)\beta\mathbf{p}_{01}^Q + \alpha\beta\mathbf{p}_{11}^Q. \quad (17)$$

where $\mathbf{p}_{00}^Q, \mathbf{p}_{10}^Q, \mathbf{p}_{01}^Q$, and $\mathbf{p}_{11}^Q$ are the bilinear mixtures using the restricted form for quadrant Q (Table 3) around a center pixel. Note in Table 3 that the location of the four pixels mixed in the bilinear interpolation are merely changed to maintain α and β between zero and one.

Table 3. Definition of the bilinear mixture spectra in each of the four quadrants.

Quadrant II (Q=II)	Quadrant I (Q=I)
$\mathbf{p}_{00} = \mathbf{A}\mathbf{r}(x, y) + \mathbf{b}$	$\mathbf{p}_{00} = \mathbf{A}\mathbf{r}(x, y) + \mathbf{b}$
$\mathbf{p}_{10} = \mathbf{A}\mathbf{r}(x - 1, y) + \mathbf{b}$	$\mathbf{p}_{10} = \mathbf{A}\mathbf{r}(x + 1, y) + \mathbf{b}$
$\mathbf{p}_{01} = \mathbf{A}\mathbf{r}(x, y + 1) + \mathbf{b}$	$\mathbf{p}_{01} = \mathbf{A}\mathbf{r}(x, y + 1) + \mathbf{b}$
$\mathbf{p}_{11} = \mathbf{A}\mathbf{r}(x - 1, y + 1) + \mathbf{b}$	$\mathbf{p}_{11} = \mathbf{A}\mathbf{r}(x + 1, y + 1) + \mathbf{b}$
Quadrant III (Q=III)	Quadrant IV (Q=IV)
$\mathbf{p}_{00} = \mathbf{A}\mathbf{r}(x, y) + \mathbf{b}$	$\mathbf{p}_{00} = \mathbf{A}\mathbf{r}(x, y) + \mathbf{b}$
$\mathbf{p}_{10} = \mathbf{A}\mathbf{r}(x - 1, y) + \mathbf{b}$	$\mathbf{p}_{10} = \mathbf{A}\mathbf{r}(x + 1, y) + \mathbf{b}$
$\mathbf{p}_{01} = \mathbf{A}\mathbf{r}(x, y - 1) + \mathbf{b}$	$\mathbf{p}_{01} = \mathbf{A}\mathbf{r}(x, y - 1) + \mathbf{b}$
$\mathbf{p}_{11} = \mathbf{A}\mathbf{r}(x - 1, y - 1) + \mathbf{b}$	$\mathbf{p}_{11} = \mathbf{A}\mathbf{r}(x + 1, y - 1) + \mathbf{b}$

Defining $q(x, y; \Delta x, \Delta y)$ as the function within the braces minimized in Eq. (16),

$$q(x, y; \Delta x, \Delta y) = [\mathbf{t}(x, y) - \hat{\mathbf{p}}(x, y|\Delta x, \Delta y)]^T \mathbf{C}_n^{-1}[\mathbf{t}(x, y) - \hat{\mathbf{p}}(x, y|\Delta x, \Delta y)]$$
$$+ \frac{\Delta x^2}{\sigma_x^2} + \frac{\Delta y^2}{\sigma_y^2}, \quad (18)$$

the test statistic is found by minimizing $q(x, y; \alpha, \beta)$ over each quadrant Q=1...4

independently subject to the constraints, $0 \leq \alpha \leq 1$ and $0 \leq \beta \leq 1$.

Inserting Eq. (17) into Eq. (18), then multiplying and collecting terms, the cost function is rewritten as

$$q(x, y; \alpha, \beta, Q) = a^Q \alpha^2 \beta^2 + b^Q \alpha^2 \beta + c^Q \alpha \beta^2 + d^Q \alpha \beta + e^Q \alpha^2$$
$$+ f^Q \beta^2 + g^Q \alpha + h^Q \beta + k^Q, \qquad (19)$$

where Q again denotes the quadrant (note that the f above is a coefficient and not a PDF) and the coefficients of the cost function are data-dependent defined as

$$a^Q = [\mathbf{p}_{01}^Q + \mathbf{p}_{10}^Q - \mathbf{p}_{00}^Q - \mathbf{p}_{11}^Q]^T \mathbf{C}_n^{-1} [\mathbf{p}_{01}^Q + \mathbf{p}_{10}^Q - \mathbf{p}_{00}^Q - \mathbf{p}_{11}^Q]$$

$$b^Q = -2[\mathbf{p}_{10}^Q - \mathbf{p}_{00}^Q]^T \mathbf{C}_n^{-1} [\mathbf{p}_{01}^Q + \mathbf{p}_{10}^Q - \mathbf{p}_{00}^Q - \mathbf{p}_{11}^Q]$$

$$c^Q = -2[\mathbf{p}_{01}^Q - \mathbf{p}_{00}^Q]^T \mathbf{C}_n^{-1} [\mathbf{p}_{01}^Q + \mathbf{p}_{10}^Q - \mathbf{p}_{00}^Q - \mathbf{p}_{11}^Q]$$

$$d^Q = 2[\mathbf{t}(x, y) - \mathbf{p}_{00}^Q]^T \mathbf{C}_n^{-1} [\mathbf{p}_{01}^Q + \mathbf{p}_{10}^Q - \mathbf{p}_{00}^Q - \mathbf{p}_{11}^Q] + 2[\mathbf{p}_{10}^Q - \mathbf{p}_{00}^Q]^T \mathbf{C}_n^{-1} [\mathbf{p}_{01}^Q - \mathbf{p}_{00}^Q]$$

$$e^Q = [\mathbf{p}_{10}^Q - \mathbf{p}_{00}^Q]^T \mathbf{C}_n^{-1} [\mathbf{p}_{10}^Q - \mathbf{p}_{00}^Q] + \frac{1}{\sigma_x^2}$$

$$f^Q = [\mathbf{p}_{01}^Q - \mathbf{p}_{00}^Q]^T \mathbf{C}_n^{-1} [\mathbf{p}_{01}^Q - \mathbf{p}_{00}^Q] + \frac{1}{\sigma_x^2}$$

$$g^Q = -2[\mathbf{t}(x, y) - \mathbf{p}_{00}^Q]^T \mathbf{C}_n^{-1} [\mathbf{p}_{10}^Q - \mathbf{p}_{00}^Q]$$

$$h^Q = -2[\mathbf{t}(x, y) - \mathbf{p}_{00}^Q]^T \mathbf{C}_n^{-1} [\mathbf{p}_{01}^Q - \mathbf{p}_{00}^Q]$$

$$k^Q = [\mathbf{t}(x, y) - \mathbf{p}_{00}^Q]^T \mathbf{C}_n^{-1} [\mathbf{t}(x, y) - \mathbf{p}_{00}^Q]$$

Since Eq. (19) is a fourth order polynomial, numerical methods are required to perform the constrained minimization in each quadrant. Such methods depend on computing the gradient vector and Hessian matrix, defined as (dropping the quadrant

index Q for notational ease)

$$\nabla q = \begin{bmatrix} \frac{\partial q}{\partial \alpha} \\ \frac{\partial q}{\partial \beta} \end{bmatrix}, \tag{20}$$

$$H = \begin{bmatrix} \frac{\partial^2 q}{\partial \alpha^2} & \frac{\partial^2 q}{\partial \beta \alpha} \\ \frac{\partial^2 q}{\partial \alpha \beta} & \frac{\partial^2 q}{\partial \beta^2} \end{bmatrix}. \tag{21}$$

The first order partial derivatives are defined as

$$\frac{\partial q}{\partial \alpha} = 2a\alpha\beta^2 + 2b\alpha\beta + c\beta^2 + d\beta + 2e\alpha + g \,,$$
$$\frac{\partial q}{\partial \beta} = 2a\alpha^2\beta + b\alpha^2 + 2c\alpha\beta + d\alpha + 2f\beta + h. \tag{22}$$

The second order partial derivatives are defined as

$$\frac{\partial^2 q}{\partial \alpha^2} = 2a\beta^2 + 2b\beta + 2e,$$
$$\frac{\partial^2 q}{\partial \beta^2} = 2a\alpha^2 + 2c\alpha + 2f,$$
$$\frac{\partial^2 q}{\partial \alpha \beta} = 4a\alpha\beta + 2b\alpha + 2c\beta + d,$$
$$\frac{\partial^2 q}{\partial \beta \alpha} = 4a\alpha\beta + 2b\alpha + 2c\beta + d. \tag{23}$$

The minimization problem requires a suitable optimization algorithm to solve but the convergence rate can be slow; hence in the next section an analytical solution is derived to support an inexpensive computational approximation.

3.1.2 Derivation of a quadratic approximation to the GLRT test statistic

A second order Taylor series expansion of the nonlinear cost function $q(x, y; \alpha, \beta)$ can be used to support an analytical minimization and closed-form test statistic that should support a more computationally efficient change detector. For each of the four quadrants, first find the unconstrained minimum based on a quadratic approximation about the center of the quadrant (approximated by assuming the center pixel), $\alpha = \beta = \frac{1}{2}$. If this unconstrained minimum, designated as (α^*, β^*), falls within the constraint boundaries $(0 < \alpha^* < 1$ and $0 < \beta^* < 1)$, it is accepted as the constrained minimum. Otherwise, the minimum among each of the four boundaries of the quadrant is determined, and the smallest value of the four is accepted as the constrained minimum. No approximation is required along these quadrant boundaries as the cost function is quadratic for a fixed α or β.

The two-dimensional function $q(x, y; \alpha, \beta)$ can be expanded about a point (α', β') into a second order Taylor series as

$$
\begin{aligned}
q(x, y, \alpha', \beta') = q(x, y, \alpha', \beta') &+ \left.\frac{\partial q}{\partial \alpha}\right|_{\alpha',\beta'} \frac{1}{1!}(\alpha - \alpha') + \left.\frac{\partial q}{\partial \beta}\right|_{\alpha',\beta'} \frac{1}{1!}(\beta - \beta') \\
&+ \left.\frac{\partial^2 q}{\partial \alpha^2}\right|_{\alpha',\beta'} \frac{1}{2!}(\alpha - \alpha')^2 + \left.\frac{\partial^2 q}{\partial \beta^2}\right|_{\alpha',\beta'} \frac{1}{2!}(\beta - \beta')^2 \\
&+ \left.\frac{\partial^2 q}{\partial \alpha \partial \beta}\right|_{\alpha',\beta'} \frac{2}{2!}(\alpha - \alpha')(\beta - \beta') + \dots
\end{aligned}
\tag{24}
$$

$$
\tag{25}
$$

Taking the derivatives with $\alpha' = \beta' = \frac{1}{2}$ and keeping only the terms explicitly shown

in Eq. (25), the quadratic approximation is

$$
\begin{aligned}
q(x, y; \alpha', \beta') \approx & \left[\frac{a}{16} + \frac{b+c}{8} + \frac{d+e+f}{4} + \frac{g+h}{2} + k \right] \\
& + \left[\frac{a+c}{4} + \frac{b+d}{2} + e + g \right]\left(\alpha - \frac{1}{2} \right) + \left[\frac{a+b}{4} + \frac{c+d}{2} + f + h \right]\left(\beta - \frac{1}{2} \right) \\
& + \left[\frac{a}{4} + \frac{b}{2} + e \right]\left(\alpha - \frac{1}{2} \right)^2 + \left[\frac{a}{4} + \frac{c}{2} + f \right]\left(\beta - \frac{1}{2} \right)^2 \\
& + [a + b + c + d]\left(\alpha - \frac{1}{2} \right)\left(\beta - \frac{1}{2} \right)
\end{aligned} \tag{26}
$$

where the variables $a, b, c, d, e, f, g, h, k$ are defined in Section 3.2.1. Setting the derivatives of this quadratic approximation with respect to both α and β to zero, the unconstrained minimum is located at α^* and β^* per Eq. (27) and Eq. (28).

$$
\alpha^* = \frac{(8d+8c+8b+8a)h+(-16f-8c-4a)g+(4c+8b+8a)f+(-4c-2b-4a)d-2c^2+(-2b-3a)c-2b^2-4ab-2a^2}{(32e+16b+8a)f+(16c+8a)e-8d^2+(-16c-16b-16a)d-8c^2+(-8b-12a)c-8b^2-12ab-6a^2} \tag{27}
$$

$$
\beta^* = -\frac{(16e+8b+4a)h+(-8d-8c-8b-8a)g+(-8c-4b-8a)e+(2c+4b+4a)d+2c^2+(2b+4a)c+2b^2+3ab+2a^2}{(32e+16b+8a)f+(16c+8a)e-8d^2+(-16c-16b-16a)d-8c^2+(-8b-12a)c-8b^2-12ab-6a^2} \tag{28}
$$

The minima along the four boundaries are computed directly per Eq. (23). For $(\alpha_0, 0)$:

$$
\left. \frac{\partial q}{\partial \alpha} \right|_{(\alpha_0, 0)} = 0 \quad \rightarrow \quad \alpha_0 = -\frac{g}{2e} \tag{29}
$$

For $(0, \beta_0)$:

$$
\left. \frac{\partial q}{\partial \alpha} \right|_{(0, \beta_0)} = 0 \quad \rightarrow \quad \beta_0 = -\frac{h}{2f} \tag{30}
$$

47

For $(\alpha_1, 1)$:

$$\left.\frac{\partial q}{\partial \alpha}\right|_{(\alpha_1,1)} = 0 \quad \rightarrow \quad \alpha_1 = -\frac{(c+d+g)}{2(a+b+e)} \tag{31}$$

For $(1, \beta_1)$:

$$\left.\frac{\partial q}{\partial \alpha}\right|_{(1,\beta_1)} = 0 \quad \rightarrow \quad \beta_1 = -\frac{(b+d+h)}{2(a+c+f)} \tag{32}$$

The minimum test statistic for a given quadrant $Q = 1 \ldots 4$ is then given by

$$d_Q(x,y) = \begin{cases} q(x,y;\alpha^*,\beta^*,Q) & 0 \le \alpha^* \le 1 \text{ and } 0 \le \beta^* \le 1 \\ \min\{q(x,y;\alpha_0,0,Q), q(x,y;0,\beta_0,Q), q(x,y;\alpha_1,1,Q), q(x,y;1,\beta_1,Q)\} & \text{otherwise} \end{cases} \tag{33}$$

The test statistic $d(\cdot)$ is then the overall minimum over the four quadrants: $d(x,y) = \min\ d(x,y;Q)$ for $Q\ =\ 1\ \ldots\ 4$.

3.1.3 Comparison with local co-registration adjustment

The foundation for both the LCRA and the GLRT quadratic approximation is based on an anomalous change detector. The LCRA performs an interpolation of the test statistic, which becomes quadratic. The GLRT results in a fourth-order (quartic) test statistic that is approximated as a quadratic using a second order Taylor series expansion. Both algorithms seek to improve detection performance for mis-registered data. Unlike LCRA (Section 2.4.2.3), the GLRT-based approach developed in this dissertation incorporates a prior probability density function for the residual mis-registration, which might be critical in inhibiting the local optimization from finding minima that are improbable relative to the statistics of the actual mis-registration between images. The GLRT further allows one to incorporate additional prior information regarding the image mis-registration statistics, as might be available to compensate for other image acquisition or image preprocessing errors. The GLRT

formulation results in a closed form solution for the test statistic that is minimized relative to the unknown local shift parameters. One major downfall of LCRA from the perspective of this research is that it does not provide a basis to extend it to address the parallax problem. The GLRT approach provides the generality to incorporate *a priori* information about the expected direction of parallax errors.

3.2 Accounting for image parallax

To account for parallax, there is first a need to explicitly extend the method to handle multiple pixel shifts. In this case, let

$$\Delta x = \tilde{m} + \alpha,$$

$$\Delta y = \tilde{n} + \beta,$$

where $(\tilde{m}, \tilde{n})$ are whole pixel shifts and $0 \leq \alpha \leq 1$ and $0 \leq \beta \leq 1$. As such, the Quadrant I algorithm is used in all cases (see Section 3.1.1) with the addition of the $(\tilde{m}, \tilde{n})$ pixel shift. That is, the sub-pixel part of $(\Delta x, \Delta y)$ is always assumed to be in the positive x and y direction from the full-pixel $(\tilde{m}, \tilde{n})$ part. Following Eq. (10), the prediction then becomes

$$\hat{\mathbf{p}}(x, y; |\tilde{n}, \tilde{m}, \alpha, \beta) = (1 - \alpha)(1 - \beta)\mathbf{p}_{00} + \alpha(1 - \beta)\mathbf{p}_{10} + (1 - \alpha)\beta\mathbf{p}_{01} + \alpha\beta\mathbf{p}_{11}, \quad (34)$$

where, per Table 3

$$\mathbf{p}_{00}(x, y, \tilde{m}, \tilde{n}) = \mathbf{Ar}(x + \tilde{m}, y + \tilde{n}) + \mathbf{b},$$

$$\mathbf{p}_{10}(x, y, \tilde{m}, \tilde{n}) = \mathbf{Ar}(x + \tilde{m} + 1, y + \tilde{n}) + \mathbf{b},$$

$$\mathbf{p}_{01}(x, y, \tilde{m}, \tilde{n}) = \mathbf{Ar}(x + \tilde{m}, y + \tilde{n} + 1) + \mathbf{b},$$

$$\mathbf{p}_{11}(x, y, \tilde{m}, \tilde{n}) = \mathbf{Ar}(x + \tilde{m} + 1, y + \tilde{n} + 1) + \mathbf{b}.$$

Note that $\tilde{m}$ and $\tilde{n}$ can be positive or negative.

Let ϕ be the direction of the observed parallax, σ_p the RMS parallax error, and σ_m the RMS residual mis-registration, both measured in pixels. The expected RMS parallax error can be estimated by the change in viewing geometry and the 3-D scene structure. This is shown in Fig. 15 where $\tilde{d}_r$ is the occlusion from incidence angle θ_r and $\tilde{d}_t$ is the occlusion from incidence angle θ_t. Thus $\tilde{d}_t - \tilde{d}_r$ can be estimated as the parallax error, σ_p, due to the height, h, of the building structure. The mis-
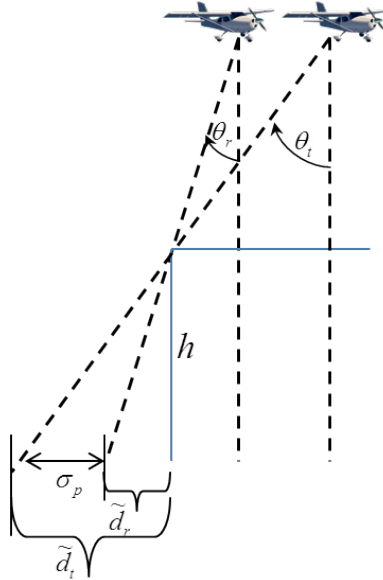
Figure 15. Image depicting geometry of acquiring a test and reference image.

registration is assumed to be direction-independent such that $\sigma_m = \sigma_x = \sigma_y$. This

assumption is made for two reasons. First, a priori estimates of the misregistration parameters σ_x and σ_y are unavailable and the values are difficult to determine without extensive studies. Second, there is convenience in making the mathematics cleaner given the assumption. In the principal point coordinates $(\Delta\xi, \Delta\eta)$ where $\Delta\xi$ is along the parallax direction and $\Delta\eta$ is orthogonal to it, the prior PDF for the local misregistration is

$$f_{\Delta\xi,\Delta\eta}(\Delta\xi, \Delta\eta) = \frac{1}{(2\pi)}\frac{1}{\sigma_m\sqrt{\sigma_m^2 + \sigma_p^2}}e^{-\frac{\Delta\eta^2}{2(\sigma_m^2+\sigma_p^2)}}e^{-\frac{\Delta\xi^2}{2(\sigma_m^2)}}. \tag{35}$$

In Fig. 16(left), the Δx and Δy axes represents the zero parallax case which is rotated about the origin through an acute angle ϕ resulting in the $\Delta\xi$ and $\Delta\eta$ axes corresponding to the direction of parallax (ξ) and the orthogonal direction (η). The angle ϕ is the direction of parallax relative to the x-axis. Thus, a given point $\mathbf{p}$ has coordinates $(\Delta x, \Delta y)$ in the image coordinate system and $(\Delta\xi, \Delta\eta)$ in the parallax-oriented coordinate system. In Fig. 16(right), the line from the origin to the the point $\mathbf{p}$ has magnitude r and angle θ in the $(\Delta\xi, \Delta\eta)$ coordinate system. Using this observation, the relationship between $\Delta\xi$ and $\Delta\eta$ to Δx and Δy (as illustrated in Fig. 16(right)) is given by

$$\Delta\xi = r\cos\theta \qquad\qquad \Delta\eta = r\sin\theta,$$
$$\Delta x = r\cos(\phi + \theta) \qquad\qquad \Delta y = r\sin(\phi + \theta).$$

Using the addition formula for the cosine and sine functions, Δx and Δy are expressed
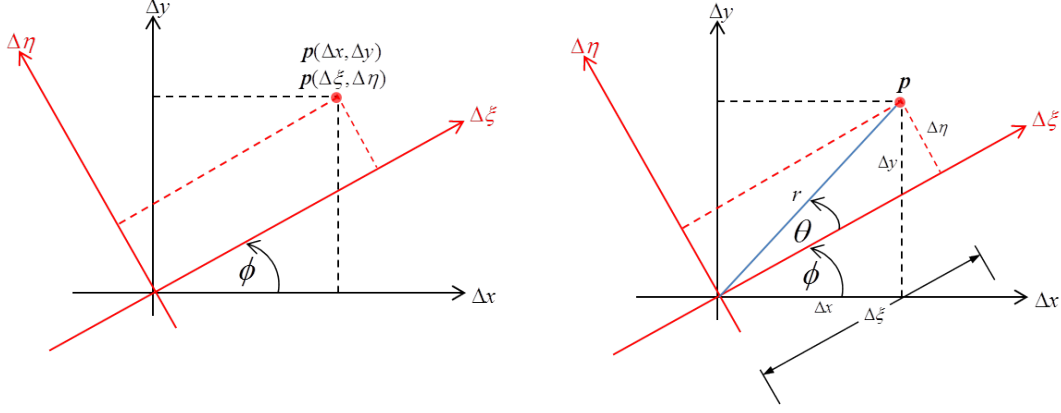
Figure 16. The relationship between coordinates as they describe the same point, p in the plane. (left) The Δx and Δy axes have been rotated about the origin through an angle ϕ (the parallax direction angle) to produce the $\Delta \xi$ and $\Delta \eta$ axes. (right) $\Delta \xi$ and $\Delta \eta$ are related to Δx and Δy through the blue line from the origin to point P.

in terms of $\Delta \xi$ and $\Delta \eta$ as

$$\Delta x = r \cos(\phi + \theta) = r(\cos \phi \cos \theta - \sin \phi \sin \theta),$$

$$\Delta x = (r \cos \theta) \cos \phi - (r \sin \theta) \sin \phi,$$

$$\Delta x = \Delta \xi \cos \phi - \Delta \eta \sin \phi. \tag{36}$$

and

$$\Delta y = r \sin(\phi + \theta) = r(\sin \phi \cos \theta + \cos \phi \sin \theta),$$

$$\Delta y = (r \cos \theta) \sin \phi - (r \sin \theta) \cos \phi,$$

$$\Delta y = \Delta \xi \sin \phi + \Delta \eta \cos \phi. \tag{37}$$

Solving for $\Delta \xi$ and $\Delta \eta$ in Eq. (36) and Eq. (37) yields

$$\Delta \xi = \Delta x \cos \phi + \Delta y \sin \phi, \tag{38}$$

$$\Delta \eta = -\Delta x \sin \phi + \Delta y \cos \phi. \tag{39}$$

After expressing the new coordinates from axis rotation, an evolution of the normal

prior PDF is formulated to include an expected parallax orientation (ϕ) and RMS parallax error (σ_p). Thus, substituting Eq. (38) and Eq. (39) into Eq. (35) yields

$$f_{\Delta x, \Delta y}(\Delta x, \Delta y) = \frac{1}{(2\pi)} \frac{1}{\sigma_m \sqrt{\sigma_m^2 + \sigma_p^2}} e^{-\frac{(\Delta x \cos\phi + \Delta y \sin\phi)^2}{2(\sigma_m^2 + \sigma_p^2)}} e^{-\frac{(-\Delta x \sin\phi + \Delta y \cos\phi)^2}{2(\sigma_m^2)}}. \tag{40}$$

The original cost function in Eq. (18) then becomes

$$q(\tilde{m}, \tilde{n}, \alpha, \beta) = [\mathbf{t}(x,y) - \mathbf{p}(x,y|\Delta x, \Delta y)]^T \mathbf{C}_n^{-1} [\mathbf{t}(x,y) - \mathbf{p}(x,y|\Delta x, \Delta y)]$$
$$+ \frac{(\Delta x \cos\phi + \Delta y \sin\phi)^2}{(\sigma_m^2 + \sigma_p^2)} + \frac{(-\Delta x \sin\phi + \Delta y \cos\phi)^2}{\sigma_m^2} \tag{41}$$

For each $(\tilde{m}, \tilde{n})$ the polynomial is of the same form as before but the penalty terms are different. They are found by expanding two quadratic equations

$$(\Delta x \cos\phi + \Delta y \sin\phi)^2, \tag{42}$$

$$(-\Delta x \sin\phi + \Delta y \cos\phi)^2. \tag{43}$$

The coefficients used in the cost function described in Eq. (19) now become

$$a = [\mathbf{p}_{01} + \mathbf{p}_{10} - \mathbf{p}_{00} - \mathbf{p}_{11}]^T \mathbf{C}_n^{-1} [\mathbf{p}_{01} + \mathbf{p}_{10} - \mathbf{p}_{00} - \mathbf{p}_{11}]$$

$$b = -2[\mathbf{p}_{10} - \mathbf{p}_{00}]^T \mathbf{C}_n^{-1} [\mathbf{p}_{01} + \mathbf{p}_{10} - \mathbf{p}_{00} - \mathbf{p}_{11}]$$

$$c = -2[\mathbf{p}_{01} - \mathbf{p}_{00}]^T \mathbf{C}_n^{-1} [\mathbf{p}_{01} + \mathbf{p}_{10} - \mathbf{p}_{00} - \mathbf{p}_{11}]$$

$$d = 2[\mathbf{t}(x,y) - \mathbf{p}_{00}]^T \mathbf{C}_n^{-1} [\mathbf{p}_{01} + \mathbf{p}_{10} - \mathbf{p}_{00} - \mathbf{p}_{11}] + 2[\mathbf{p}_{10} - \mathbf{p}_{00}]^T \mathbf{C}_n^{-1} [\mathbf{p}_{01} - \mathbf{p}_{00}]$$
$$- \frac{\sigma_p^2}{\sigma_m^2} \frac{2\cos\phi\sin\phi}{\sigma_m^2 + \sigma_p^2}$$

$$e = [\mathbf{p}_{10} - \mathbf{p}_{00}]^T \mathbf{C}_n^{-1} [\mathbf{p}_{10} - \mathbf{p}_{00}] + \frac{\sigma_m^2 + \sigma_p^2\sin^2\phi}{\sigma_m^2(\sigma_m^2 + \sigma_p^2)}$$

$$f = [\mathbf{p}_{01} - \mathbf{p}_{00}]^T \mathbf{C}_n^{-1} [\mathbf{p}_{01} - \mathbf{p}_{00}] + \frac{\sigma_m^2 + \sigma_p^2\cos^2\phi}{\sigma_m^2(\sigma_m^2 + \sigma_p^2)}$$

$$g = -2[\mathbf{t}(x,y) - \mathbf{p}_{00}]^T \mathbf{C}_n^{-1} [\mathbf{p}_{10} - \mathbf{p}_{00}]$$
$$+ \frac{2\cos\phi(\tilde{m}\cos\phi + \tilde{n}\sin\phi)}{\sigma_m^2 + \sigma_p^2} + \frac{2\sin\phi(\tilde{m}\sin\phi - \tilde{n}\cos\phi)}{\sigma_m^2}$$

$$h = -2[\mathbf{t}(x,y) - \mathbf{p}_{00}]^T \mathbf{C}_n^{-1} [\mathbf{p}_{01} - \mathbf{p}_{00}]$$
$$+ \frac{2\sin\phi(\tilde{m}\cos\phi + \tilde{n}\sin\phi)}{\sigma_m^2 + \sigma_p^2} - \frac{2\cos\phi(\tilde{m}\sin\phi - \tilde{n}\cos\phi)}{\sigma_m^2}$$

$$k = [\mathbf{t}(x,y) - \mathbf{p}_{00}]^T \mathbf{C}_n^{-1} [\mathbf{t}(x,y) - \mathbf{p}_{00}] + \frac{(\tilde{m}\cos\phi + \tilde{n}\sin\phi)^2}{\sigma_m^2 + \sigma_p^2} + \frac{(\tilde{m}\sin\phi - \tilde{n}\cos\phi)^2}{\sigma_m^2}$$

Calculating the parallax direction through stereo correspondence was described previously in Section 2.5. The stereo correspondence method utilized in this work is based on matching SIFT descriptors. The SIFT descriptors are computed and compared using a similarity measure to determine correspondence points. The similarity is defined as the cosine of the angle between SIFT vectors in the reference image and test image as

$$sim(\mathbf{p}_r, \mathbf{p}_t) = \frac{\mathbf{p}_r \cdot \mathbf{p}_t}{||\mathbf{p}_r|| \, ||\mathbf{p}_t||} \tag{44}$$

where $\mathbf{p}_r$ and $\mathbf{p}_t$ are SIFT descriptor vectors from the reference and test images, respectively, and $||\cdot||$ denotes the Euclidean norm. Matching descriptor points between

the reference and test images is accomplished by computing the similarity measure between all feature pairs where the two feature pairs are declared a match when their similarity is within a threshold. For a set of correspondence points, the maximum is the most likely shift for parallax. This eliminates small shifts likely from slight mis-registration. The parallax direction is computed in terms of the coordinate shift, expressed in pixels, by selecting the correspondence points with the largest Euclidean distance between index values,

$$k = \arg\max_i \left(x_{t,i} - x_{r,i}\right)^2 + \left(y_{t,i} - y_{r,i}\right)^2, \qquad (45)$$

where i is the pair of correspondence points under consideration, $(x_{r,i}, y_{r,i})$ and $(x_{t,i}, y_{t,i})$ are the indices of correspondence point i in the reference and test images respectively, and k is the reference and test correspondence point used to determine the parallax angle. Next, the parallax direction angle (ϕ) (shown in Fig. 17) for the given corre-
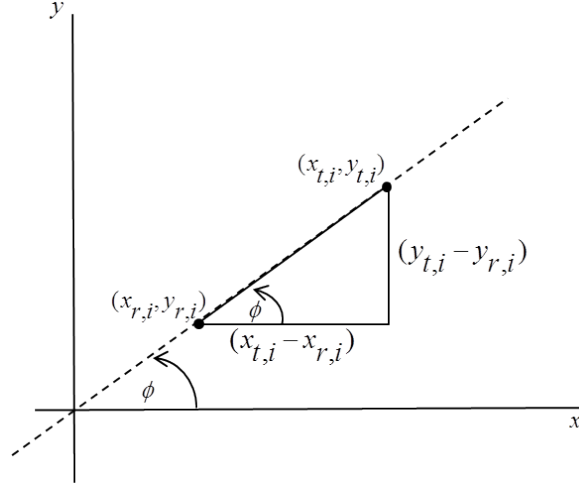
Figure 17. Calculating the parallax direction angle, ϕ, from the calculated correspondence point shift.

spondence point is calculated as

$$\phi = \operatorname{atan}\left(\frac{y_{t,k} - y_{r,k}}{x_{t,k} - x_{r,k}}\right). \qquad (46)$$

55

If the denominator is zero then $\phi = 90°$.

The correspondence points allow a parallax direction angle estimate, ϕ, then to be used in Eq. (41) for computation of the test statistic.

3.3 Summary

This chapter defined two algorithms used to address the problems of image mis-registration and image parallax as they pertain to the CD problem. The mis-registration algorithm incorporates a spatial mis-registration model into a GLRT-based change detector leading to a fourth order polynomial test statistic. A second order Taylor series expansion of the nonlinear cost function is then used to derive a closed-form test statistic to support a more computationally efficient change detector. The second algorithm leveraged the inherent relationship between the reference and test image views and pixel correspondence matching to perform parallax mitigation. This requires a search for correspondence points in order to calculate the parallax angle, ϕ, to determine if in the pixel-level change detector, a true change pixel exists even along the parallax direction.

Chapter IV describes the test data used in algorithm analysis. Algorithm performance of both proposed algorithms are compared to existing anomalous CD schemes.

IV. Experimentation and Results

4.1   Overview

The previous chapters presented necessary background material and derived novel hyperspectral change detection (HSCD) algorithms. In this chapter, hyperspectral data used to detail the algorithms are presented and described. The generalized likelihood ratio test (GLRT) mis-registration compensation algorithm presented in Chapter III is compared with current state-of-the-art anomalous change detection (CD) algorithms, namely chronochrome (CC) and covariance equalization (CE), as well as the local co-registration adjustment (LCRA). The GLRT-based parallax-compensation algorithm is compared to CC, and parameter sensitivity is explored for both GLRT-based algorithms. All of the results presented in this chapter were developed and applied in the MATLAB® software environment.

4.2   Data description

There are two data sets used to evaluate the mis-regristration algorithm, the *Air Force Research Lab (AFRL) tower data* and the Civil Air Patrol (CAP) Airborne Real-time Cueing Hyperspectral Enhanced Reconnaissance (ARCHER) [76] *Mojave data* sets. In particular, a simulated change to the CAP ARCHER [76] *Mojave data* set is used to compare mis-registration compensating change detector results with LCRA. An additional data set is presented and is used for evaluating the parallax compensation algorithm, a synthetic data set generated by the *Digital Imaging and Remote Sensing Image Generation (DIRSIG)* system [77].

4.2.1 Data to evaluate mis-registration-compensating change detection algorithm

4.2.1.1 Tower data

The *tower data* shown in Fig. 18, used for testing the proposed detector, was collected in a controlled manner from a tower using a visible to near infrared (VNIR) hyperspectral imaging spectrometer mounted on a pan and tilt assembly. The spectral range of the imager is $0.46 - 0.9\,\mu m$ and the spatial resolution is approximately $4\,cm$. The *tower data* was collected at Wright Patterson Air Force Base, Ohio. While the data collection effort extended from August 2005 through May 2006, this particular pair was collected on October 14, 2005 near solar noon [78]. Less than one half hour passes between collecting the test and reference image pair thereby limiting illumination and vegetation changes between images. In doing so, any degradation in performance that may occur can be attributed mostly to prediction error due to artificially introduced mis-registration rather than errors introduced by shadowing or vegetation changes [79]. The top two images in Fig. 18 are a color composite of the data. The scene is composed of mostly grass and trees with coated aluminum panels placed along the treeline. One change of interest is identified in the scene, corresponding to a small green tarp bundle added to the test image. The challenge for the CD algorithm is to detect the small change in the presence of mis-registration. A pixel-level truth map for the spatial pixel dimensions (126x126) *tower data* is extracted manually based on the CC test statistic to evaluate the results and is displayed in Fig. 18 (bottom). The truth image represents pixels as black (0) for no change and white (1) for true change. The change target in the truth mask is a rectangular grid of 3x5 pixels with a one pixel *ignore mask* along the outer edge of the change target. An ignore mask identifies pixels around the periphery of the change target that are ignored during scoring to keep them from biasing the results

because the ground truth for these pixels is uncertain. The background consists of 15,841 pixels.
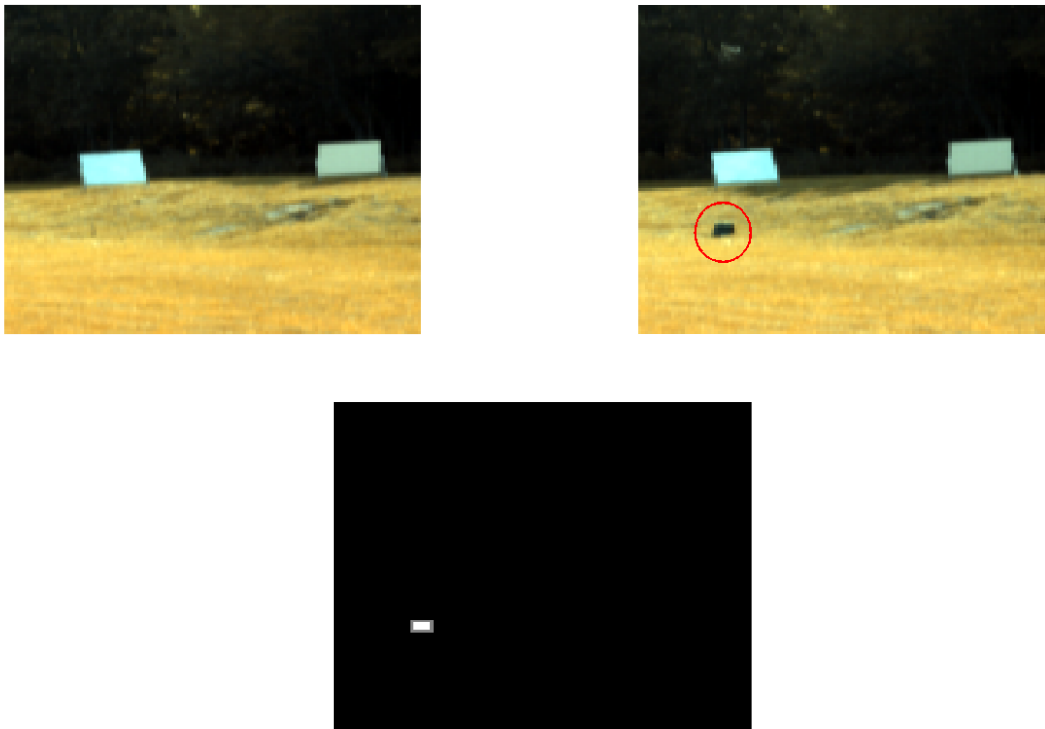
Figure 18. Change pair _tower data_ set used for mis-registration analysis (top). These false color composites are produced from the hyperspectral data cubes by selecting respective red, green and blue bands. Binary target truth mask for the _tower data_ set (bottom).

To test the proposed algorithms, the test image is artificially mis-registered by translating the original high resolution data then mean filtering to simulate fractional pixel shifts as shown in Fig. 19. The test data is shifted one pixel in both the positive x and negative y direction with respect to the reference spatial scene to simulate mis-registration. A sub-pixel mis-registration was introduced by resampling both images (reference and test) with a 2x2 pixel mean filter to create the sub-pixel mis-registration shift. In order to eliminate edge artifacts, the images are cropped to ensure the same number of samples is used to estimate test statistics. Shifting integer pixel amounts for the original high resolution imagery and then synthetically reducing resolution by

averaging full pixel blocks avoids potential spectral interpolation artifacts.
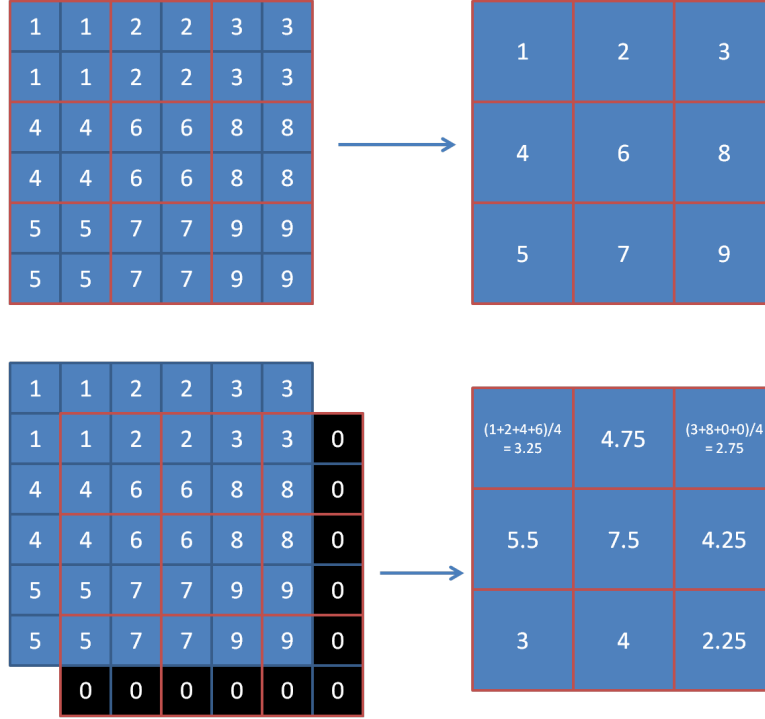
Figure 19. **An example of the simulated mis-registration process. The images on the left represent high resolution imagery. The bottom-left image is shifted prior to performing block averaging. The images on the right represent the new images at a coarser spatial resolution where the bottom image also reflects a simulated $1/2$ pixel shift in the positive x and negative y directions.**

4.2.1.2 Mojave data

CAP ARCHER [76] hyperspectral images were captured at the collection conducted at the National Test Pilot School in Mojave, California. The objective of the collection was to demonstrate the operational utility and baseline the performance of a VNIR hyperspectral sensor for a search and rescue mission. The images with a spatial pixel dimension size of 238x208 are displayed in Fig. 20. Again, a synthetic mis-registration is introduced in order to perform an analysis on the mis-registration compensation algorithm. The same approach for synthetically mis-registering the data is used for this change pair as was described for the *tower data*. Specific spatial portions of the synthetically mis-registered data were swapped to simulated change

occurring between the reference and test images. Fig. 20 shows a synthetic change for testing the algorithms that is created by interchanging a square 9x9 block of pixels from one spatial location in the image to another (see red circled image chips in Fig. 20 right). This provides known true change pixels for algorithm evaluation which can be seen in the truth mask (bottom) where target pixels are represented as white.
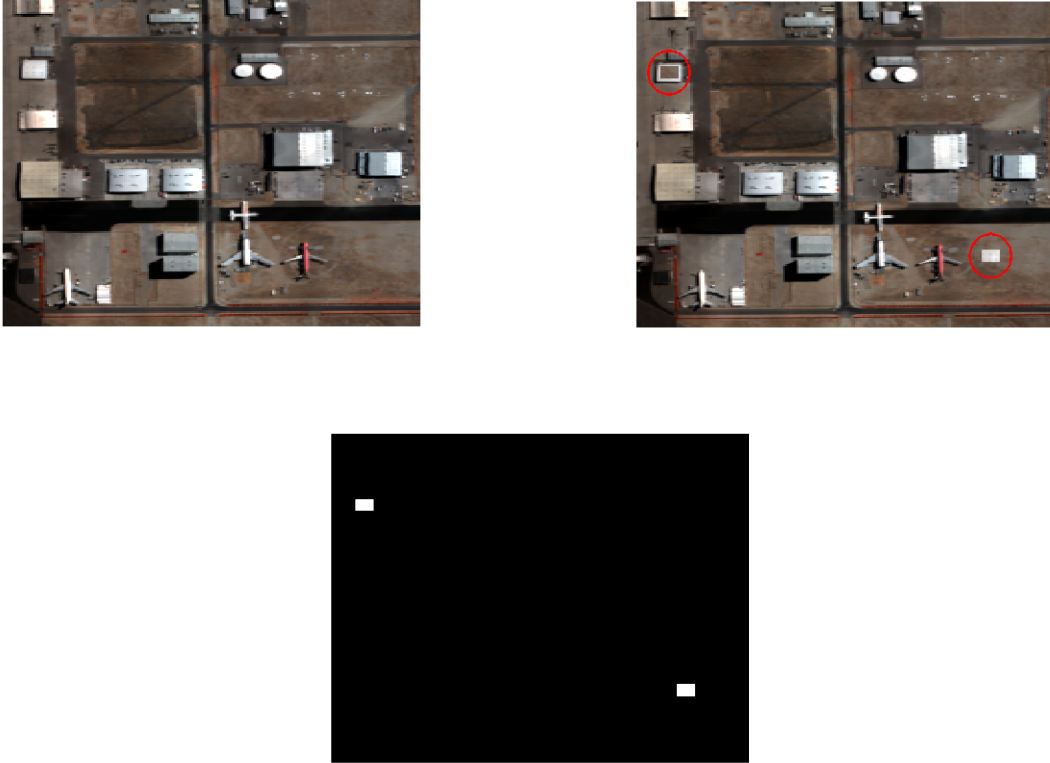
Figure 20. Top images show CAP ARCHER data set with synthetic change. The swapped pixels are shown in red circles on the right image. Bottom image shows the target truth mask.

4.2.2   Data to evaluate parallax-compensating change detection algorithm

4.2.2.1   Synthetic DIRSIG data

The parallax GLRT algorithm is tested on synthetic imagery generated using the DIRSIG system [77]. DIRSIG is a software suite started in the late 1980s at the

Rochester Institute of Technology (RIT) in Rochester, NY. The program predicts imager radiance values using a physics model and ray tracing. The physics model takes into account thermal characteristics, atmospheric properties and distortion, HS imager features and noise, the sensor platform, and the surface composition [77]. The DIRSIG modeler uses actual end-member spectra for in-scene materials, and calculates the spectral response as seen by the sensor for the specific environmental conditions. The software is used by civilian, academic, and defense agencies for various scientific and engineering studies [2, 29, 80–83]. The use of synthetic imagery provides the advantage of having complete truth information and exact positions of the change targets within the scene.

An artificial scene that mimics an Airborne Visible InfraRed Imaging Spectrometer (AVIRIS) sensor with 224 spectral channels ranging from approximately 400 - 2500 nm is constructed to represent an urban scene with elevated structures. The spatial resolution is approximately $0.3m$ and the image spatial size is 311x259. The synthetic scene was constructed to introduce image parallax. The rendered scenes were simulated to collect at 10,000 ft with two different viewing angles: 10° and 20°. The reference and test images are formed with a vehicle departure change occurring between instances (red circles, top of Fig. 21).

The parallax direction is estimated by manually evaluating the building edges. The different off-nadir view angles between the reference and test images results in parallax and this is the manually estimated parallax direction from "building lean" where the sides of the buildings become more visible with an increase in off-nadir viewing angle. The manually estimated parallax direction average is approximately 4 pixels in the upward direction (90°, see Fig. 22).

In addition, the synthetic data allows a controlled environment for knowable ground truth. DIRSIG supports per-pixel truth maps that provide important im-

age formation parameters [77]. The true parallax in this imagery can be calculated from the per-pixel truth maps provided by DIRSIG. The displacement or true pixel shift (tps), in pixels, can be determined by knowing the collection angle, the height of the buildings, and the ground sampling distance (GSD) (Fig. 15). Therefore, a truth mask is developed from the pixel truth information furnished by DIRSIG by calculating Eq. (47) at every pixel

$$\text{tps} = \frac{h \tan \theta_r}{\text{GSD}} - \frac{h \tan \theta_t}{\text{GSD}}, \tag{47}$$

where h is the building height and θ_r and θ_t are the reference and test viewing angles.

The parallax truth mask is shown in Fig. 23, where the colorbar on the right reflects the true value of the local shift. There are a total of 1,562 true parallax pixels. An ignore mask was created for pixels above the ground plane but not on the edge of a structure and are the gray pixels in Fig. 23 . The buildings where the parallax does not occur are considered to be ignore pixels because although the building reveals a shift in the parallax truth map, the algorithm sees 'no change' as it is still of the same material. The ignore pixels account for 8,807 pixels out of the total 80,549 pixels in the image. The background pixels (ground plane pixels) experience no height difference thus is zero and account for 70,180 pixels.
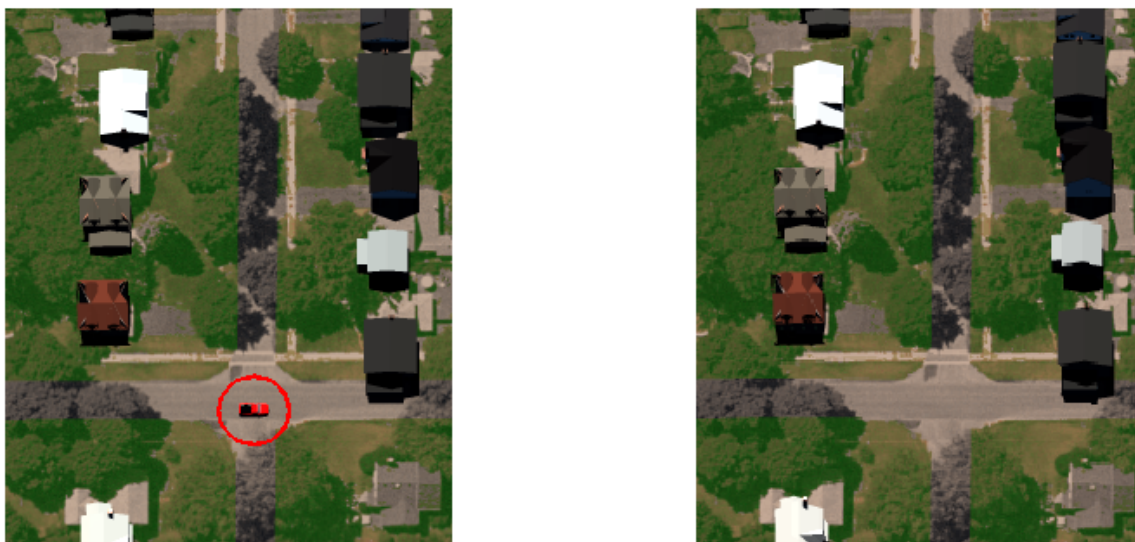
Figure 21. Synthetic reference image of an urban scene with elevated structures and a stationary red vehicle (red circle) taken at a $10°$ viewing angle is displayed upper left. On the upper right is the synthetic test image, captured from an alternate angle ($20°$ viewing angle) with the vehicle no longer in scene.

Figure 22. In-scene building edge from the synthetic reference image (collected at a $10°$ viewing angle) used to manually estimate the parallax direction between images (left images). Synthetic test image (right images) of the same in-scene building but captured from an alternate viewing angle of $20°$ displaying an increase in visibility of the building side with an appraised parallax shift of 4 pixels in the upward direction $(90°)$. Labels on both image chips are pixel values.

4.3 Algorithm implementation details

4.3.1 Mis-registration algorithm implementation

Both the CC and CE anomalous change detectors rely on a linear prediction of the reference image using the statistics from the test image. Assuming this linear relationship exists, a gain matrix $(\hat{\mathbf{A}})$ and offset vector $(\hat{\mathbf{b}})$ are estimated and applied to the reference image to match conditions of the test image. Upon applying the
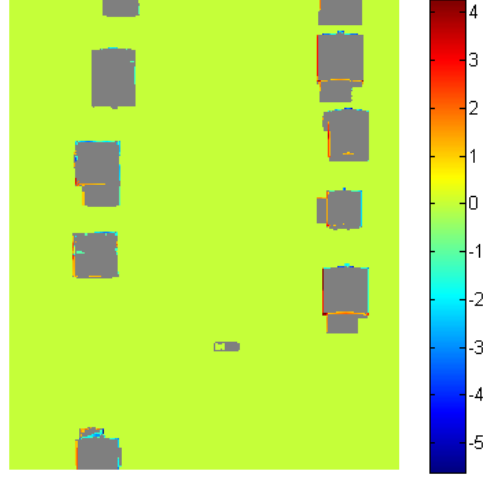
Figure 23. Depiction of parallax truth mask. The parallax effects reside along the building edges. The gray pixels reflect ignore masks so that top pixels of elevated structures are ignored during analysis.

predictor, the difference image between the prediction and test images is obtained, followed by an anomaly detector to determine if a change has occurred. This is the typical process for anomalous CD and is shown in the dotted box in Fig. 24. The remaining blocks in Fig. 24 show the CD process based on the derived GLRT in Section 3.1 where the minimization block corresponds to minimizing the objective function (described in Eq. (19) through a numerical optimization technique or the quadratic approximation in Eq. (26)). This minimization is performed for each of the four quadrants (refer to Table 3) where the minimum over the four quadrants is the minimized test statistic. In Fig. 24, $\mathbf{C}_n$ is the covariance matrix of the difference image based on the CC predictor and σ_x, σ_y are user-specified parameters characterizing the root mean squared (RMS) mis-registration.
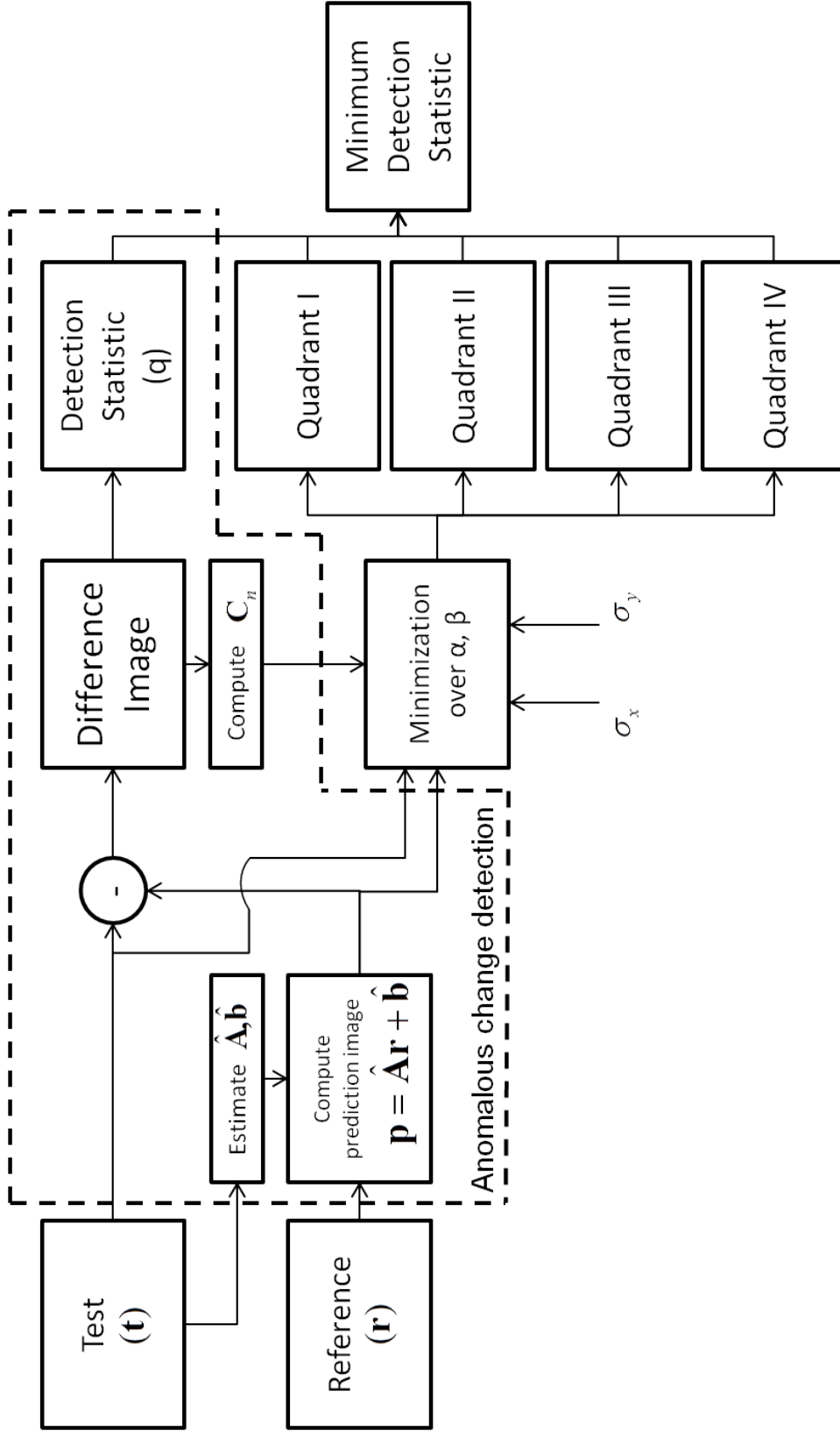
Figure 24. Flow chart for applying the mis-registration GLRT change detection algorithm.

67

The minimization problem defined in this dissertation requires a suitable optimization algorithm to solve. In general, there are two categories of approach: derivative and non derivative. Derivative approaches are based on either the gradient or Hessian (first and second derivatives respectively). Gradient-based approaches, such as steepest/gradient descent (a greedy method), are popular due to ease of problem formulation but tend to converge slowly since movement towards the (possibly local) minimum is linear. Convergence rate is improved through various algorithmic enhancements, such as the addition of a momentum term in back propagation neural networks [84]. Hessian-based approaches generally follow Newton's method (see *e.g.*, [85]), which has a quadratic convergence rate and hence converges much quicker than gradient-based approaches. Variants of Newton's method (*e.g.*, Broyden-Fletcher-Goldfarb-Shanno [86] and Gauss-Newton [87]) are used to overcome certain limitations such as the requirement of the Hessian being positive definite and non-singular. The nature of the problem may require one to seek non derivative-based approaches. Such search algorithms include the class of genetic algorithms and stochastic algorithms (*e.g.*, Simulated Annealing [88]) to name a few. The search literature is vast and myriad good options exist, each with its merits and demerits. A constrained variant [89] of the Nelder-Mead simplex method [90] (a direct search approach) that transforms the constraints and uses the standard unconstrained form for the minimization task, is used in this dissertation.

For a function with $n = 2$ variables, the Nelder-Mead method creates a simplex of $n + 1$ points (a triangle for the spatial problems explored in this research), and performs a search that compares function values at each of the vertices. The vertex where the function takes its largest value is rejected and replaced with a new vertex. A new triangle is formed and the search is continued. The process generates a sequence of triangles, for which the function values at the vertices decrease and the size of the

triangles is reduced locating the coordinates of the minimum point [91].

4.3.2 Parallax-compensation algorithm implementation

The parallax-compensation flow diagram in Fig. 25 is similar to that of the misregistration flow diagram in Fig. 24 in Section 4.3.1 where the anomalous CD process remains unchanged but the minimization process is noticeably different. In Fig. 25 the minimization block minimizes the objective function with the parallax-derived coefficients described in Section 3.2 to include integer pixels shifts.

This minimization is performed for multiple $(\tilde{m}, \tilde{n})$ values where $(\tilde{m}, \tilde{n})$ is established based on ϕ. The search region was set manually for this experiment based on the fact that ϕ is in the vertical direction. Thus, $\tilde{m}$ is small and restricted to $(-1, 0)$ while $\tilde{n}$ is bounded by an assumed $\sigma_p = 4$ pixels $(-2\sigma_p \leq \tilde{n} \leq 2\sigma_p)$.

Note that the search region can very easily be established over a square search region bounded by $-2\sigma_p \leq (\tilde{m}, \tilde{n}) \leq 2\sigma_p$ (illustrated in Fig. 26), however the prior PDF allows the cost function with lower cost in the ϕ direction. Therefore, choosing the search region according to the ϕ estimate would be appropriate (see Fig. 26 illustration for 'low-cost' and 'high-cost' search direction).
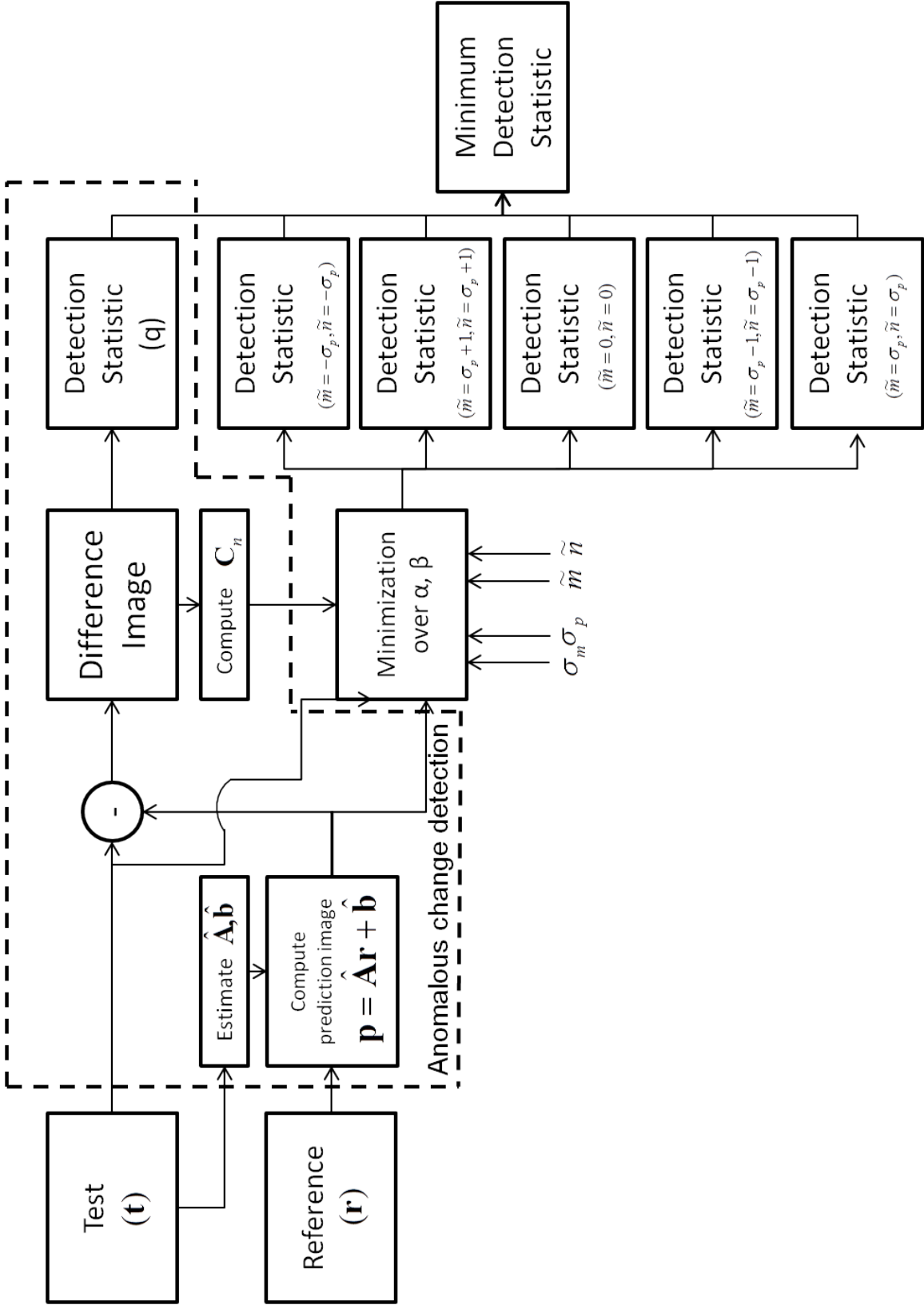
Figure 25. Flow chart for applying the parallax-compensation GLRT change detection algorithm.

70
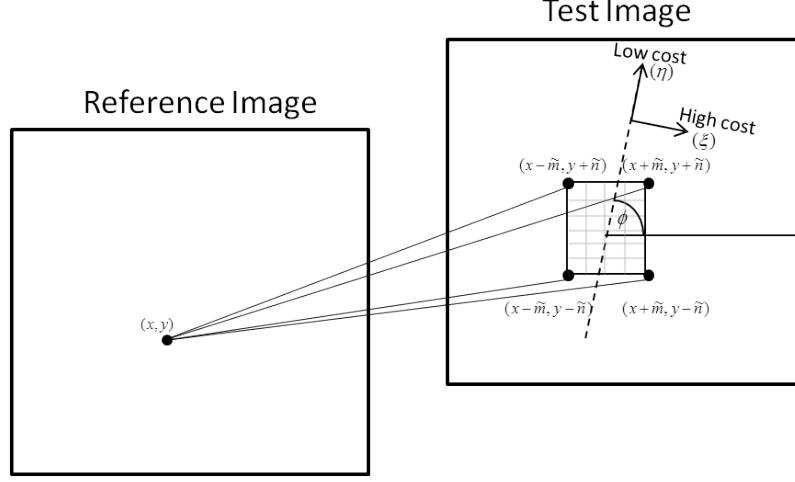
Figure 26. Parallax-compensation algorithm search space defined for parameters $(\tilde{m}, \tilde{n})$.

4.4 Scoring methodology

Pixel-level scoring (described in Section 2.4.5.2) is used to generate the ROC curves describing pixel-level success. For a CD system, the ROC analysis consists of measuring the binary response of the detection system by calculating the probability of detection as

$$P_D = \frac{D}{T}, \tag{48}$$

where D are properly matched pixels and T are true change target pixels and the probability of false alarm with

$$P_{FA} = \frac{M - D}{N - T} \tag{49}$$

where N is the total number of pixels in the image and M is the declared changed pixels at a particular threshold. The (P_{FA}, P_D) pair is one point on the ROC curve. This process is repeated for multiple thresholds where M and D will vary with different thresholds.

At each decision threshold, P_D and P_{FA} are calculated by comparing a binary detection image with a ground-truth mask. In practice, the simplest way to compare the detection image and the truth mask is to make a pixel-level comparison exactly fitting the definitions of P_D and P_{FA}. The manually derived ground-truth mask can be difficult to define and skew performance if not accurate. In particular, edge pixels may be either uncertain or contain a mixture of target and background, especially if mis-registration errors are present. Thus, after deriving the ground-truth pixels based on the baseline CC test statistic, the change target(s) are surrounded with non-penalizing pixels around the change target borders (the ignore mask). The performance is further examined when the ignore mask extends into the target mask to reduce the effect of uncertain edge pixels.

4.5   Experiments and results

Performance analysis occurs in two ways in this dissertation. First is a visual analysis of the detection image. The visual analysis, when combined with the truth mask and knowledge of the CD scenario, helps provide insights into what the change detector is doing on the given set of imagery. It further provides visual confirmation that the algorithms are performing in a manner that makes logical sense. Second is a quantitative analysis by way of the ROC curve and the AUC derived from the ROC curve. The ROC curve is the standard method of performance assessment in the detection literature and is used in this dissertation. In the case there are non-dominating ROC curves, the AUC provides another measure to comapre performance. An exception is for the DIRSIG imagery, where the Signal-to-Clutter Ratio (SCR) is used to show how the clutter from the edge artifacts is reduced by increasing σ_p.

Other performance analysis approaches exist and include histogram-based methods and simply plotting intensity versus a 1-D pixel index. A common histogram-

based method uses a histogram of the change image to determine if modes exist within the detection image that can be post-processed to identify change versus no change. The latter approach is not as common and may be difficult to interpret. These are not pursued in this dissertation.

4.5.1 Mis-registration algorithm

This section describes the results from the mis-registration GLRT algorithm derived in Section 3.1.1 almost exclusively on the *tower data* before considering the *Mojave data*. First, using the CC predictor, the nonlinear optimization results are analyzed to provide evidence that the algorithm and its quadratic approximation are functioning as derived. Second, using the CC predictor, the quadratic approximation results are compared to the nonlinear optimization approach to demonstrate the efficacy of the estimate. Third, using the CE predictor, performance of the quadratic approximation is compared to the CC results. Fourth, the quadratic approximation using the CC predictor is compared with LCRA [53]. Finally, model parameter performance impact is explored using the quadratic approximation.

4.5.1.1 Nonlinear optimization

An inspection of the unthresholded detection image, using the CC predictor, for the mis-registration GLRT algorithm using nonlinear optimization is shown in Fig. 27. After experimenting, the RMS mis-registration parameters were chosen as $\sigma_x = \sigma_y = 0.05$ for computing the test statistic image results for the *tower data* set. The arrows indicate the mis-registration artifacts; the test statistic is visibly lower in Quadrant II which is expected because the mis-registration shift is in that direction. A common scale is used where black and white pixels in the change mask correspond to a test statistic $d_{min\{Q_1,Q_2,Q_3,Q_4\}}(x,y) = 56.9$ and $d_{max\{Q_1,Q_2,Q_3,Q_4\}}(x,y) = 745.5$,

respectively. The detection image can take values in the range $[0, \infty)$. Experiments show that Quadrant II suppresses the edge effects due to the mis-registration and is the correct direction in which the actual mis-registration shift of $\Delta x = 1/2$ and $\Delta y = -1/2$ occurred. Therefore, by choosing the minimum test statistic over the four quadrants detected change caused by mis-registration is reduced.

The uncompensated CC test statistic image (bottom left), test statistic using minimum nonlinear optimization (top), and the test statistic using the known mis-registration (bottom right) are compared in Fig. 28. Uncompensated CC (Fig. 28 bottom left) highlights the impact of the mis-registration effect on CD. This impact is indicated by the two bright white vertical lines on the left and right side of the panel that result in a false declaration of change. When using the GRLT with nonlinear optimization (Fig. 28 top), there is visual evidence that false changes caused by mis-registration are alleviated (note the darker appearance corresponding to a lower test statistic, indicative of being non change pixels). The test statistic using the known mis-registration (Fig. 28 bottom right) represents the minimum of the average pixel spectra for each of the four quadrants as input to the CC algorithm. The edges here offer a lower test statistic and are accomplished using the known (true) mis-registration.

ROC curves are shown in Fig. 29 and it is evident that the false alarm rate is reduced using the proposed GLRT-based method. For similar false alarm rates, the GLRT-based approach provides two to three times the detection performance. For similar detection results, the GLRT-based approach provides one to two orders of magnitude reduction in false alarms. AUC is used to compare the curves in Fig. 29 with the test statistic maps displayed in Fig. 28. A higher value indicates a better quality test statistic map, meaning it is more capable of providing higher accuracy change results. As is seen in Table 4, the AUC for the nonlinear optimization is

higher than the uncompensated CC and the known mis-registration. The fact that the nonlinear optimization approach provides better results than the GLRT using the known mis-registration is most likely due to unaccounted for mis-registration artifacts in the original data set.

Q1 : Nonlinear Optimization

Registration error

Q2 : Nonlinear Optimization

Lower registration error

Q3 : Nonlinear Optimization

Registration error

Q4 : Nonlinear Optimization

Registration error
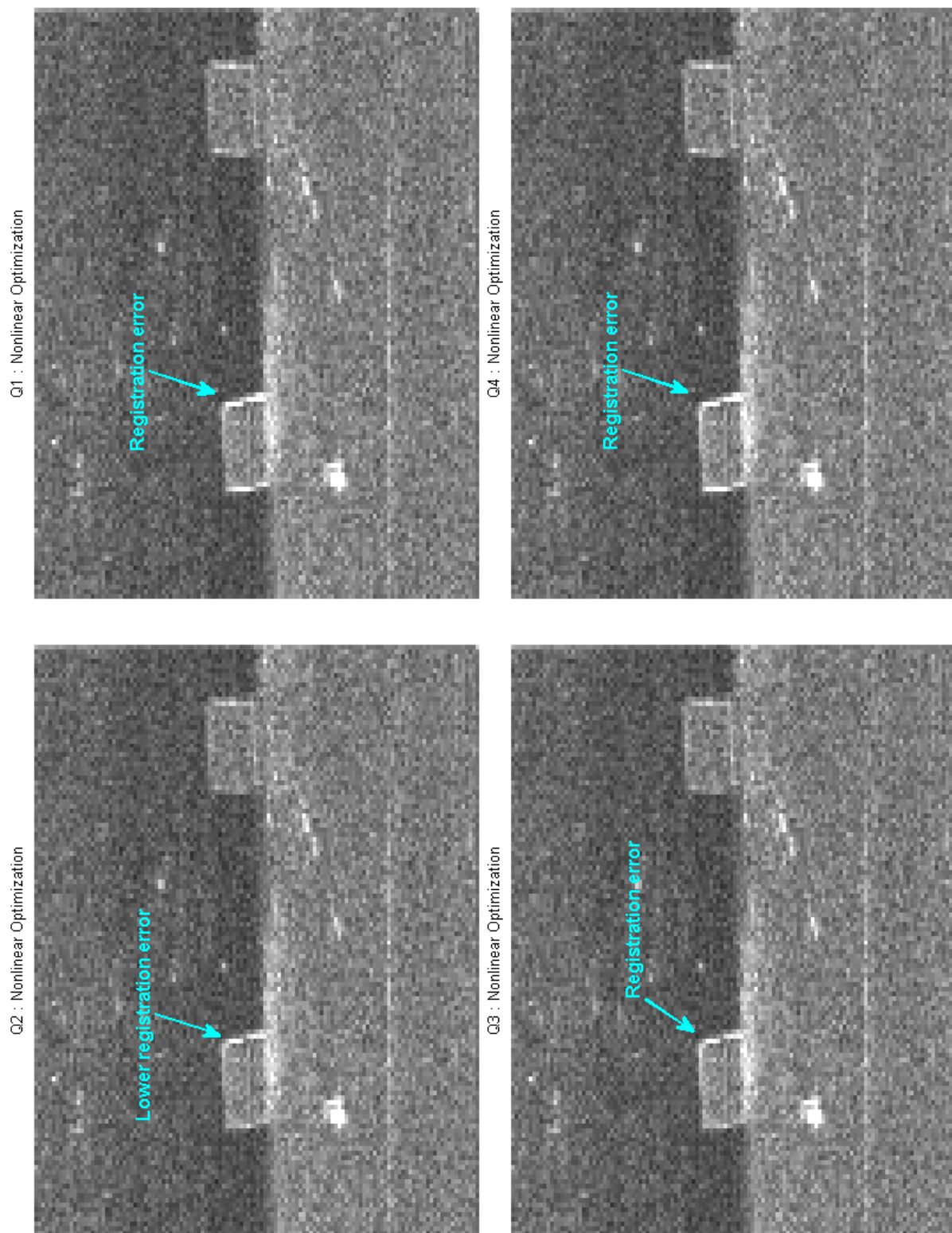
Figure 27. The four quadrant test statistics produced using the nonlinear optimized test statistic for the *tower data.*

76
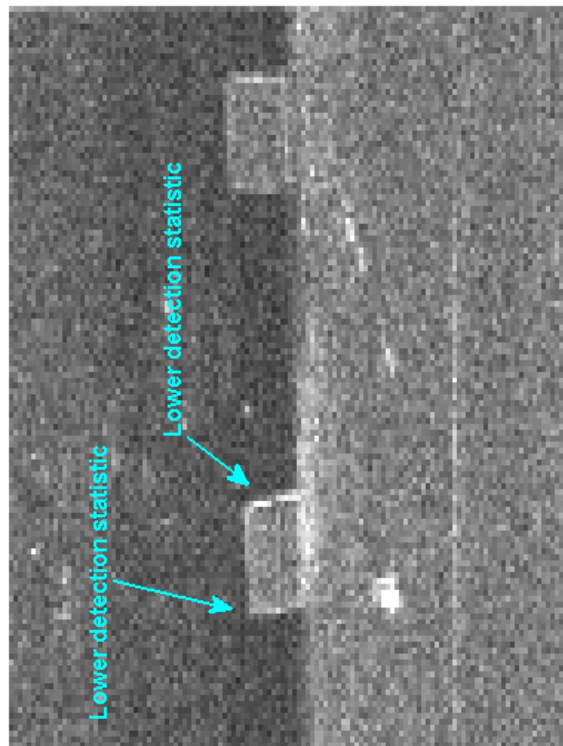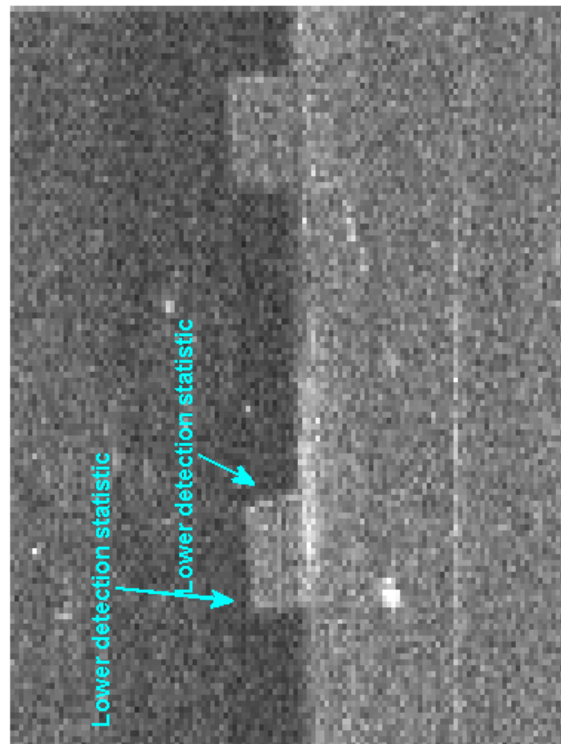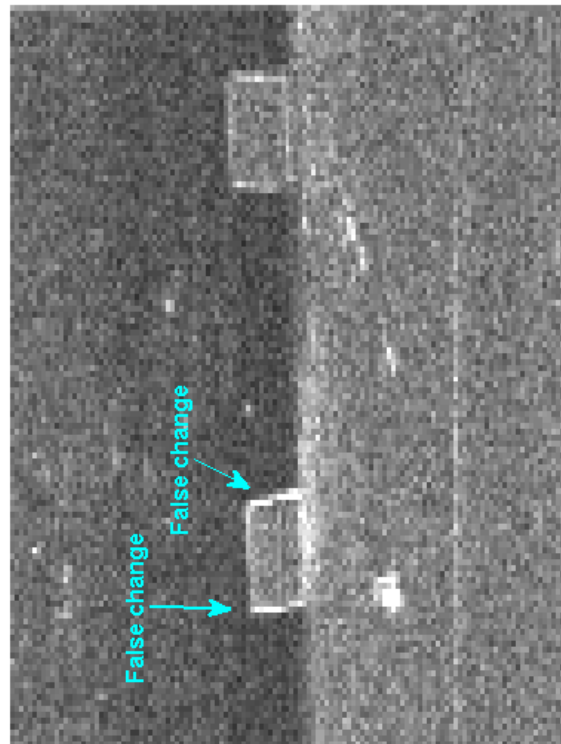
Figure 28. The uncompensated CC test statistic (bottom left), minimum nonlinear optimization test statistic (top), and the known mis-registration (bottom right) test statistic.
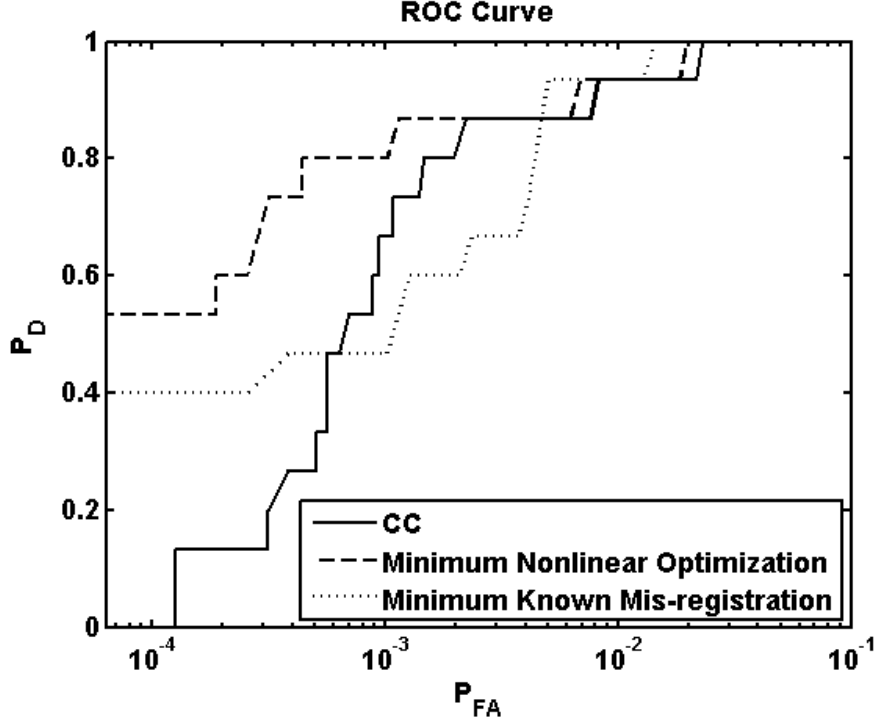
Figure 29. ROC curves for CC (solid line), proposed GLRT-based nonlinear optimization (dashed line), and the known mis-registration test statistic (dotted line).

Table 4. AUC values for the ROC curves displayed in Fig. 29.

	CC	Minimum Nonlinear Optimization	Minimum Known Mis-registration
AUC	0.9973	0.9980	0.9974

4.5.1.2 Quadratic approximation

The quadratic approximation to the quartic test statistic is compared to the nonlinear optimization approach in order to demonstrate the efficacy of that approximation. This is accomplished by investigating specific pixel classes: tree, top-edge of panel, side-edge of panel, change pixel, and grass. The figures show the percent error between the test statistic ($q(x, y; \alpha, \beta)$) from Eq. (19) and Eq. (26) prior to minimization.

78

Fig. 30 shows the different pixel classes and their spatial location in the imagery used to assess the efficacy of the approximation. The labels display the $x-$ and $y-$ coordinates, the RGB values, and the color index for each class of pixels. Fig. 31 shows the percent error between the nonlinear optimization and the quadratic approximation for Quadrant II (where the nonlinear optimization results are regarded as 'truth'). In the figures, the x-axis and y-axis are α and β respectively, while the z-axis corresponds to the percent error between test statistics in Eq. (19) and Eq. (26). Based on the simulation results, tree, change pixel, and grass pixel classes, it is seen that the minima of the quadratic approximation matches very closely to the Nelder-Mead results using the non-closed form solution. Error increases slightly for top-edge and significantly for side-edge pixels. The results demonstrate the efficacy of the quadratic approximation to replace the nonlinear optimization, yielding a more computational efficient option over the Nelder-Mead numerical optimization method. There is a 30 times improvement in computation performance of the quadratic implementation over the Nelder-Mead nonlinear optimization results.

Figure 30. The spatial location of investigated pixels from the image representing (top-to-bottom) a tree, top-edge of panel, side-edge of panel, change, and grass pixel. The labels on the image display the $x-$ and $y-$ coordinates, the RGB values, and the color index for each class of pixels.
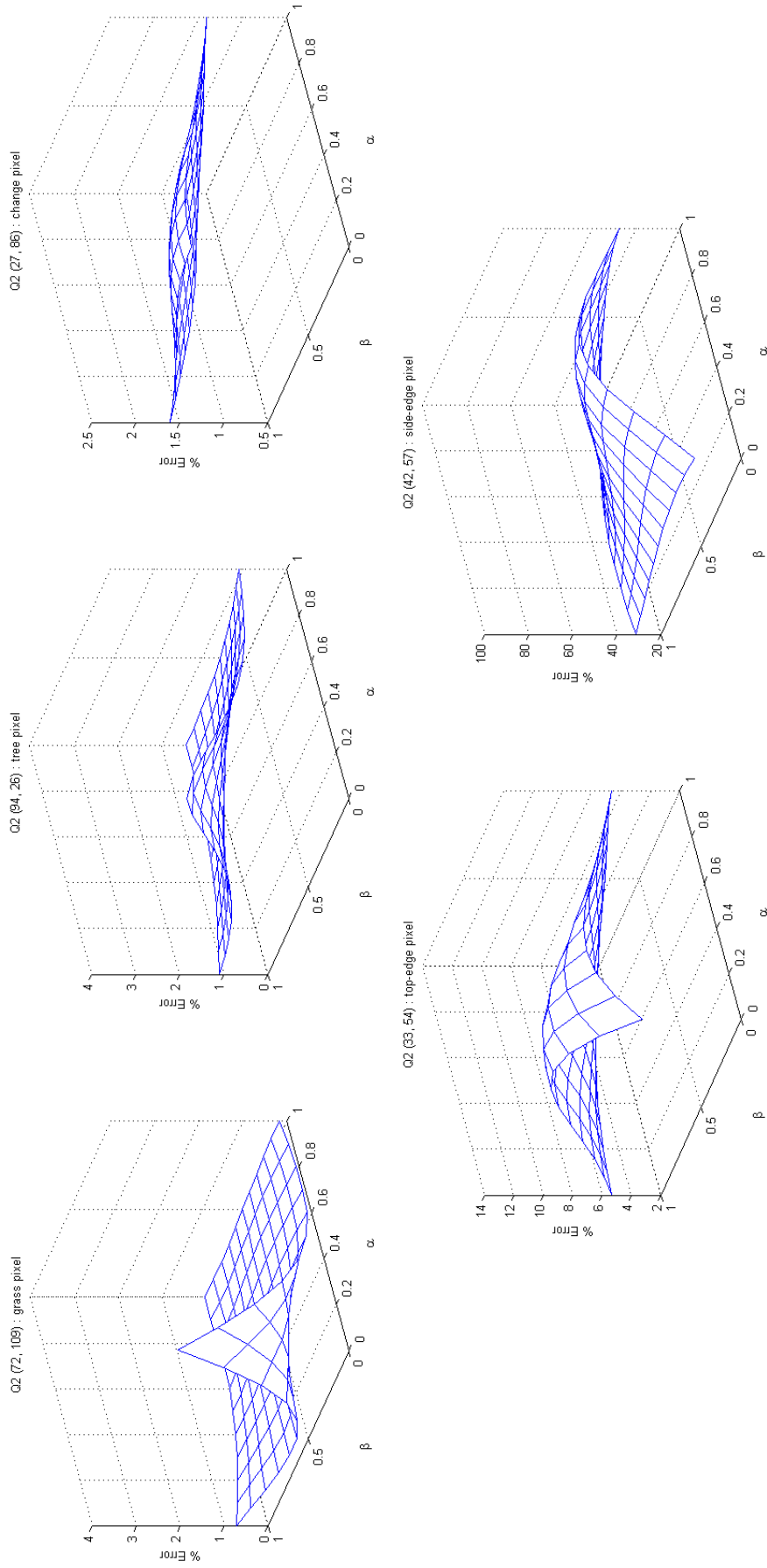
Figure 31. Percent error for five pixel classes of interest shown in Fig. 30. The error is calculated as the difference between the nonlinear optimization and the quadratic approximation relative to the nonlinear optimization test statistic for Quadrant II.

The test statistic for the four quadrants resulting from the quadratic approximation are shown in Fig. 32 for $\sigma_x = \sigma_y = 0.05$. Again, Quadrant II suppresses the mis-registration effects observed on the panel edges as seen by the lower test statistic. Fig. 33 displays the uncompensated CC result (bottom left) in comparison to the overall minimum of the quadratic approximation (top) and the known mis-registration test statistic (bottom right). The true changes in the scene are indicated with a larger (white) test statistic while a noticeable smaller (black) test statistic is observable on the panel edges while some change errors occur from the variation in shadow positions as indicated by the shot noise appearance in the test statistic imagery. The ROC results for the nonlinear optimization and quadratic approximation are nearly identical (Fig. 34). This further supports the use of the more computationally efficient closed form solution versus the nonlinear form requiring numeric approaches to solve. The AUC value results shown in Table 5 highlight the similants of the quadratic approximation results to the nonlinear optimization results. Additionally, both overcome the known mis-registration which likely does not account for mis-registration artifacts in the original data set.

Table 5. AUC values for the ROC curves displayed in Fig. 34.

	Minimum Nonlinear Optimization	Minimum Quadratic Approximation	Minimum Known Mis-registration
AUC	0.9980	0.9981	0.9974

4.5.1.3   Mis-registration estimates

While estimating sub-pixel shifts is not the goal of this work, it is instructive to examine the statistics of α and β estimates for similar groups of pixels (*e.g.*, tree, top-edge of panel, side-edge of panel, change pixel, and grass) with both the nonlinear
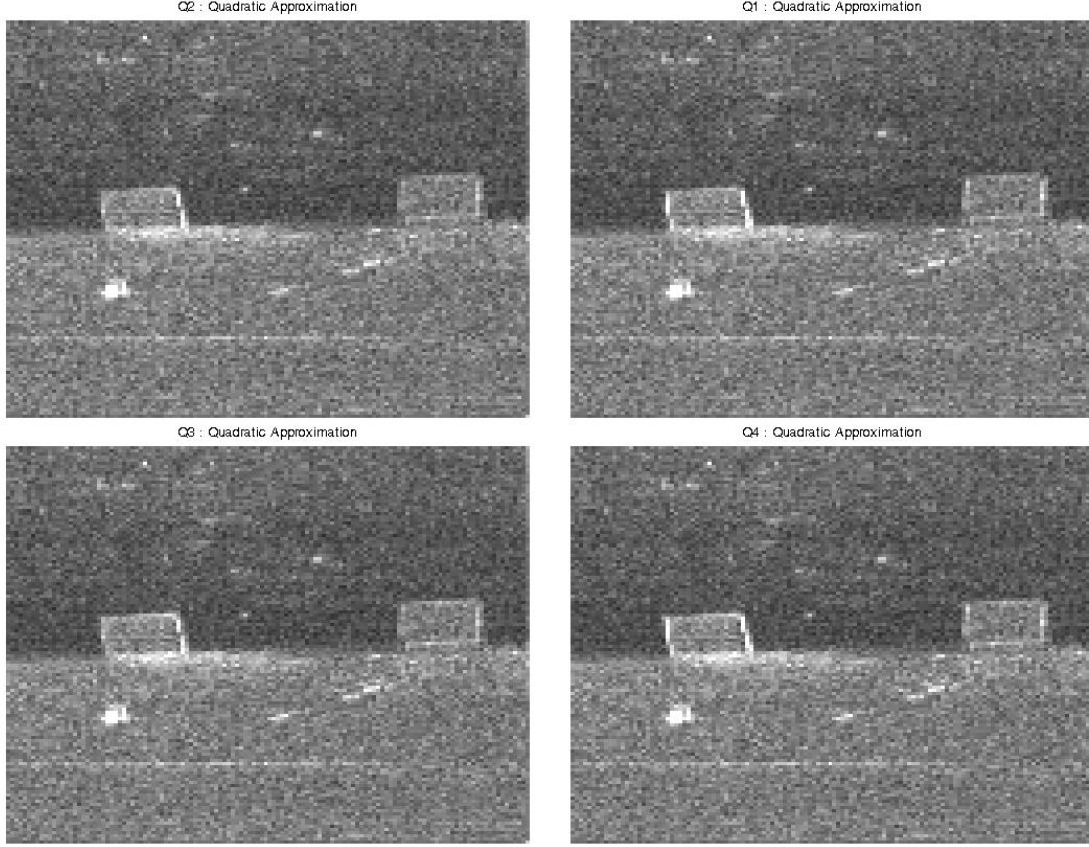
Figure 32. The four quadrant test statistics produced using the quadratic approximation.

optimization and the quadratic approximation for $\sigma_x = \sigma_y = 0.5$.

The $\bar{\beta}$ estimate for the top-edge pixel is approaching the actual value of 0.5 with moderate variance. The $\bar{\alpha}$ estimate is larger, which is expected since a shift along the edge has little effect. Based on the known mis-registration, $(\bar{\alpha}, \bar{\beta})$ should be (0.5, 0.5). Table 6 provides the mean estimates of α and β (indicated with an overbar as $\bar{\alpha}$ and $\bar{\beta}$). The $\bar{\alpha}$ estimate for the side-edge pixels is near the actual value of 0.5 with moderate variance. The $\bar{\beta}$ estimate is not close to 0.5, presumably because a vertical shift does not introduce a large change for the side-edge pixel. The minimum test statistic for the grass and tree pixels do not necessarily fall in the correct quadrant. This likely occurs because the mis-registration-induced effects are small relative to the clutter/noise level resulting from a lack of fine spatial content. Additionally, the

83
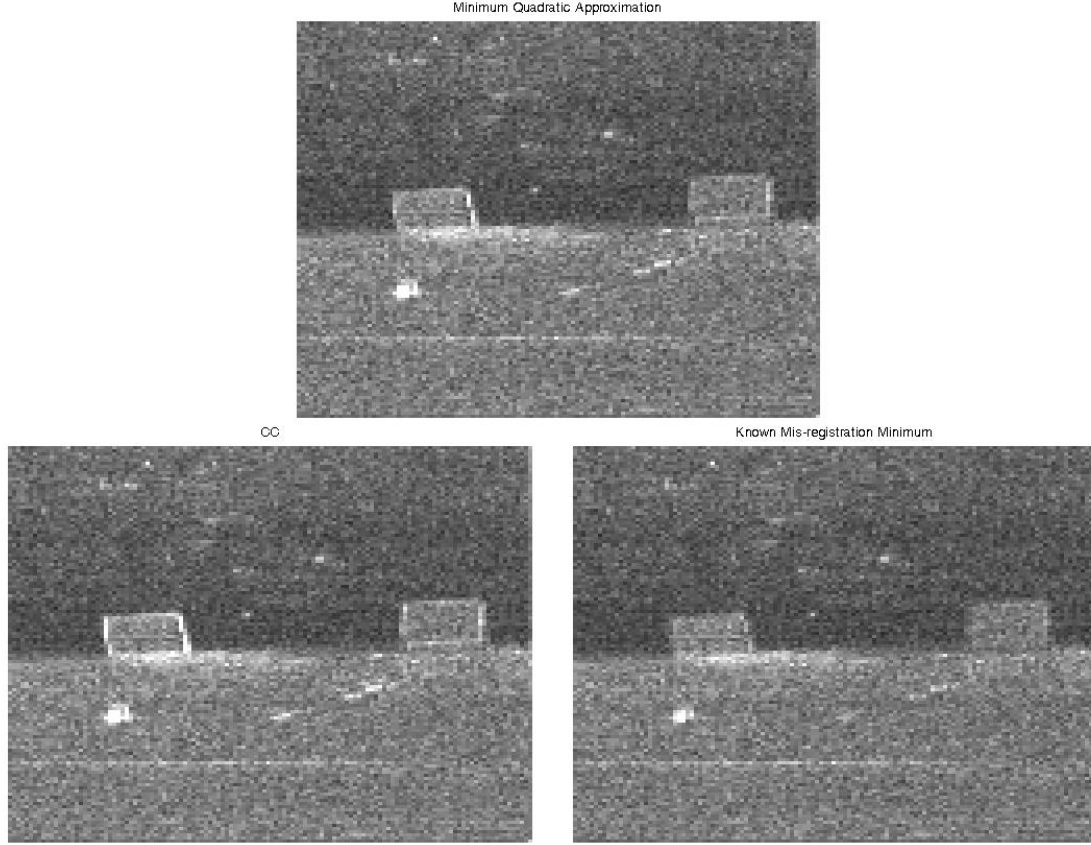
Figure 33. The uncompensated CC (bottom left), minimum quadratic approximation (top), and the known mis-registration (bottom right) test statistics visually represented.

clutter/noise level impacts the α estimate on the horizontal edge and the β estimate on the vertical edge. The local mixing model appears to weakly depend on the mis-registration. The algorithm works well with regard to reducing the test statistic for edge areas that are affected by spatial mis-registration, even if it does not provide a precise estimate of the mis-registration.

4.5.1.4 Covariance equalization predictor

The experiments are repeated using the CE predictor to assess the relative behavior with mis-registration compensation. As described in Section 2.4.2.1, CE estimates can be substituted for CC estimates. The CE and CC test statistic images are compared visually with and without compensation using the quadratic approximation

84
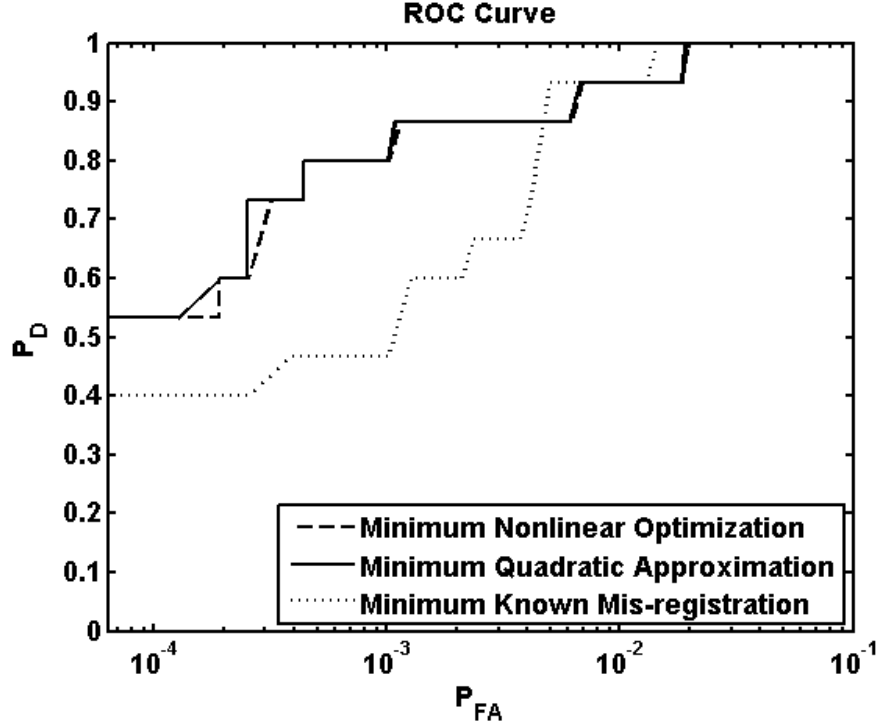
Figure 34. ROC curves for test statistics based on minimum nonlinear optimization (dashed line) and minimum quadratic approximation (dotted line).

in Fig. 35 and Fig. 36. The value of the mis-registration-induced test statistic is higher than the true change, illustrating the impact mis-registration has on the un-compensated change detectors (Fig. 35). For both algorithms, the mis-registration compensation significantly suppresses false alarms around the panel edges (Fig. 36). Comparing the corresponding ROC curves in Fig. 37, it is evident that CC provides better results than CE for this case both with and without compensation. Further-

Table 6. Mean estimates and variance of sub-pixel shifts for Quadrant II

Pixels	Nonlinear optimization				Quadratic approximation			
	$\bar{\alpha}$	σ_{α}^2	$\bar{\beta}$	σ_{β}^2	$\bar{\alpha}$	σ_{α}^2	$\bar{\beta}$	σ_{β}^2
Tree	0.233	0.145	0.174	0.034	0.303	0.056	0.142	0.055
Top-Edge	0.449	0.139	0.481	0.067	0.531	0.060	0.432	0.028
Side-Edge	0.565	0.138	0.191	0.134	0.661	0.123	0.332	0.044
Change	0.426	0.267	0.543	0.167	0.667	0.240	0.833	0.164
Grass	0.302	0.092	0.112	0.014	0.175	0.103	0.109	0.011

more, the compensation algorithm provides more significant improvement for CC than CE. The AUC values are presented in Table 7. The AUC indicates that the detection rate of the quadratic approximation is higher than the uncompensated CC or CE.
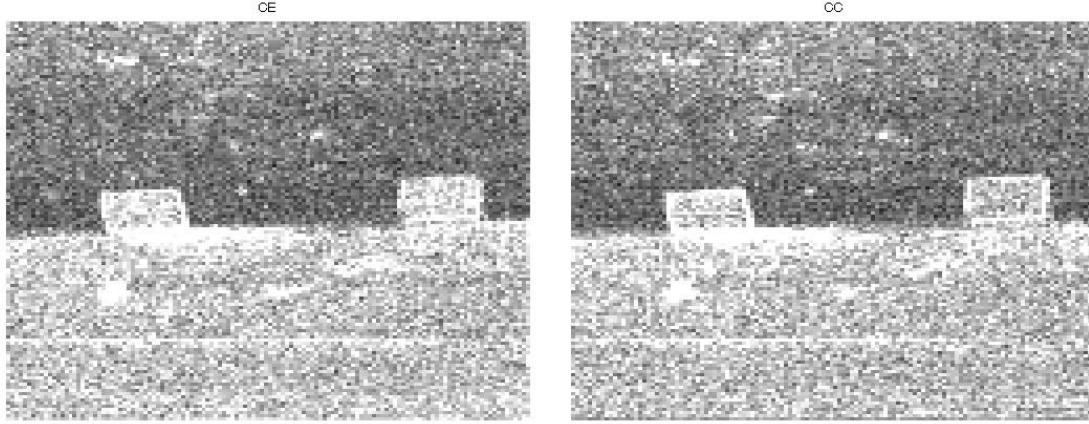
Figure 35. Visual results of the uncompensated CE change detector (left) and the CC change detector (right).
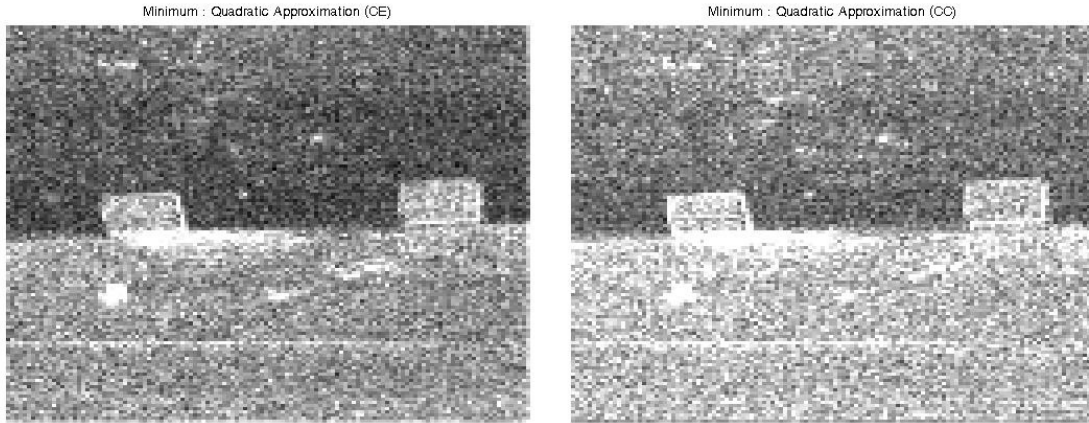
Figure 36. The minimum quadratic approximation results using the CE estimates (left) and the minimum quadratic approximation results using the CC estimates (right).
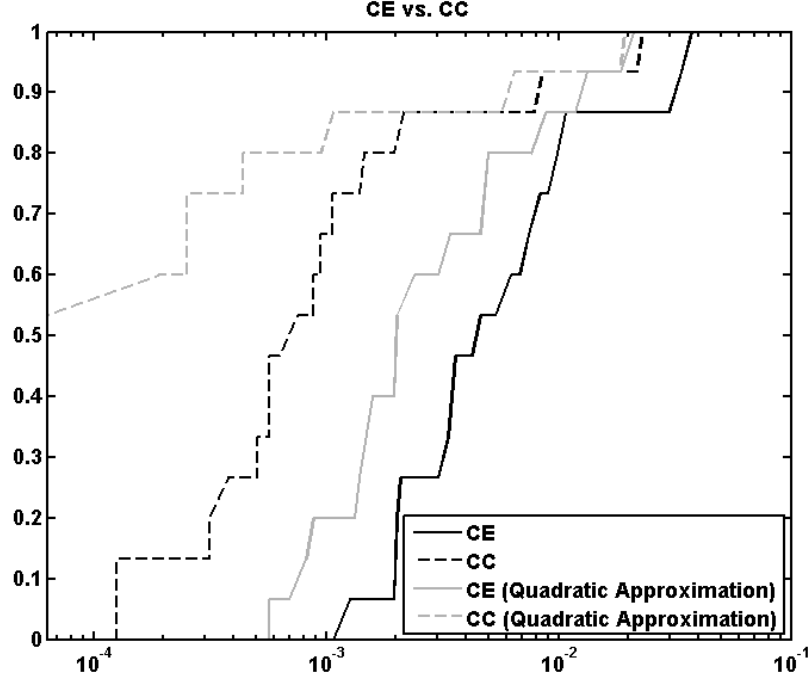
Figure 37. ROC curve for uncompensated CE change detector (black solid) and the CC change detector (black dashed) and the minimum quadratic approximation using the CE (gray solid) and CC estimates (gray dashed).

Table 7. AUC values for the ROC curves displayed in Fig. 37.

	CC	Quadratic approximation CC	CE	Quadratic approximation CE
AUC	0.9972	0.9981	0.9909	0.9954

4.5.1.5   Parameter sensitivity

The GLRT test statistic in Eq. (16) is based on three model parameters: the noise covariance matrix $\mathbf{C}_n$ and the RMS mis-registration parameters σ_x and σ_y. The value of $\mathbf{C}_n$ is estimated from the difference image while experiment-based estimates for σ_x and σ_y are required. To further explore parameter sensitivity, the RMS mis-registration parameter is varied from 0 to 1, calculating the ROC curve for each

parameter value. The baseline CC algorithm corresponds to $\sigma_x = \sigma_y = 0$. The ROC curves in Fig. 38 demonstrate the performance for the quadratic approximation algorithm (with CC prediction) using $\sigma_x = \sigma_y = \{0.0, 0.05, 0.1, 0.5\}$. The best results are achieved with σ_x and σ_y on the order of 0.05 to 0.1. This result indicates both the importance of including the prior distribution for the residual mis-registration and the challenge of appropriately setting the parameter. Having no prior distribution would correspond to large σ_x and σ_y, which would tend to poor performance as indicated in $\sigma_x = \sigma_y = 0$ (CC results) in Fig. 38. In the next section, the influence of parameter sensitivity of the image data characteristics and the target mask employed in the scoring is explored.
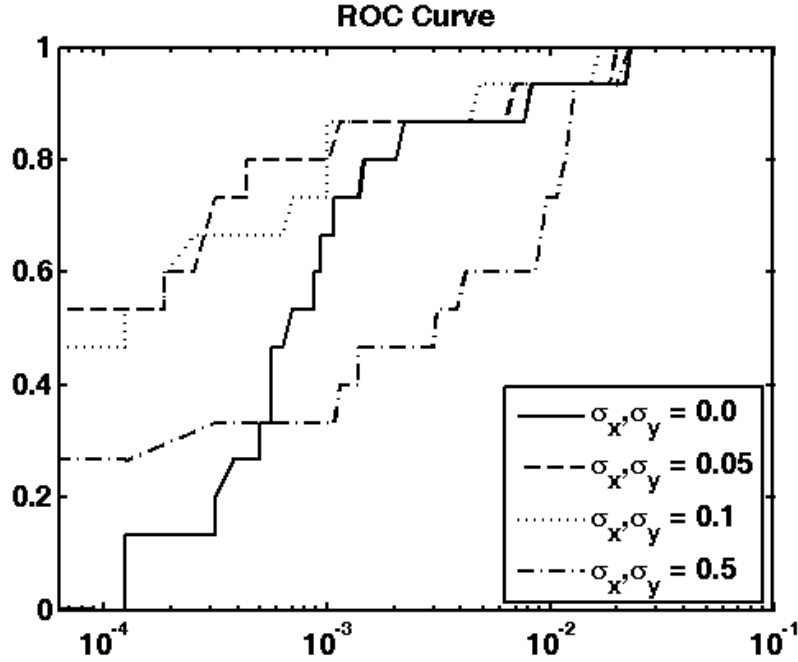
Figure 38. The ROC curve compares the performance using the quadratic approximation for the *tower data* with varied RMS mis-registration parameters (σ_x and σ_y) where CC ($\sigma_x = \sigma_y = 0$) is the solid line, $\sigma_x = \sigma_y = 0.05$ is the dashed line, $\sigma_x = \sigma_y = 0.1$ is the dotted line, and $\sigma_x = \sigma_y = 0.5$ is the dash-dot line.

4.5.1.6   Extended performance investigation

In this section the *Mojave data* set is explored to provide additional insight on the performance of the proposed mis-registration GLRT-based algorithm. The results are examined against various truth masks to demonstrate the performance impact of edge pixels. Detection results in the form of ROC curves and AUC are used to show the performance of the proposed mis-registration GLRT-based algorithm against LCRA. Upsampling is a pre-processing requirement for sub-pixel LCRA. In order to provide a fair comparison between LCRA and the GLRT-based approach, images are upsampled by two in both the x and y direction prior to running the CD routine.

The proposed mis-registration GLRT-based algorithm and LCRA algorithm are demonstrated on both the *tower data* and *Mojave data* sets for comparison purposes. Multiple GLRT curves are generated by varying the size of the truth pixel mask while fixing the mis-registration parameter $\sigma_x = \sigma_y = 0.5$.

Fig. 40 shows ROC curves corresponding with an increasing erode of the truth mask for the *tower data* set. The ROC curves include CC, $\sigma_x = \sigma_y = 0.1$, $\sigma_x = \sigma_y = 0.5$, and LCRA. There is one true change in the *tower data* set and the ground truth mask provides the spatial pixel locations to develop the ROC curve for every threshold. The ground truth is defined at the pixel-level where the truth mask is derived using the CC test statistic. The target truth mask is 4x4 resulting in 16 target pixels. A 3 pixel ignore mask extends the true target mask for a total size of 20x20 pixels. As such, 20x20 is the maximum extent of the truth plus ignore pixel region. The masks vary based on the number of pixels associated with the target centroid. The target centroid begins with a 4x4 true change pixel mask and erodes outward by 1 pixel in the $x-$ and $y-$ direction toward the ignore mask edge per ROC curve evaluation iteration. Thereby, the background pixels remain unchanged at 66,632 pixels. The sizes of the target centroid pixels for each ROC curve is 4x4,

6x6, 8x8, 10x10, and 12x12 (a pixel diagram is shown in Fig. 39 for reference). Thus, the ignore mask continues to shrink as the true target centroid expands. The ignore mask begins with an 8 pixel boundary outward from the 4x4 target pixels and shrinks by 1 pixel until it reaches the 12x12 target with a 4 ignore pixel boundary. The ROC curves intersect thus the AUC is considered and shown in Table 8. Although, the LCRA tends to have a higher AUC value for this data, it must be noted that the AUC gives equal weight to the full range of threshold values obscuring the fact that the proposed GLRT-based algorithm performs better for lower false alarm values specifically those truth masks that extend into the target mask to reduce effects of uncertain edge pixels.
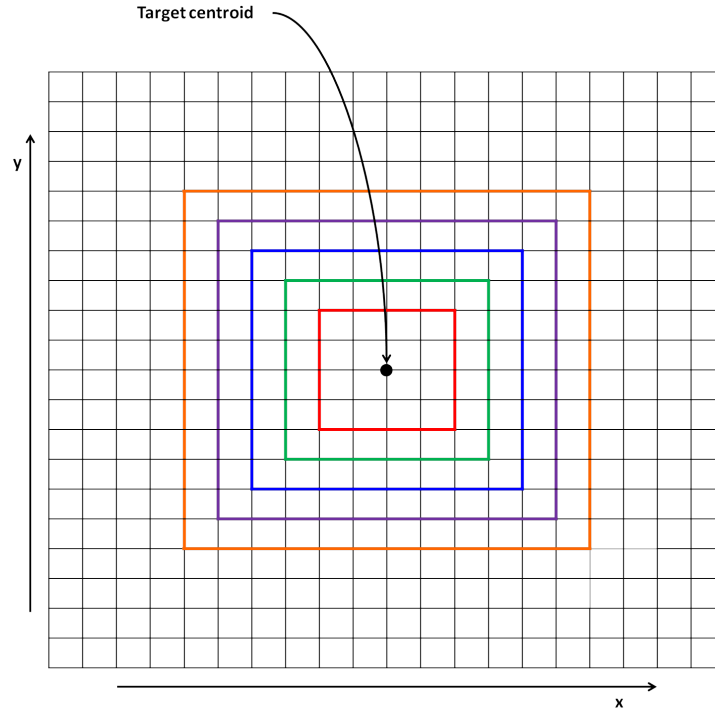
Figure 39. The diagram shows the target centroid surrounded by a pixel ignore mask. As the ROC performances are evaluated at each performance iteration the truth target size increases toward the edge of the ignore mask. The truth mask sizes of the target centroid pixels for each ROC curve is 4x4 (red square), 6x6 (green square), 8x8 (blue square), 10x10 (purple square), and 12x12 (orange square) for the *tower data* set.

Table 8. AUC values for the ROC curves displayed in Fig. 40 (*tower data*).

	CC	Quadratic approximation $\sigma_x = \sigma_y = 0.1$	Quadratic approximation $\sigma_x = \sigma_y = 0.5$	LCRA
AUC 1	0.99864	0.99939	0.99959	0.99956
AUC 2	0.99875	0.99949	0.99955	0.99974
AUC 3	0.99871	0.99945	0.99841	0.99964
AUC 4	0.99656	0.99607	0.98460	0.99818
AUC 5	0.98135	0.97968	0.96089	0.99137

Fig. 41 displays the ROC curves for the *Mojave data* set. Similar to the *tower data*, the ROC curves for CC, $\sigma_x = \sigma_y = 0.1$, $\sigma_x = \sigma_y = 0.5$, and LCRA were calculated for varying truth masks. The *Mojave data* contains two change targets and were again derived using the CC test statistic. An ignore mask for both targets extended 3 pixels past the observed true target for a total size of 24x24 pixels. Both target truth masks varied at the same rate per evaluation. The target pixels begin with a 2x2 square true change region before expanding outward toward the edge of the ignore mask. The background pixels account for a total of 196,860 pixels. The sizes of the target centroid pixels for each ROC curve calculation, starting with the upper left plot of Fig. 41, is 2x2, 6x6, 10x10, 14x14, and 18x18. The ignore mask starts with an 11 pixel boundary and reduces to a 3 pixel boundary for the final ROC curve. The AUC values for the curves in Fig. 41 are provided in Table 9.

Table 9. AUC values for the ROC curves displayed in Fig. 41 (*Mojave data*).

	CC	Quadratic approximation $\sigma_x = \sigma_y = 0.1$	Quadratic approximation $\sigma_x = \sigma_y = 0.5$	LCRA
AUC 1	0.99256	0.99666	0.99800	0.99793
AUC 2	0.99240	0.99679	0.99816	0.99824
AUC 3	0.99307	0.99735	0.99862	0.99863
AUC 4	0.99362	0.99789	0.99916	0.99913
AUC 5	0.99279	0.99512	0.97564	0.95889

After observing the (σ_x, σ_y) parameter sensitivity with the varying truth analysis, the change detection performance is found to vary somewhat based on user-defined parameters for the underlying prior probability distribution for the residual misregistration. While this supports the importance of including a prior distribution in the model, it motivates further work to better understand this parameter sensitivity. This specific experiment demonstrates that the algorithmic performance is largely based on coverage of the truth mask. The conclusion of which algorithm has superior performance can change depending on the truth mask used in the analysis. For the middle truth mask, the proposed mis-registration GLRT-based approach and LCRA are comparable.
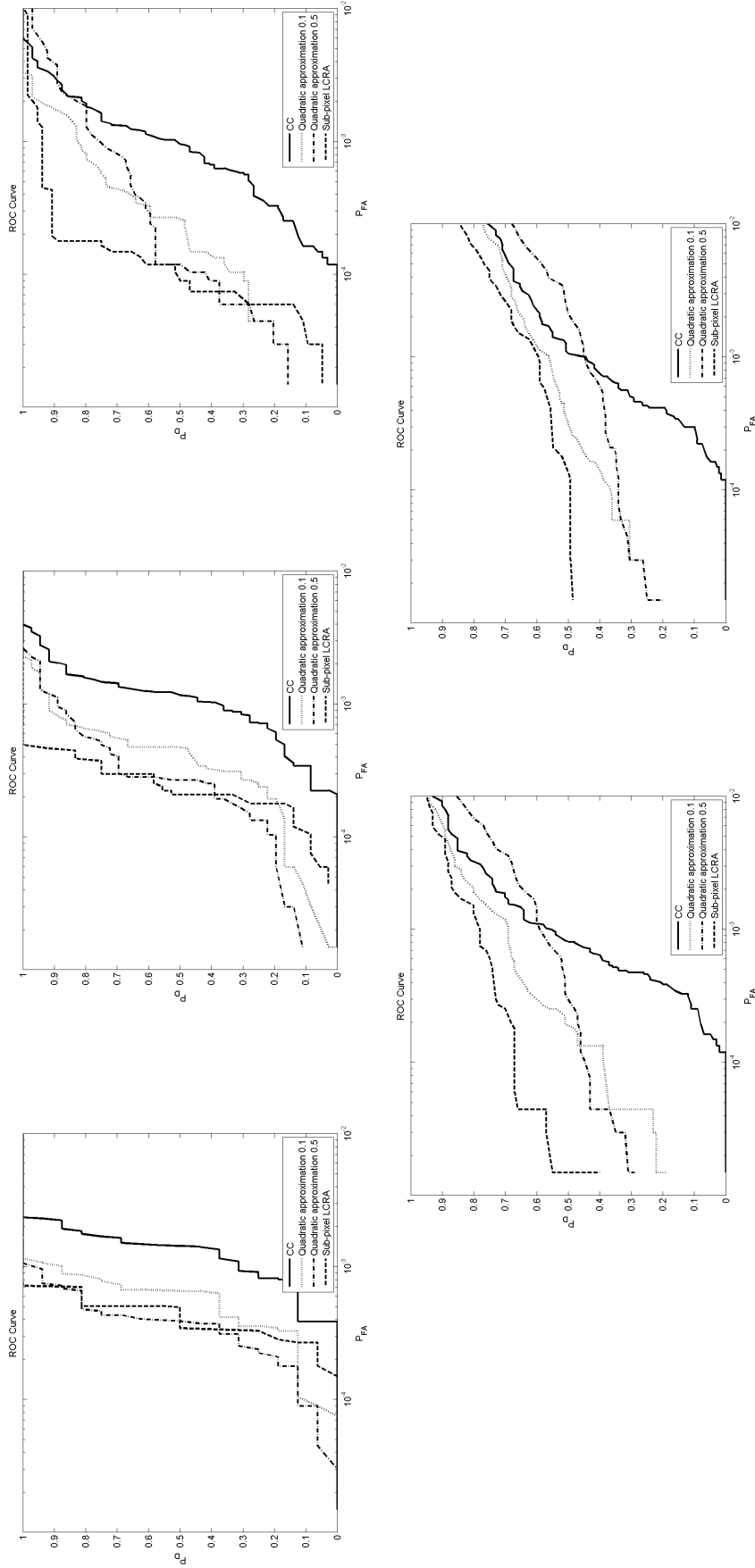
Figure 40. The *tower data* ROC curves with varying truth masks. The truth mask begin with a 4x4 change pixel area dilating outward until toward the **3 pixel non-penalizing** border. The curves represent CC (solid line), $\sigma_x = \sigma_y = 0.1$ mis-registration compensation GLRT (dotted line), $\sigma_x = \sigma_y = 0.5$ mis-registration compensation GLRT (dash-dot line), and the LCRA (dashed line).
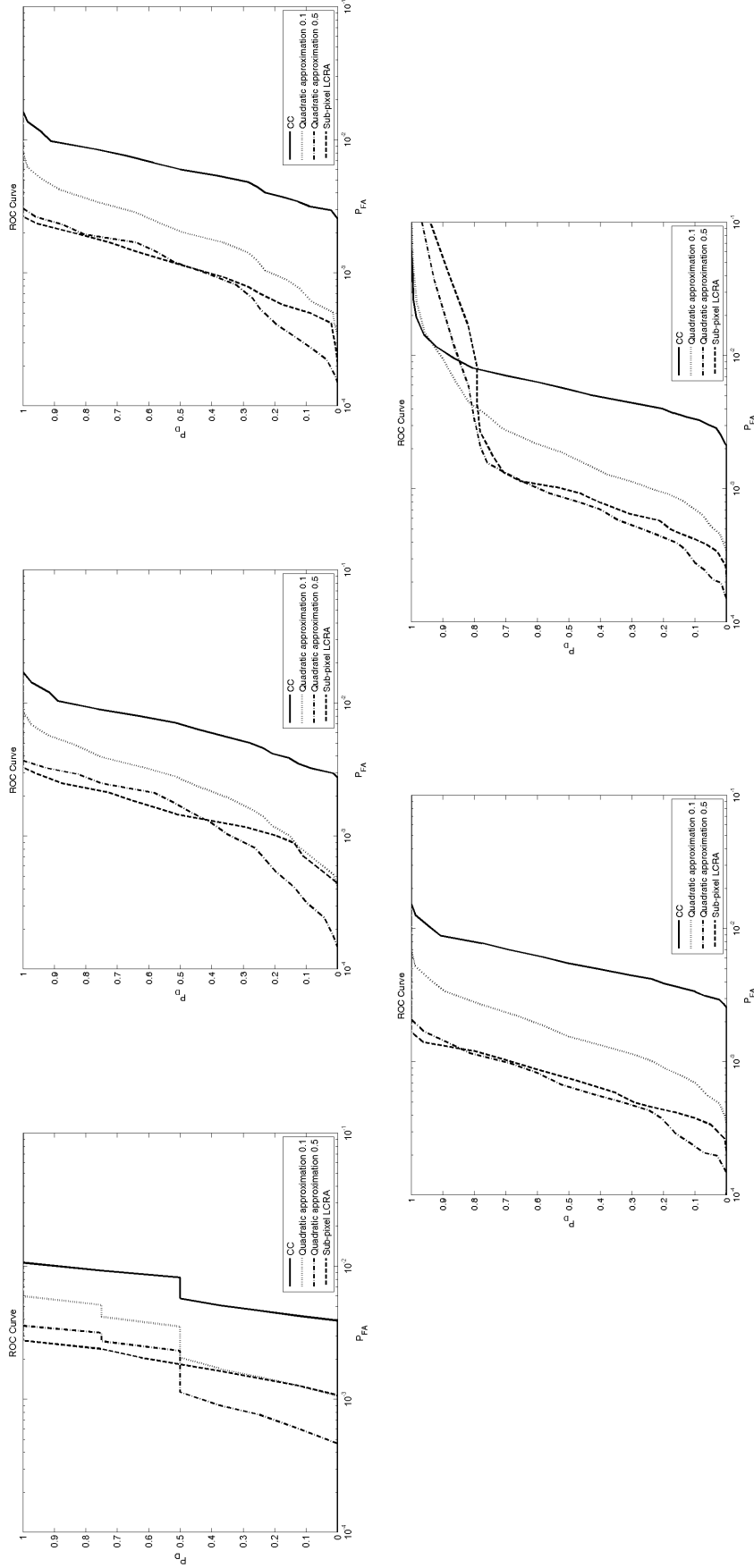
Figure 41. *Mojave data* set with the synthetic change displaying the ROC curves for various eroding truth masks. Beginning with a **2x2** change pixel area dilating outward toward the **3** pixel border. The curves represent CC (solid line), $\sigma_x = \sigma_y = 0.1$ mis-registration compensation GLRT (dotted line), $\sigma_x = \sigma_y = 0.5$ mis-registration compensation GLRT (dash-dot line), and LCRA (dashed line).

The (σ_x, σ_y) parameter tuning results for the propsed GLRT-based algorithm on the interpolated data justify further exploration of the parameter and its impact on performance. The RMS mis-registration parameter is varied from 0 to 1 for the *Mojave data* set, calculating the ROC curve for each parameter value. The truth mask in Fig. 42 (left) contains one change target as defined at the pixel-level and derived using the CC test statistic. There is a border surrounding the truth target that is ignored during evaluation to eliminate uncertainty along the target edges. The white target pixels are a 6x6 square consisting of 36 pixels and the boundry pixels radiate outward 7 pixels in each direction creating a border of 364 pixels (or a 20x20 square region excluding the target pixels). The total number of background pixels is 66,632. The baseline CC algorithm corresponds to $\sigma_x = \sigma_y = 0$. The ROC curves in Fig. 42 (right) demonstrate the performance for the quadratic approximation algorithm (with CC prediction) using $\sigma_x = \sigma_y = \{0.0, 0.05, 0.1, 0.5\}$ on the *tower data*. The best results on the upsampled imagery are achieved with σ_x and σ_y are on the order of 0.5 and 0.1. In the non upsampled domain, the results correspond to 0.25 and 0.05 respectively. The results are consistent with results presented in Section 4.5.1.5, even though the truth mask may be somewhat different. The variation in results is due to a difference in edge pixels between the upsampled and original imagery.

In addition, the *Mojave data* set was used to explore the variation of performance with the mis-registration parameters. The truth mask in Fig. 43 (left) contains two change targets, both have ignore pixels surrounding the target edges. The left and right changes include an 8x8 target square (64 pixels) with 8 ignore boundry pixels (24x24=576 square region excluding the target pixels). The total number of background pixels is 196,860. The ROC curves are generated by varying the (σ_x, σ_y) parameter and are shown in Fig. 43 (right). The best results are achieved with the upsampled *Mojave data* set are on the order of 0.25 and 0.05 in the original non

upsampled space (Section 4.5.1.5). The conclusion is the best performing parameter range is consistent through repeated results on different imagery and varying truth masks.
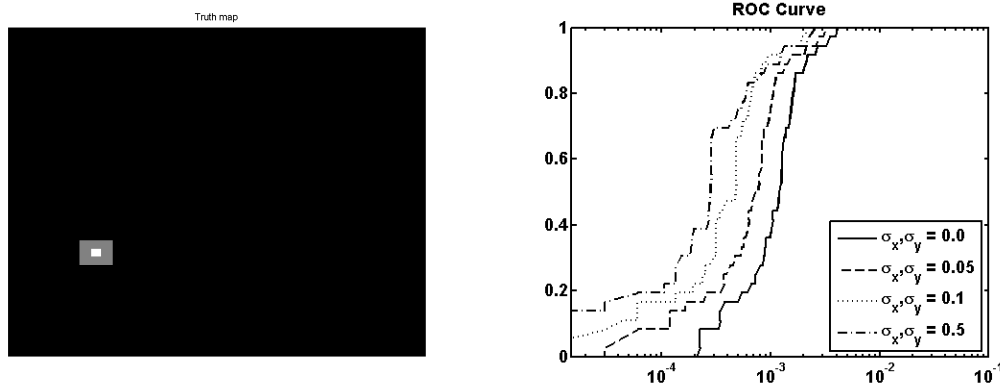
Figure 42. Parameter investigation for (σ_x, σ_y) with the *tower data*. The truth mask (left) displays target pixels in white and boundry pixels in gray which are ignored during evaluation. The ROC curve (right) compares the performance using the quadratic approximation with varied RMS mis-registration parameters (σ_x, σ_y) where CC ($\sigma_x = \sigma_y = 0$) is the solid line, $\sigma_x = \sigma_y = 0.05$ is the dashed line, $\sigma_x = \sigma_y = 0.1$ is the dotted line, and $\sigma_x = \sigma_y = 0.5$ is the dash-dot line.

4.5.2 Parallax-compensation algorithm

This section discusses the results for the parallax compensation algorithm derived in Section 3.2. The primary experimental results are promising by visual inspection as any potential quantitative assessment would be difficult to derive with lack of truth data. For the synthetic DIRSIG data set, the assessment is performed visually and good change detection is obtained while minimizing parallax errors.

4.5.2.1 Synthetic DIRSIG data

This section shows that the correspondence matching pixel shift estimate from Section 3.2 provides a good approximation of the parallax direction (denoted here as the computed parallax direction). The results for the manually estimated parallax

96
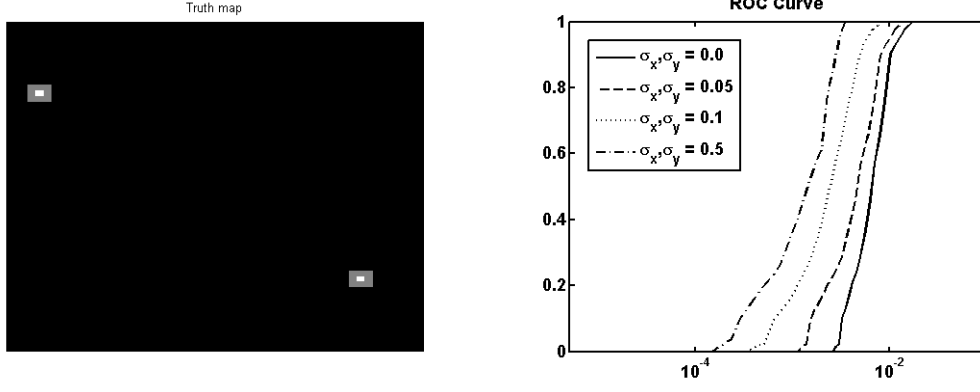
Figure 43. Parameter investigation for (σ_x, σ_y) with the *Mojave data*. The truth mask (right) displays target pixels in white and boundry pixels in gray which are ignored during evaluation. The ROC curve (left) compares the performance using the quadratic approximation with varied RMS mis-registration parameters (σ_x, σ_y) where CC ($\sigma_x = \sigma_y = 0$) is the solid line, $\sigma_x = \sigma_y = 0.05$ is the dashed line, $\sigma_x = \sigma_y = 0.1$ is the dotted line, and $\sigma_x = \sigma_y = 0.5$ is the dash-dot line.

direction (90° as computed directly from the imagery) are shown visually in Fig. 44. The parallax error parameter (σ_p) is varied while the mis-registration parameter is held constant ($\sigma_m = 0.5$) while searching over $(\tilde{m}, \tilde{n}) = (-1, \{-8, -7...7, 8\})$ and $(\tilde{m}, \tilde{n}) = (0, \{-8, -7...7, 8\})$ regions of whole pixel shifts (double in extent in the $\tilde{n}$ direction relative to the known maximum parallax shift). The first entry in Fig. 44 is the baseline CC and the visual result for increasing σ_p follow. According to Fig. 44, as σ_p progresses from low (too severe a penalty function) to high (too lax a penalty function), best performance occurs at $\sigma_p = 4.0$ pixels (approximately the true parallax).

Fig. 45 shows the per pixel mapping of the minimum value of $q(\cdot)$ in Eq. (41) resulting from the $(\tilde{m}, \tilde{n})$ search window between a fixed pixel in the reference image to the search area in the test image for a fixed value of σ_p. For the ground plane where no parallax exists, values of $(\tilde{m}, \tilde{n})$ should be approximately $(0, 0)$. This observation is shown in the visual $(\tilde{m}, \tilde{n})$ maps as the ground plane values are represented by $\tilde{n} = 0$. For buildings that exhibit parallax, values of $(\tilde{m}, \tilde{n})$ should approximate the

parallax shift (in pixels) along edges in the parallax direction. The $\tilde{n}$ values should correspond roughly to the truth map shown in Fig. 23. The value of σ_p stabilizes at approximately $\sigma_p = 4$ as shown in the $(\tilde{m}, \tilde{n})$ mapping plots where the building edges take on a vertical value shift of $\tilde{n}$ according to the truth map.

Fig. 46 displays the results using the computed parallax direction attained by Eq. (46) versus the manually estimated parallax direction. The computed parallax angle is $\phi = 86.6°$ which is very close to the manually estimated parallax direction of 90°. The minimum selection map (Fig. 47) is now well-structured and the $\tilde{n} = -4$ pixels on the building edges are easily identified. Results between the manually estimated ϕ and the computed value ϕ show significant differences in structure. This indicates some sensitivity in the value of ϕ during the optimization. The difference between the manual estimate and the computed are likely due to a slight sub-pixel parallax shift attained during the registration process of the temporal images. The results show there is little sensitivity to the parallax parameter (σ_p) and for values of σ_p greater than the manually estimated parallax direction, there is no penalty paid.
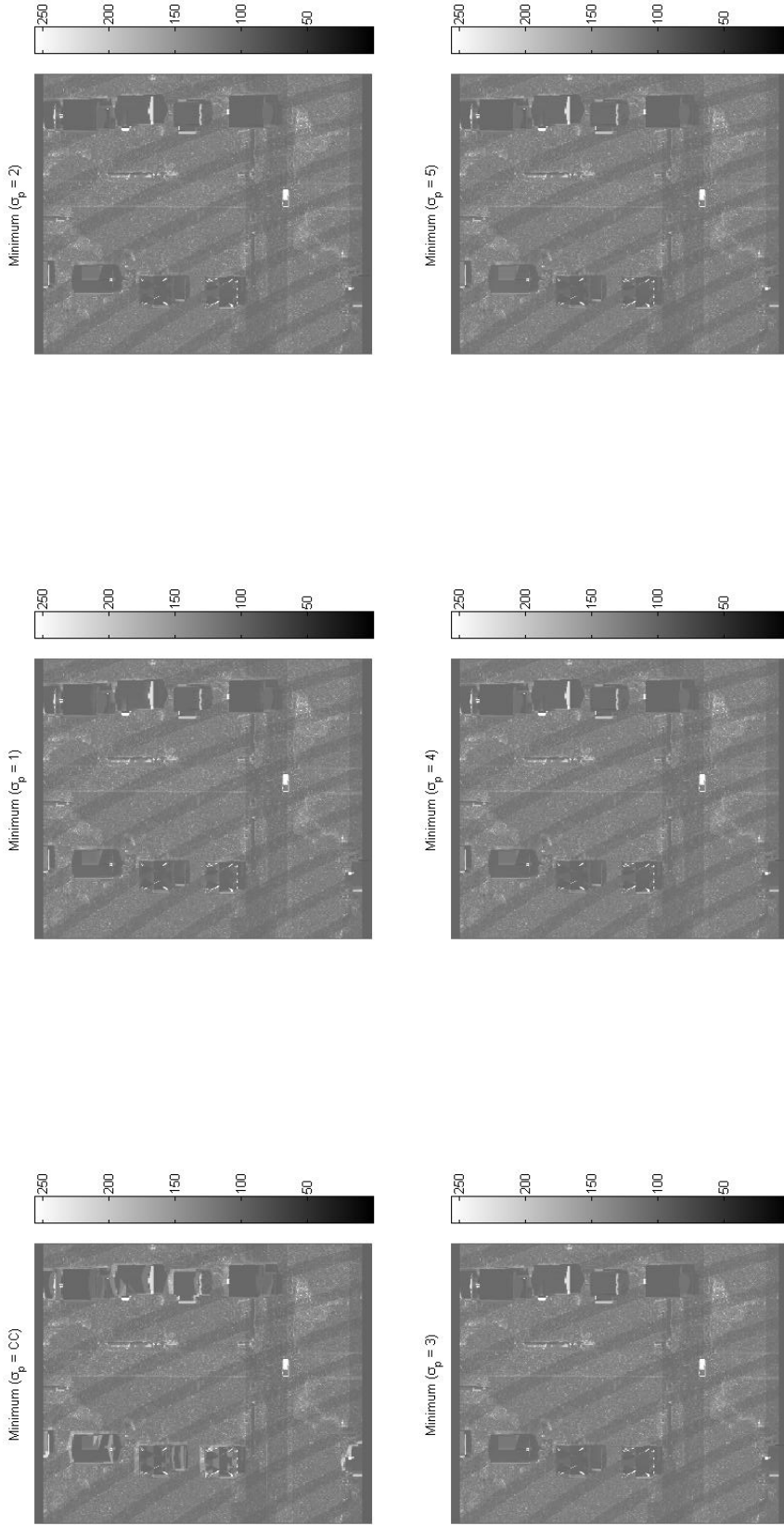
Figure 44. Each entry shows the results for the specified value for σ_p using the synthetic DIRSIG data. The first (upper left) test statistic image is the baseline CC. The sequential test statistic images derived from the parallax compensation algorithm minimum are a result from increasing σ_p (left to right, top to bottom). These results are developed with a constant $\phi = 90°$ parallax direction angle in the cost function described in Eq. (19).
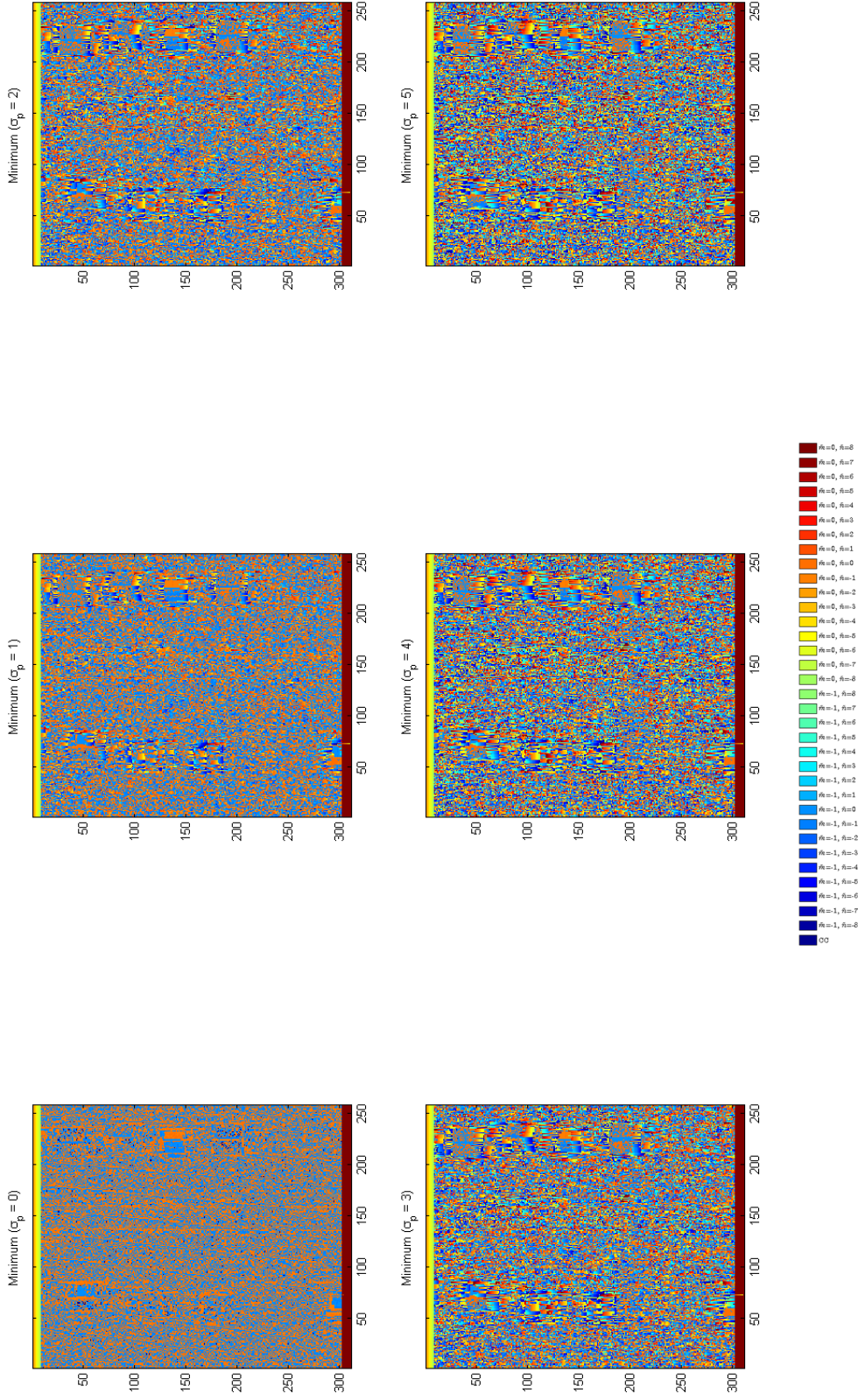
Figure 45. Each map for the DIRSIG data set shows the associated $(\tilde{m}, \tilde{n})$ chosen as the minimum for the specified σ_p value.
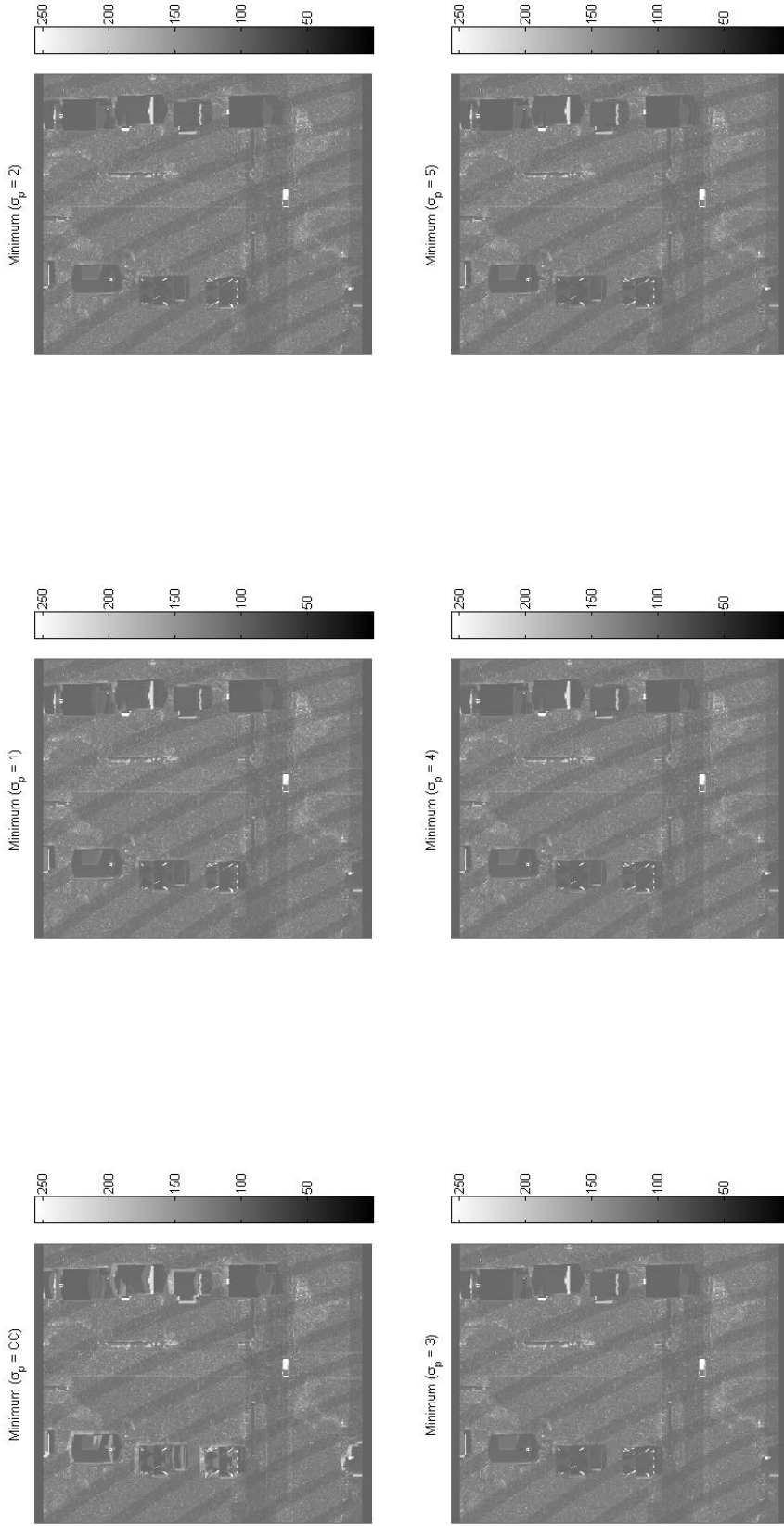
Figure 46. Each entry shows the results for the specified σ_p value using the DIRSIG data set. The first (upper left) test statistic image is the baseline CC. The sequential test statistic images derived from the parallax compensation algorithm minimum are resulted from increasing σ_p. These are developed by calculating the parallax direction angle, $\phi = 86.6°$, using a stereo correspondence algorithm.
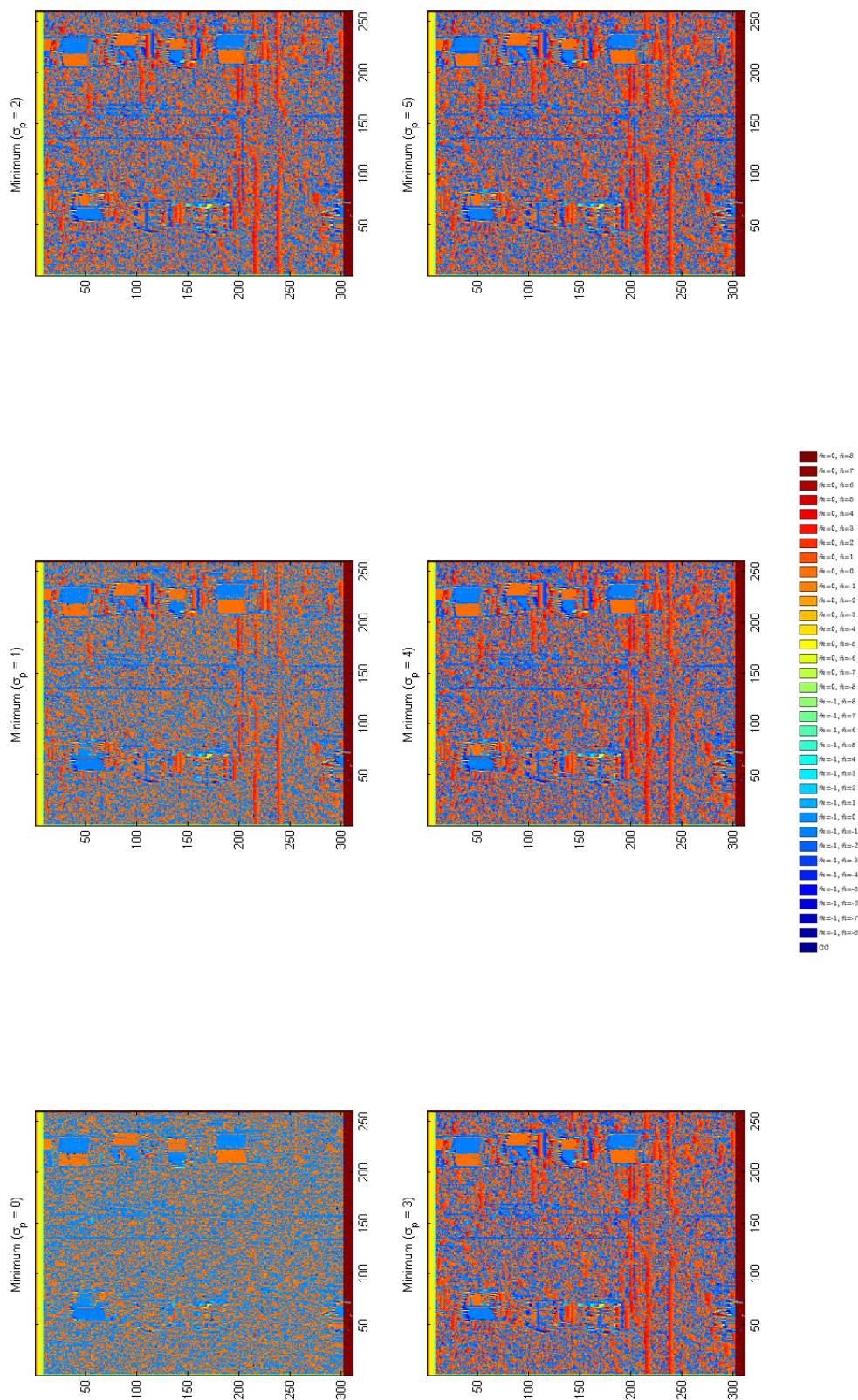
Figure 47. Each map using the DIRSIG data set shows the associated $(\tilde{m}, \tilde{n})$ chosen as the minimum for the specified σ_p value. The maps become well-structured and the $\tilde{n} = -4$ pixels on the building edges are easily identified. The results show there is little sensitivity to the parallax parameter, σ_p and at a σ_p greater than the parallax, there is no penalty paid for improvement.

The calculated synthetic ground truth mask described in Section 4.2.2.1 provides further insight into the performance of the algorithm. The truth parallax class pixels mean and variance were calculated as 1.9124 and 0.7228, respectively, as defined in the truth mask in Fig. 23. The computed parallax direction maps computed via the correspondence algorithm shown in Fig. 47 were limited to $\tilde{n}$ as the parallax shift is vertical in order to compare the parallax shift in pixels to the truth parallax shift. The visual results are displayed in Fig. 48. The first image corresponds to the calculated parallax truth based on the heights of the buildings. The middle of the buildings are then catergorized as ignore pixels unless the pixels are along the edges signifying parallax pixels. The subsequent images are the visual results cooresponding to the $\tilde{n}$ shift as selected by the proposed parallax-compensation algorithm as σ_p is increased.
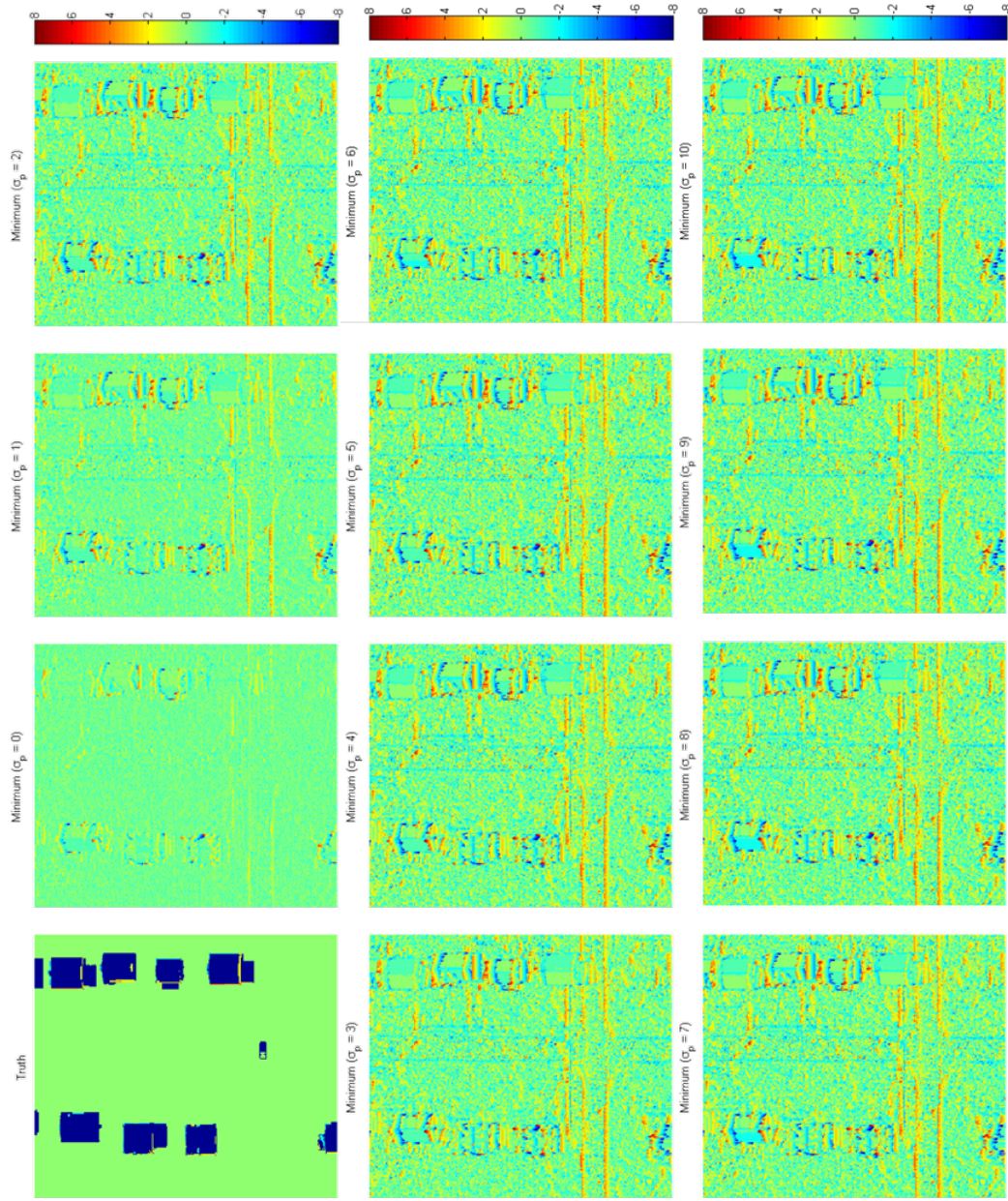
Figure 48. The first image corresponds to the calculated parallax truth based on the heights of the buildings. The middle of the buildings are then catergorized as ignore pixels unless the edges signifying parallax pixels. The subsequential images are the results cooresponding to the $\tilde{n}$ shift as selected by the proposed parallax-compensation algorithm as σ_p is increased.

Table 10 tabulates the mean and variance for each σ_p ranging from zero to one (for $\sigma_m = 0.5$) for the ground plane pixels and the parallax pixel results in the minimum selection map (Fig. 48). Accordingly, the ground plane pixel statistics are close to zero which is anticipated but as σ_p increases so does the error. The parallax mean statistics get closer to the actual known value as σ_p increases. The variance of the parallax pixels also increases which increases the uncertainty of the mean estimates. In addition, the ground plane mean and variance diverge from the calculated value becoming less accurate while σ_p increases beyond the true parallax shift. Both cases result in the increased clutter appearance in Fig. 48. The impact is that true change pixels could be lost as σ_p grows too large.

Table 10. Statistics of the detection statistic $q(\cdot)$ for the parallax and ground plane pixels.

σ_p	$\mu_{q(\cdot)}$		$\sigma^2_{q(\cdot)}$	
0	ground	0.504565	ground	0.292905
	parallax	0.880782	parallax	0.704813
1	ground	0.753677	ground	0.555484
	parallax	1.405863	parallax	1.276498
2	ground	1.043424	ground	0.81114
	parallax	1.629967	parallax	1.510966
3	ground	1.155527	ground	0.888017
	parallax	1.686645	parallax	1.555591
4	ground	1.203219	ground	0.917929
	parallax	1.715961	parallax	1.593324
5	ground	1.227652	ground	0.935127
	parallax	1.725081	parallax	1.598425
6	ground	1.242345	ground	0.944134
	parallax	1.72899	parallax	1.601864
7	ground	1.251017	ground	0.949046
	parallax	1.731596	parallax	1.601967
8	ground	1.256184	ground	0.951562
	parallax	1.736156	parallax	1.607655
9	ground	1.259919	ground	0.953887
	parallax	1.738111	parallax	1.614551
10	ground	1.262952	ground	0.954663
	parallax	1.741368	parallax	1.618203

Further, performance is visualized through a sequence of magnified test statistic images (here, the magnification refers to zooming in on the building of interest vice processing on the test statistic itself) of a few of the buildings from the CC CD with $\sigma_p = 0$ to $\sigma_p = 10$. For reference, Fig. 49 shows the buildings in the scene designated with a numeric label. The results for building label 3 are shown in Fig. 50, where it is evident that the increase in σ_p decreases the test statistic surrounding the building which is caused by parallax. These magnified test statistic images are for the

computed parallax direction derived via correspondence matching ($\phi = 86.6°$). The corresponding histograms are shown in Fig. 51, which shows the distribution changes for the parallax pixels as σ_p approaches the manually estimated parallax direction. The histograms show increasing pixel occurrences for the lower brightness values (*i.e.*, pixel has been re-classified to a lower brightness value) as σ_p steps to the next increment. In other words, the histograms represent the false alarm mitigation activity, a larger test statistic pixel value is mitigated to a smaller test statistic pixel value as σ_p increases toward the manually estimated parallax direction. This is repeated for building labeled 6 to emphasize the reduction in parallax-induced false alarms (Fig. 52 and Fig. 53).
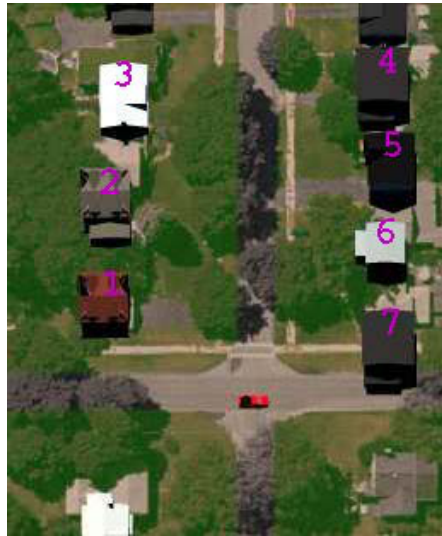
Figure 49. RGB of DIRSIG image, where buildings are labeled $1 - 7$.
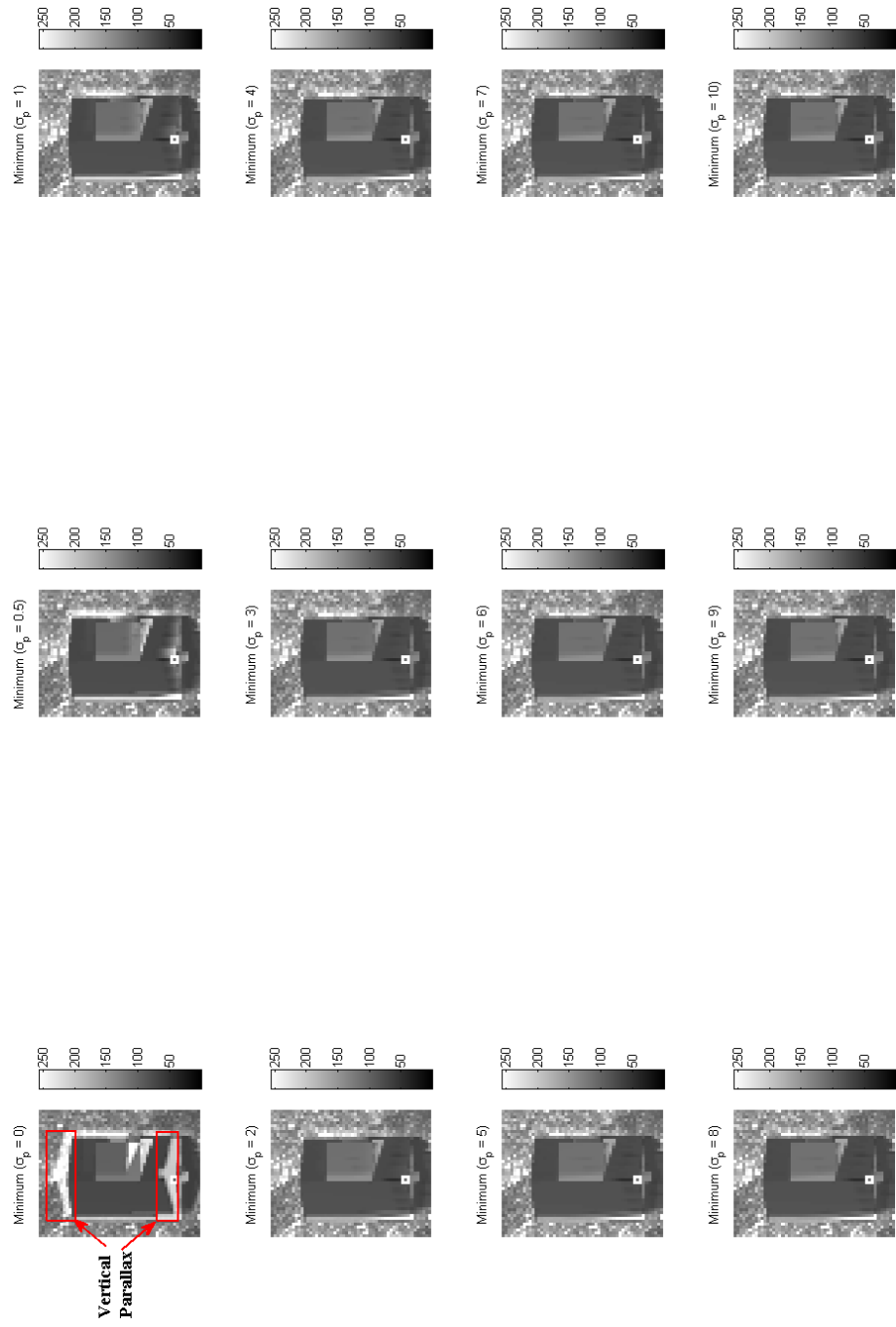
Figure 50. Magnified test statistic results of building 3 to visualize reduction in false alarms due to parallax.
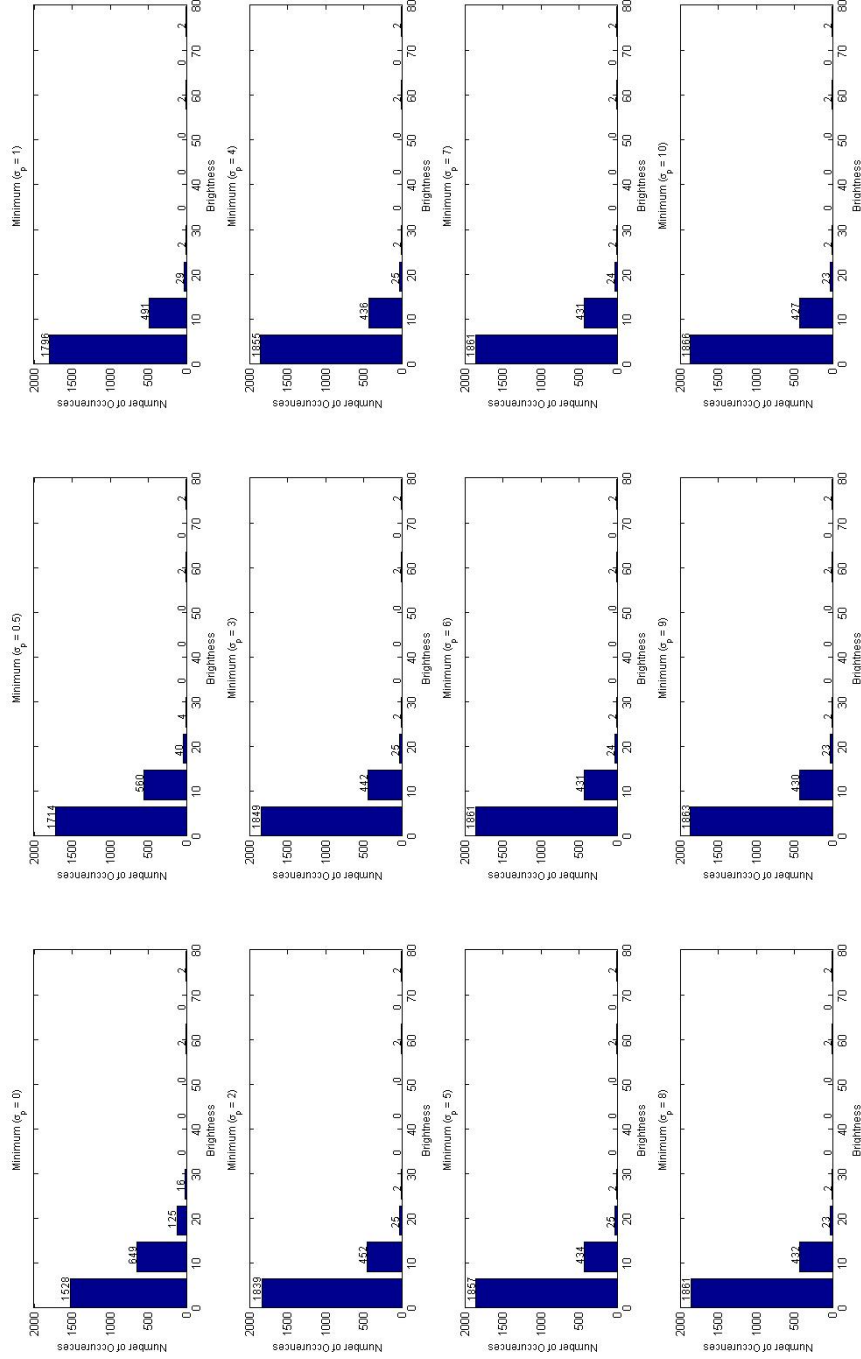
Figure 51. Test statistic histograms for building 3 for increasing σ_p. The histograms show a redistribution of parallax pixels in Fig. 50 as σ_p increases.
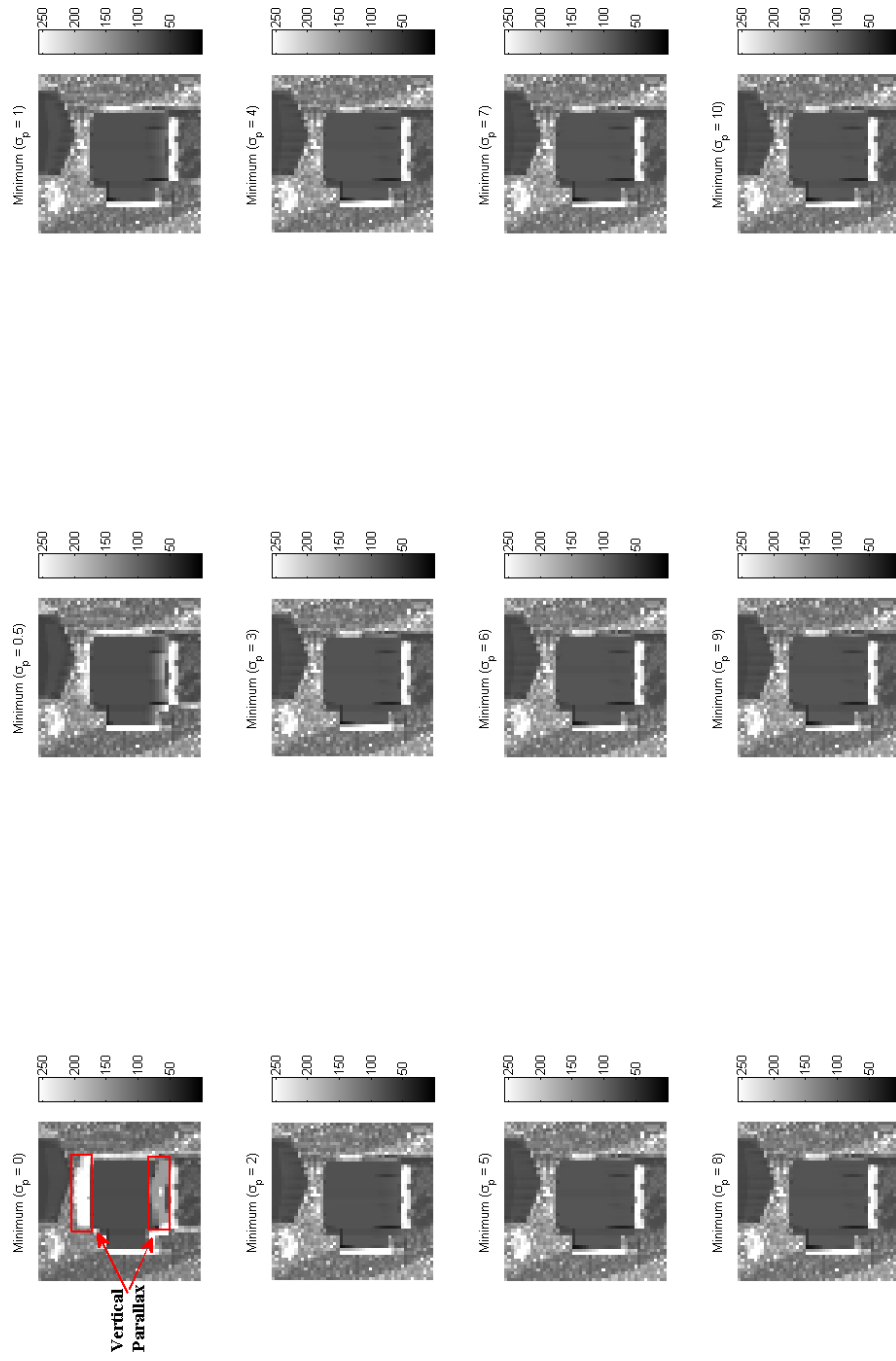
Figure 52. Magnified test statistic results of building 6 to visualize reduction in false alarms due to parallax.
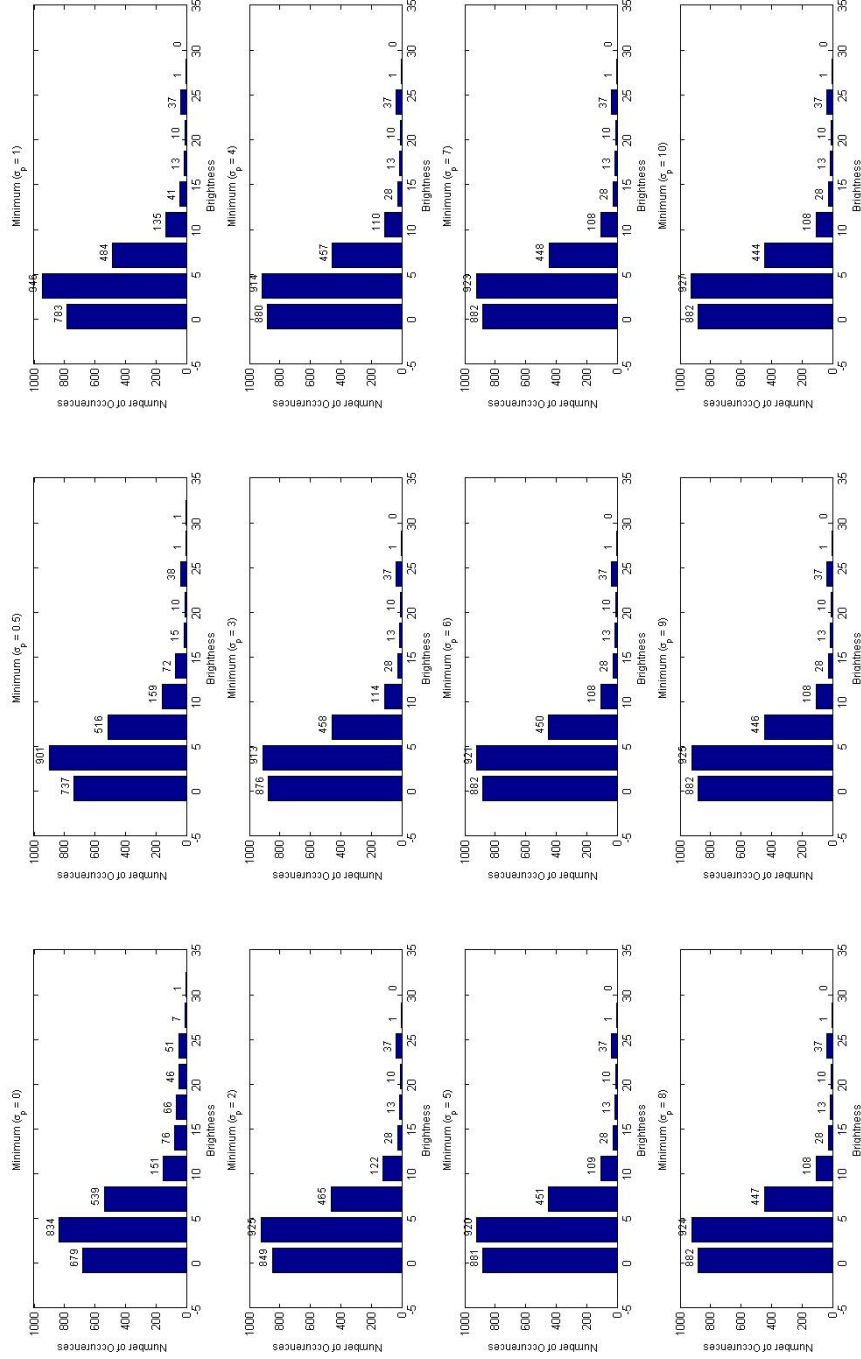
Figure 53. Test statistic histograms for building 6 for increasing σ_p. The histograms show a redistribution of parallax pixels in Fig. 52 as σ_p increases.

Although ROC curve analysis is preferred, performance would be hampered by other spurious false alarm sources. Additional false alarms sources not caused by parallax can affect the reliability of the change detector system and are in influenced by factors such as shadows, illumination differences, and atmospheric effects.

In addition to the visual magnified test statistic images, the SCR is used. The SCR is computed individually for each building defined as

$$\text{SCR} = \frac{\mu_{\text{Change target}} - \mu_{\text{Building}}}{\sigma_{\text{Building}}} \tag{50}$$

where $\mu_{\text{Change target}}$ and μ_{Building} are the mean of the change target and the mean of the building of interest, respectively, and σ_{Building} is the standard deviation of the building of interest. The plot shown in Fig. 54 is the SCR versus σ_p and demonstrates how the clutter from the edge artifacts is reduced with an increase of σ_p resulting in a higher signal. The SCR plot suggests for a large σ_p there is no penalty paid for this parallax compensation improvement. This is likely because the change target is spectrally different than the local surroundings. Otherwise, the SCR would start to decrease at some point or perhaps not increase as σ_p increases because the algorithm would find a local match for the true change target. Contrary to the SCR plot, the statistics (Table 10) and the visual interpretation images indicate that a σ_p value greater than the true parallax would result in missed true change pixels.

4.6   Summary

Incorporating a spatial mis-registration model into a GLRT-based CD methodology leads to a fourth order polynomial test statistic that must be numerically minimized to detect changes in hyperspectral imagery. Results using controlled imagery with synthetically introduced mis-registration show that the approach is able to sup-
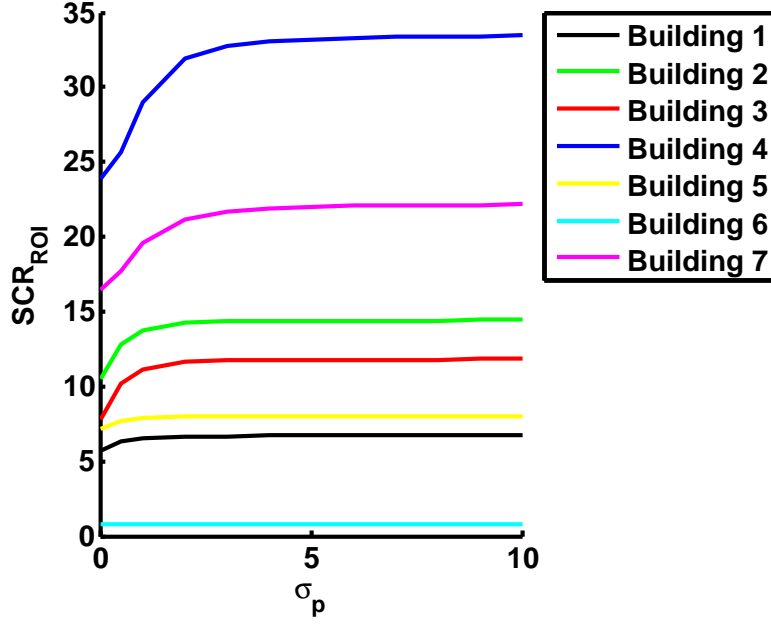
Figure 54. SCR plot for Buildings 1-7 as referenced in Fig. 49 of the synthetic DIRSIG data. This plot shows there is no penalty for the parallax compensation improvement as σ_p increases because the SCR does not decrease.

press mis-registration-introduced false alarms due to high spatial frequency content as seen at edges caused by larger contrast differences (*e.g.*, edges of the panel and fine spatial structure with tree leaves). While the nonlinear optimization is numerically complex, a closed-form quadratic approximation provides nearly identical CD performance while running 30 times faster. While the mis-registration compensation approach provides a benefit for both CC and CE change predictors, a much more substantial improvement in the presence of residual mis-registration is achieved using the CC method.

The CD performance is found to vary somewhat based on user-defined parameters for the underlying prior probability distribution for the residual mis-registration. The best performance appears to be data-dependent. While this supports the importance of including a prior distribution in the model, a unique contribution of our approach over prior methods, it also motivates further work to better understand this parameter

113

sensitivity.

The largest contribution of our generalized CD approach is that it can be extended to incorporate more complicated prior probability distributions for residual mis-registration and serves as a starting point to account for other known image acquisition and preprocessing artifacts. In particular, current hyperspectral CD algorithms (CC and CE) are leveraged in conjunction with bilinear interpolation and stereo correspondence to develop an algorithm for performing hyperspectral CD to address sub-pixel mis-registration and parallax effects. The experiments clearly show that parallax mitigation using correspondence matching gives superior performance when compared to the manual parallax estimate approach. The visual detections exemplify the ability of the hyperspectral algorithm to reduce parallax by eliminating the strong test statistic at building or structure edges. In addition to the visual performance of the algorithm, the test statistic histograms and SCR computations provide evidence of the reduction in parallax-induced edge artifacts in HSCD performance.

V. Conclusion

In this final chapter, a summary of the research is provided. Additionally research contributions are highlighted and the possibility of future work discussed.

5.1 Summary

A summary of change detection (CD) processes was discussed and a framework was outlined to understand the design space of CD applications in Chapter 2. A detailed mathematical formulation of the algorithms developed was presented in Chapter 3. The proposed mis-registration algorithm compensates for mis-registration in the CD process based on minimizing the detection test statistic derived using the generalized likelihood ratio test (GLRT). It was demonstrated that the GLRT formulation results in a closed form solution for the test statistic minimized relative to the unknown local shift parameters. The mathematical formulation led to a fourth-order polynomial solution that was minimized numerically. By performing a second order Taylor series expansion of the test statistic, a quadratic approximation was developed leading to a less computationally-complex closed-form analytical solution. Moreover, the GLRT formulation provided a gateway to address more complex false-alarm sources typically found in persistent surveillance scenarios. To that end, the mis-registration GLRT test statistic was extended to address parallax compensation by rotating the axis along the parallax direction to account for the relative orientation between two consecutive image views.

In Chapter 4, experimental results showed that the methods developed in this research achieve good performance when applied to real or synthetic hyperspectral data sets. This was demonstrated by comparing performances with those reached by two standard anomalous CD methods, chronochrome (CC) and covariance equaliza-

tion (CE). In the case of the mis-registration GLRT, performance was additionally compared with the local co-registration adjustment (LCRA) algorithm. The results indicated far superior performance relative to CC and CE, and comparable performance relative to LCRA. An important benefit to the approach developed in this dissertation, however, is the ability to extend it to other more complex signal processing functions, an attribute not exhibited by LCRA.

Change detector performance was assessed through a visual analysis and quantitatively using the receiver operating characteristic curves (ROC) and the area under the ROC curve (AUC) subject to the availability of detailed truth information. Experiments showed that significant performance improvement is accomplished in the presence of mis-registration for CC ($\text{AUC}_{\text{GLRT}_{\text{CC}}} = 0.9981$ and $\text{AUC}_{\text{CC}} = 0.9972$) and CE ($\text{AUC}_{\text{GLRT}_{\text{CE}}} = 0.9954$ and $\text{AUC}_{\text{CE}} = 0.9909$). The GLRT showed similar performance over LCRA for sub-pixel shifts. Experiments clearly showed that parallax artifacts in the detection statistic are reduced compared to CC. LCRA is not designed to address this type of structured mis-registration and was therefore not evaluated against it.

5.2   Research contributions

The contributions of this work included practical and theoretical aspects. From the practical point of view, the CD framework helps the CD researcher identify research areas of interest and helps the analyst build functional CD systems. From the theoretical point of view, the mis-registration GLRT test statistic provided a gateway to more complex signal processing tasks related to CD and the quadratic approximation to the GLRT test statistic provided a practical implementation of that approach. Extending the mis-registration GLRT test statistic to include parallax compensation for hyperspectral change detection provided a novel contribution in that such an

116

algorithm has yet to be published in the literature.

5.3   Future work

Although the research presented in this dissertation document is highly successful and presents novel approaches to reducing complex false-alarm sources in CD, there are possible areas for future work. These are outlined briefly in this section.

As shown in Chapter 4, excellent false-alarm mitigation results are achieved using (SIFT) features for the correspondence matching in the parallax compensation algorithm. However, other correspondence algorithms exist and may improve performance by providing more reliable feature matching between the test and reference images. Possible correspondence approaches include contrast invariant matching [92] and iterative approaches [93]. In doing so, however, the correspondence matching approach may be more complex. Emerging new research areas such as computational photography give rise to novel applications for correspondence problems that may be applicable to the current body of research [94].

A critical component in the calculation of the parallax direction is the accuracy in mapping corresponding pixels between image pairs. Higher accuracy of the correspondences results in a more accurate estimate of the parallax direction. Another consideration in an urban surveillance scenario is that building occlusions hinder the matching of potentially good image features. Investigation of mismatches or approaches accounting for occlusion pixels may uncover a more accurate correspondence matching method. It is recognized in the literature that multiple sources of correspondence matching errors exist [94]. These error sources include left-right consistency and the flatness of the cost curve [95]. These errors are mitigated by using the matching cost with heuristics rules [95]. Occlusion is a relevant problem to mismatching errors and there exist three classes of algorithms for handling occlusion: methods that de-

tect occlusion, methods that reduce sensitivity to occlusion, and methods that model the occlusion geometry [96]. Correspondence robustness and optimization matching should be considered in future work. The matching algorithm may favor a target data set, for example, hyperspectral data, multi-spectral data, or intensity (gray-scale) data. Furthermore, the user must decide whether or not any accuracy gains in more complex correspondence matching approaches are worth the potential increase in computational time.

The parallax-compensation algorithm requires a $(\tilde{m}, \tilde{n})$ search space defined by the user. Future research can focus on automatizing the $(\tilde{m}, \tilde{n})$ search space through the estimated parallax direction. For example, targeting a larger search along the ϕ direction and limiting the orthogonal direction to a smaller search for efficiency.

The CD performance is found to vary somewhat based on user-defined parameters for the underlying prior probability distribution for the residual mis-registration. In fact, the best performing parameter range, as determined through experimentation, was found to be consistently lower than the known mis-registration. While this supports the importance of including a prior distribution in the model (a unique contribution to this work) it also motivates further work to better understand the relationship of the model parameters to the known mis-registration. Finally, the addition of more extensive, real, truthed, hyperspectral data to exercise and test would refine the approach. This requires such data to be available, which is currently a major shortcoming.

Bibliography

[1] National Aeronautics Airborne Visible/Infrared Imaging Spectrometer (AVIRIS), Jet Propulsion Laboratory (JPL) and Space Administration (NASA), "Imaging spectroscopy: Concept, approach, calibration, atmospheric compensation, research and applications," `http://aviris.jpl.nasa.gov/html/aviris.spectroscopy.html`.

[2] K. Vongsy, M.J. Mendenhall, P.M. Hanna, and J. Kaufman, "Change detection using synthetic hyperspectral imagery," in *Hyperspectral Image and Signal Processing: Evolution in Remote Sensing, 2009. WHISPERS '09. First Workshop on*, 2009, pp. 1–4.

[3] Air Force Cambridge Research Laboratories (U.S.) and S.L. Valley, *Handbook of geophysics and space environments*, McGraw-Hill, 1965.

[4] D.L. Hall and J. Llinas, "An introduction to multisensor data fusion," *Proceedings of the IEEE*, vol. 85, no. 1, pp. 6–23, 1997.

[5] AFRL COMPASE Center, "SFCP documentation: HSI/FOPEN sensor fusion challenge problem," Tech. Rep., Wright-Patterson Air Force Base, Dayton, OH, 2007.

[6] R.J. Radke, S. Andra, O. Al-Kofahi, and B. Roysam, "Image change detection algorithms: A systematic survey," *IEEE Transactions on Image Processing*, vol. 14, no. 3, pp. 294–307, March 2005.

[7] T.M. Lillesand, R.W. Kiefer, and J.W. Chipman, *Remote sensing and image interpretation*, John Wiley & Sons, New York, 2008.

[8] M.T. Eismann and J. Meola, "Hyperspectral change detection: Methodology and challenges.," in *IGARSS*. 2008, pp. 605–608, IEEE.

[9] R.D. Macleod and R.G. Congalton, "A quantitaive comparsion of change detection algorithms for monitoring eelgrass from remotely sensed data," *Photogrammetric Engineering and Remote Sensing*, vol. 64, pp. 207–216, 1998.

[10] T.D. Ross, J.J. Bradley, L.J. Hudson, and M.P. O'Connor, "SAR ATR: so what's the problem? An MSTAR perspective," 1999, vol. 3721, pp. 662–672, SPIE.

[11] M. Borengasser, W. Hungate, and R. Watkins, *Hyperspectral Remote Sensing: Principles and Applications*, CRC Press, USA, 2008.

[12] J. R. Jensen, *Introductory digital image processing; remote sensing perspective*, Prentice-Hall, USA, 1996.

[13] D. Lu, P. Mausuel, E. Brondizio, and E. Moran, "Change detection techniques," *International Journal of Remote Sensing*, vol. 25, no. 12, pp. 2365–2407, June 2003.

[14] G. Jianya, S. Haigang, M. Guorui, and Z. Qiming, "A review of Multi-Temporal remote sensing data change detection algorithms," in *ISPRS Congress Beijing 2008*, 2008, vol. 27, pp. 757–762.

[15] M.T. Eismann, J. Meola, and R.C. Hardie, "Hyperspectral change detection in the presence of diurnal and seasonal variations," *IEEE Transactions on Geoscience and Remote Sensing*, vol. 46, no. 1, pp. 237–249, 2008.

[16] M. T. Eismann, J. Meola, A. D. Stocker, S. G. Beaven, and A. P. Schaum, "Airborne hyperspectral detection of small changes," *Applied Optics*, vol. 47, pp. 27–45, 2008.

[17] V. Ortiz-Rivera, M. Vélez-Reyes, and B. Roysam, "Change detection in hyperspectral imagery using temporal principal components," 2006, vol. 6233, SPIE.

[18] J.F. Mas, "Monitoring land-cover changes: A comparison of change detection techniques," *International Journal of Remote Sensing*, vol. 20, no. 1, pp. 139 – 152, 1999.

[19] T.L. Sohl, "Change analysis in the United Arab Emirates: An investigation of techniques," *Photogrammetric Engineering and Remote Sensing*, vol. 65, no. 4, pp. 475 – 484, 1999.

[20] A. Rosenfeld, "Automatic detection of changes in reconnaissance data," *5th National Convention on Military Electronics Conference Proceedings*, pp. 492–499, 1961.

[21] L. Marcenaro, G. Gera, and C. Regazzoni, "Adaptive change detection approach for object detection in outdoor scenes under variable speed illumination changes," 2000, vol. 2, pp. 1025–1028, European Signal Processing Conf.

[22] T. Knudsen and B.P. Olsen, "Automated change detection for updates of digital map databases," *Photogrammetric Engineering and Remote Sensing*, vol. 69, pp. 1289–1296, 2003.

[23] L. Zhang, M. Liao, L. Yang, and H. Lin., "Remote sensing change detection based on canonical correlation analysis and contextual Bayes decision," *Photogrammetric Engineering and Remote Sensing*, vol. 73, no. 3, pp. 311–318, 2007.

[24] P.L. Rosin, "Thresholding for change detection," in *Computer Vision, 1998. Sixth International Conference on*, Jan 1998, pp. 274–279.

[25] P. K. Sahoo, S. Soltani, A.K.C. Wong, and Y.C. Chen, "A survey of thresholding techniques," *Computer Vision, Graphics, Image Processing*, vol. 41, no. 2, pp. 233–260, 1988.

[26] M.Sezgin and B. Sankur, "Survey over image thresholding techniques and quantitative performance evaluation," *Journal of Electronic Imaging*, vol. 13, no. 1, pp. 146–168, 2004.

[27] B. G. Lee, V. T. Tom, and M. J. Carlotto, "A signal-symbol approach to change detection," *Proc. AAAI*, 1986.

[28] Y. Hu, S.M. de Jong, and R. Sluiter, "A modeling-based threshold approach to derive change/no change information over vegetation area," *Geoinformatiocs 2004 Proceedings 12th International Conference on Geoinformatics - Geospatial Information Research: Bridging the Pacific and Atlantic*, 2004.

[29] K. Vongsy and M.J. Mendenhall, "Improved change detection through post change classification: A case study using synthetic hyperspectral imagery," in *Hyperspectral Image and Signal Processing: Evolution in Remote Sensing (WHISPERS), 2010 2nd Workshop on*, June 2010, pp. 1 –4.

[30] J.B. Collins and C.E. Woodcock, "An assessment of several linear change detection techniques for mapping forest mortality using multitemporal LANDSAT TM data," *Remote Sensing of Environment*, vol. 56, no. 1, pp. 66 – 77, 1996.

[31] C. Lee and J. Bethel, "Georegistration of airborne hyperspectral image data," *IEEE Transactions on Geoscience and Remote Sensing*, vol. 39, no. 7, pp. 1347–1351, 2001.

[32] S. Leprince, S. Barbot, F. Ayoub, and J. Avouac, "Automatic and precise orthorectification, coregistration, and subpixel correlation of satellite images, application to ground deformation measurements," *IEEE Transactions on Geoscience and Remote Sensing*, vol. 45, no. 6, pp. 1529–1558, 2007.

[33] Exelis Visual Information Solutions, *ENVI Tutorial: Introduction to Hyperspectral Data*, http://www.exelisvis.com/portals/0/tutorials/envi/Hyperspectral_Intro.pdf.

[34] A. Martinez-Uso, F. Pla, J.M. Sotoca, and P. Garcia-Sevilla, "Clustering-based hyperspectral band selection using information measures," *IEEE Transactions on Geoscience and Remote Sensing*, vol. 45, no. 12, pp. 4158–4171, 2007.

[35] N.P. Jacobson and M.R. Gupta, "Design goals and solutions for display of hyperspectral images," *IEEE Transactions on Geoscience and Remote Sensing*, vol. 43, no. 11, pp. 2684–2692, 2005.

121

[36] Q. Du, N. Raksuntorn, S. Cai, and R.J. Moorhead II, "Color display for hyper-spectral imagery," *IEEE Transactions Geoscience and Remote Sensing*, vol. 46, no. 6, pp. 1858–1866, 2008.

[37] M. J. Mendenhall and E. Merényi, "Relevance-based feature extraction from hyperspectral images," *IEEE Transactions on Neural Networks*, vol. 19, Apr 2008.

[38] M.T. Eismann and R.C. Hardie, "Hyperspectral resolution enhancement using high-resolution multispectral imagery with arbitrary response functions," *IEEE Transactions on Geoscience and Remote Sensing*, vol. 43, no. 3, pp. 455–465, 2001.

[39] M.T. Eismann, *Hyperspectral Remote Sensing*, SPIE Press Book, April 2012.

[40] P. R. Coppin, I. Jonckheere, and K. Nachaerts, "Digital change detection in ecosystem monitoring: A review," *International Journal of Remote Sensing*, vol. 25, no. 9, pp. 1565–1596, 2004.

[41] A. Singh, "Digital change detection techniques using remotely-sensed data," *International Journal of Remote Sensing*, vol. 10, no. 6, pp. 989–1003, 1989.

[42] P. J. Deer, "Digital change detection techniques: civilian and military appli-cations," Tech. Rep., International Symposium on Spectral Sensing Research, Greenbelt, MD, 1995.

[43] P. J. Deer, *Digital change detection in remotely sensed imagery using fuzzy set theory*, Ph.D. thesis, University of Adelaide, 1998.

[44] J.A. Benediktsson, P.H. Swain, and O.K. Ersoy, "Neural network approaches versus statistical methods in classification of multisource remote sensing data," in *Geoscience and Remote Sensing Symposium, 1989. IGARSS'89. 12th Canadian Symposium on Remote Sensing., 1989 International*, July 1989, vol. 2, pp. 489 –492.

[45] H. Bischof, W. Schneider, and A.J. Pinz, "Multispectral classification of LANDSAT-images using neural networks," *IEEE Transactions on Geoscience and Remote Sensing*, vol. 30, no. 3, pp. 482 –490, May 1992.

[46] K. Johansen, L.A. Arroyo, S. Phinn, and C. Witte, "Object-oriented change detection of riparian environments from high spatial resolution multi-spectral images," *International Society for Photogrammetry and Remote Sensing, Alberta*, 2008.

[47] D. Manolakis and G. Shaw, "Detection algorithms for hyperspectral imaging applications," *IEEE Signal Processing Magazine*, vol. 19, no. 1, pp. 29–43, Jan. 2002.

[48] O.A. de Carvalho Júnior, R.F. Guimarães, and R.A.T. Gomes, "Spectral change detection," in *IGARSS*, 2007, pp. 1935–1938.

[49] A. Schaum and A. Stocker, "Advanced algorithms for autonomous hyperspectral change detection," *Applied Imagery Pattern Recognition Workshop, 2004. Proceedings. 33rd*, pp. 33 – 38, Oct 2004.

[50] A. Schaum and A. Stocker, "Long-interval chronochrome target detection," in *Proc. 1997 International Symposium on Spectral Sensing Research*, 1998, pp. 1760–1770.

[51] A. Schaum and A. Stocker, "Linear chromodynamics models for hyperspectral target detection," in *Aerospace Conference, 2003. Proceedings. 2003 IEEE*, 2003, vol. 4, pp. 41879–41885.

[52] A. Schaum and A. Stocker, "Hyperspectral change detection and supervised matched filtering based on covariance equalization," *Proceedings SPIE*, vol. 5425, pp. 77–90, 2004.

[53] J. Theiler and B. Wohlberg, "Local coregistration adjustment for anomalous change detection," *Geoscience and Remote Sensing, IEEE Transactions on*, vol. 50, no. 8, pp. 3107–3116, 2012.

[54] P. Smits and A. Annoni, "Toward specification-driven change detection," *IEEE Transactions Geoscience and Remote Sensing*, vol. 38, no. 3, pp. 1484–1488, 2000.

[55] S. Elhabian, K. El-Sayed, and S. Ahmed, "Moving Object Detection in Spatial Domain using Background Removal Techniques - State-of-Art," *Recent Patents on Computer Science*, vol. 1, no. 1, pp. 32–54, 2008.

[56] H. Rue and L. Held, *Gaussian Markov random fields: Theory and applications*, Springer, New York, 2005.

[57] J. Wang, W. Qin, and D. Li, "Object-Oriented Per-Parcel Land Use Change Detection Integrating GIS and Remote Sensing," in *ISPRS mid-term symposium Remote sensing: from pixels to processes, May 8th - 11th 2006, Enschede, The Netherlands*, 2006.

[58] Z. Xiaodong, G. JianYa, and L. Deren, "A Strategy of Change Detection Based on Remotely Sensed Imagery and GIS Data," in *ISPRS mid-term symposium Remote sensing: from pixels to processes, May 8th - 11th 2006, Enschede, The Netherlands*, 2006.

[59] Y. Gu, Y. Zhang, and J. Zhang, "Integration of spatial-spectral information for resolution enhancement in hyperspectral images," *IEEE Transactions on Geoscience and Remote Sensing*, vol. 46, no. 5, pp. 1347–1358, 2008.

[60] P.L. Rosin and E. Ioannidis, "Evaluation of global image thresholding for change detection," *Pattern Recognition Letters*, vol. 24, no. 14, pp. 2345–2356, October 2003.

[61] T. Fawcett, "An introduction to ROC analysis," *Pattern Recognition Letters*, vol. 27, no. 8, pp. 861–874, June 2006.

[62] A. P. Bradley, "The use of the area under the roc curve in the evaluation of machine learning algorithms," *Pattern Recognition*, vol. 30, pp. 1145–1159, 1997.

[63] P. A. J. Van Oort, "Interpreting the change detection error matrix," *Remote Sensing of Environment*, vol. 108, pp. 1–8, 2007.

[64] J. Demšar, "Statistical comparisons of classifiers over multiple data sets," *Journal of Machine Learning Research*, vol. 7, pp. 1–30, Dec. 2006.

[65] S. Daskalaki, I. Kopanas, and N. Avouris, "Evaluation of classifiers for an uneven class distribution problem," *Applied Artificial Intelligence*, vol. 20, pp. 1–37, 2006.

[66] N. M. Adams and D. J. Hand, "Improving the practice of classifier performance assessment," *Neural Comput.*, vol. 12, no. 2, pp. 305–311, Feb. 2000.

[67] J.B. Campbell, *Introduction to Remote Sensing*, Taylor & Francis, London, 2002.

[68] E. Trucco and A. Verri, *Introductory Techniques for 3-D Computer Vision*, Prentice Hall PTR, Upper Saddle River, NJ, USA, 1998.

[69] F. Hu and Y. Zhao, "Comparative research of matching algorithms for stereo vision," *Computational Information Systems (JCIS)*, vol. 9, no. 13, pp. 5457–5465, 2013.

[70] T.Ch. Malleswara Rao, K. Venugopala Rao, A. Ravi Kumar, D.P. Rao, and B.L. Deekshatulu, "Digital Terrain Model (DTM) from Indian Remote Sensing (IRS) satellite data from the overlap area of two adjacent paths using digital photogrammetric techniques," *Photogrammetric Engineering and Remote Sensing*, vol. 62, no. 1, pp. 727–731, 1996.

[71] R. Hartley and A. Zisserman, *Multiple View Geometry in Computer Vision*, Cambridge University Press, New York, NY, USA, 2nd edition, 2003.

[72] K. Mikolajczyk and C. Schmid, "Scale and affine invariant interest point detectors," *International Journal of Computer Vision*, vol. 60, no. 1, pp. 63–86, 2004.

[73] D.G. Lowe, "Distinctive image features from scale-invariant keypoints," *Internation Journal of Computer Vision*, vol. 60, pp. 91–110, November 2004.

[74] J. F. Hughes, A. Van Dam, M. McGuire, D. F. Sklar, J. D. Foley, S. K. Feiner, and K. Akeley, *Computer graphics: principles and practice (3rd ed.)*, Addison-Wesley Professional, Boston, MA, USA, July 2013.

[75] L.L. Scharf and C. Demeure, *Statistical signal processing: detection, estimation, and time series analysis*, Addison-Wesley Series in Electrical and Computer Engineering. Addison-Wesley Pub. Co., 1991.

[76] B. Stevenson, R. O'Connor, W. Kendall, A. Stocker, W. Schaff, D. Alexa, J. Salvador, M. Eismann, K. Barnard, and J. Kershenstein, "The civil air patrol archer hyperspectral sensor system," 2005.

[77] DIRSIG, "The digital imaging and remote sensing image generation model," `http://dirsig.cis.rit.edu/`.

[78] J. Meola, "A model-based approach to hyperspectral change detection," Doctoral Dissertation, Ohio State University, 2011.

[79] J. Meola and M.T. Eismann, "Image misregistration effects on hyperspectral change detection," 2008.

[80] M.J. Mendenhall and E. Merenyi, "On the evaluation of synthetic hyperspectral imagery," in *Hyperspectral Image and Signal Processing: Evolution in Remote Sensing, 2009. WHISPERS '09. First Workshop on*, 2009, pp. 1–4.

[81] A. W. Yarbrough, M.J. Mendenhall, and R.K. Martin, "The effects of atmospheric mis-estimation on hyperspectral-based adaptive matched filter target detection as measured by the bhattacharyya coefficient," in *Hyperspectral Image and Signal Processing: Evolution in Remote Sensing (WHISPERS), 2010 2nd Workshop on*, 2010, pp. 1–4.

[82] K. Vongsy and M.J. Mendenhall, "A comparative study of spectral detectors," in *Hyperspectral Image and Signal Processing: Evolution in Remote Sensing (WHISPERS), 2011 3rd Workshop on*, june 2011, pp. 1–4.

[83] A.W. Yarbrough, M.J. Mendenhall, R.K. Martin, and S.T. Fiorino, "Hyperspectral-based adaptive matched filter detector error as a function of atmospheric water vapor estimation," *Geoscience and Remote Sensing, IEEE Transactions on*, vol. 52, no. 4, pp. 2029–2039, 2014.

[84] D.E. Rumelhart, G.E. Hintont, and R.J. Williams, "Learning representations by back-propagating errors," *Nature*, vol. 323, no. 6088, pp. 533–536, 1986.

[85] T. Hastie, R. Tibshirani, and J. Friedman, *The elements of statistical learning: data mining, inference and prediction*, Springer, 2 edition, 2009.

[86] M. Diehl, *Script for Numerical Optimization Course*, 2013, Available at: http://homes.esat.kuleuven.be/ mdiehl/NUMOPT/numopt.pdf.

[87] S. Haykin, *Neural Networks – A Comprehensive Foundation*, Prentice Hall, Upper Saddle River, New Jersey 07458, second edition, 1999.

[88] N. Metropolis, A. W. Rosenbluth, M. N. Rosenbluth, A. H. Teller, and E. Teller, "Equation of state calculations by fast computing machines," *The Journal of Chemical Physics*, vol. 21, no. 6, pp. 1087–1092, 1953.

[89] J. D'Errico, *Understanding fminsearchbnd*, 2005, Available at: http://www.mathworks.com/matlabcentral/fileexchange/8277-fminsearchbnd-fminsearchcon.

[90] J. C. Lagarias, J. A. Reeds, M. H. Wright, and P. E. Wright, "Convergence Properties of the Nelder-Mead Simplex Method in Low Dimensions," *SIAM Journal of Optimization*, vol. 9, no. 1, pp. 112.

[91] J. A. Nelder and R. Mead, "A simplex method for function minimization," *Computer Journal*, vol. 7, pp. 308–313, 1965.

[92] A. S. Ogale and Y. Aloimonos, "Robust contrast invariant stereo correspondence," in *Robotics and Automation, 2005. ICRA 2005. Proceedings of the 2005 IEEE International Conference on*, 2005, pp. 819–824.

[93] J. Y. Chang, K. M. Lee, and S. U. Lee, "Stereo matching using iterative reliable disparity map expansion in the color-spatial-disparity space.," *Pattern Recognition*, vol. 40, no. 12, pp. 3705–3713, 2007.

[94] H. L. Zimmer, *Correspondence Problems in Computer Vision Novel Models, Numerics, and Applications*, Doctoral dissertation, Universität des Saarlandes, 2012.

[95] X. Hu and P. Mordohai, "Evaluation of stereo confidence indoors and outdoors," in *Computer Vision and Pattern Recognition (CVPR), 2010 IEEE Conference on*, 2010, pp. 1466–1473.

[96] M.Z. Brown, D. Burschka, and G.D. Hager, "Advances in computational stereo," *Pattern Analysis and Machine Intelligence, IEEE Transactions on*, vol. 25, no. 8, pp. 993–1008, 2003.

REPORT DOCUMENTATION PAGE

Form Approved
OMB No. 0704–0188

The public reporting burden for this collection of information is estimated to average 1 hour per response, including the time for reviewing instructions, searching existing data sources, gathering and maintaining the data needed, and completing and reviewing the collection of information. Send comments regarding this burden estimate or any other aspect of this collection of information, including suggestions for reducing this burden to Department of Defense, Washington Headquarters Services, Directorate for Information Operations and Reports (0704–0188), 1215 Jefferson Davis Highway, Suite 1204, Arlington, VA 22202–4302. Respondents should be aware that notwithstanding any other provision of law, no person shall be subject to any penalty for failing to comply with a collection of information if it does not display a currently valid OMB control number. **PLEASE DO NOT RETURN YOUR FORM TO THE ABOVE ADDRESS.**

1. REPORT DATE *(DD–MM–YYYY)*	2. REPORT TYPE	3. DATES COVERED *(From — To)*
27–03–2014	PhD Dissertation	Oct 2008 — Feb 2014

4. TITLE AND SUBTITLE

5a. CONTRACT NUMBER

5b. GRANT NUMBER

5c. PROGRAM ELEMENT NUMBER

6. AUTHOR(S)

5d. PROJECT NUMBER

5e. TASK NUMBER

5f. WORK UNIT NUMBER

7. PERFORMING ORGANIZATION NAME(S) AND ADDRESS(ES)

Air Force Institute of Technology
Graduate School of Engineering and Management (AFIT/EN)
2950 Hobson Way
WPAFB OH 45433-7765

8. PERFORMING ORGANIZATION REPORT NUMBER

AFIT-ENG-DS-14-M-01

9. SPONSORING / MONITORING AGENCY NAME(S) AND ADDRESS(ES)

AFRL/RYAT
Clare Mikula, Branch Chief
2241 Avionic Circle Area B, B620
WPAFB, OH 45433
(937) 528-8839; clare.mikula@us.af.mil

10. SPONSOR/MONITOR'S ACRONYM(S)

AFRL/RYAT

11. SPONSOR/MONITOR'S REPORT NUMBER(S)

12. DISTRIBUTION / AVAILABILITY STATEMENT

DISTRIBUTION STATEMENT A: APPROVED FOR PUBLIC RELEASE; DISTRIBUTION UNLIMITED

13. SUPPLEMENTARY NOTES

14. ABSTRACT

Accurate change detection (CD) results in urban environments is of interest to a diverse set of applications including military surveillance, environmental monitoring, and urban development. This work presents a hyperspectral CD (HSCD) framework. The framework uncovers the need for HSCD methods that resolve false change caused by image parallax. A Generalized Likelihood Ratio Test (GLRT) statistic for HSCD is developed that accommodates unknown mis-registration between imagery described by a prior probability density function for the spatial mis-registration. The potential of the derived method to incorporate more complex signal proccessing functions is demonstrated by the incorporation of a parallax error mitigation component. Results demonstrate that parallax mitigation reduces false alarms.

15. SUBJECT TERMS

Hyperspectral, Change Detection, Generalized Likelihood Ratio Test, Mis-registration, Parallax

16. SECURITY CLASSIFICATION OF:			17. LIMITATION OF ABSTRACT	18. NUMBER OF PAGES	19a. NAME OF RESPONSIBLE PERSON
a. REPORT	**b. ABSTRACT**	**c. THIS PAGE**			Dr. Gilbert L. Peterson, AFIT/ENG
U	U	U	U	146	**19b. TELEPHONE NUMBER** *(include area code)* (937) 785-6565 x4281; gilbert.peterson@afit.edu

Standard Form 298 (Rev. 8–98)
Prescribed by ANSI Std. Z39.18